Quantification of Methane Emissions by Surface Mass Balance Method

YEUHYUN KIM

A THESIS SUBMITTED TO THE FAUCULTY OF

GRADUATE STUDIES IN PARTIAL FULFILMENT OF

THE REQUIREMENTS FOR THE DEGREE OF

MASTERS OF SCIENCE

GRADUATE PROGRAM IN CHEMISTRY

YORK UNIVERSITY

TORONTO, ONTARIO

MARCH 2023

ABSTRACT

The waste management and oil and natural gas sectors account for more than half of Canada's anthropogenic methane emissions. Yet, current bottom-up inventories fail to accurately quantify emissions from the two sectors since extrapolation of an individual facility measurement create inherent uncertainties without considering spatiotemporal variability. This thesis presents a surface mass balance method as a cost-effective top-down technique to conveniently validate the bottom-up inventories. Mobile methane measurements were performed for two large landfills, Keele Valley Landfill and Greenlane Landfill and the city of Sarnia which included petrochemical industries and residential areas by employing a Cavity Ringdown Spectrometer (CRDS) mounted in a vehicle to capture downwind enhancements of methane. The mobile measurement was able to provide high spatial resolutions, adequate to comprehensively characterize and quantify methane plumes. Methane emission from the Greenlane landfill was estimated to be 3300 ± 730 kg h^{-1} by a mass balance approach equivalent to 28.9 ± 6.3 kt annual methane. An estimation by a gaussian dispersion model provided a similar emission rate of 3320 ± 250 kg h^{-1}. Compared to the GreenHouse Gas Reporting Program (GHGRP) reported value of 2.1 kt in 2020, this top-down measurement showed the landfill methane emission was 14 times greater than the bottom-up inventory. The regression analysis of the mixing ratios of CO_2 and CH_4 in the landfill plumes showed positive correlation with an average molar ratio of 0.99 ± 0.04 mole $mole^{-1}$ which was used to estimate CO_2 emission to be 7600 ± 1700 kg h^{-1}. The city of Sarnia including its industrial complex and residential areas showed a total methane emission rate of 2450 ± 560 kg h^{-1}. It is estimated the city emits 21.5 ± 4.9 kt CH_4 annually accounting for 45% of Ontario's oil and gas methane emission. The gaussian model demonstrated that refineries were major methane emitters with estimated source rates of 672 ± 230 kg h^{-1} (Imperial Oil), 349 kg h^{-1} for (Suncor) and 198 kg h^{-1} (Shell Canada) respectively. These estimated source rates from facilities were consistently 9-10 times greater than the GHGRP estimates. The discrepancies confirmed in the study emphasizes that it is significant to reconcile top-down measurements with the bottom-up inventories to provide a more accurate understanding of methane sources and sinks in Canada.

ACKNOWLEDGEMENTS

First of all, I would like to express my sincerest appreciation to my supervisor, Robert McLaren for his valuable and unwavering support and guidance. He introduced me to the field of atmospheric chemistry, and I treasured every moment of the new experience under his supervision. His ingenious scholarly insights and scientific approach helped me grow as a researcher and his profound belief in my ability encouraged and motivated me to pursue research. I am also grateful for my committee members, Trevor VandenBoer, John Liggio, Cora Young and Neil Tandon for their invaluable comments and enthusiastic discussion of my work.

I am thankful for Environment and Climate Change Canada for lending us the Picarro instrument and Mariani Zen for providing valuable boundary layer data and analysis. I would like to also recognize and thank for the assistance and support from the research group member, Austin Pritchard-Oh.

TABLE OF CONTENTS

LIST OF TABLES

LIST OF FIGURES

Chapter 1 : Introduction

1.1.Atmospheric methane

As the simplest hydrocarbon, methane, (CH_4) is one of the most abundant organic compounds on Earth with large natural reservoirs found in the deep sea, underground and in the arctic. It is formed by two primary processes: thermogenically, through breakdown of larger organic molecules by a natural heat source and biogenically, by the decomposition of waste product from methanogenic archaea (Stolper, 2015). Thermal breakdown of the decomposed organic matter that are deposited underground and deep sea over million years form natural gas in which methane accounts for 75% to 99% of its composition (Simon, 1975).

Methane has a tetrahedral geometry with equivalent C-H bonds from the sp^3 hybridization of carbon. Compared to other alkanes, due to its high C-H bond strength, methane is one of the least reactive alkanes in the atmosphere. Yet, it is known to impact the formation and oxidative capacity of other important atmospheric species, such as carbon monoxide (CO), formaldehyde (HCHO), hydroxyl radicals (OH) and ozone (O_3).

The major sink of methane is from its oxidation reaction initiated by the hydroxyl radical (OH) in the troposphere which contributes to about 90% of total methane sink (Saunois et al., 2016). Soil uptake and oxidation by methanotrophs account for 4%, while destruction by tropospheric chlorine radical account for 3%. Stratospheric loss by chlorine and oxygen radical takes up rest of 3%. (Kirschke et al., 2013) Methane oxidation by OH first forms methylperoxy radical (CH_3O_2) (Ehhalt and Schmidt, 1978):

$$CH_4 + OH \rightarrow CH_3 + H_2O \qquad (1.1)$$

$$CH_3 + O_2 \rightarrow CH_3O_2 \qquad (1.2)$$

Methylperoxy radical can react with hydroperoxyl radical (HO_2) or NO to form methyl hydroperoxide(CH_3OOH), formaldehyde (HCHO) and ozone (O_3).

Formaldehyde is formed by methylperoxy radical reacting with HO_2 by reaction 1.3 – 1.4:

$$CH_3OO + HO_2 \rightarrow CH_3OOH + O_2 \qquad (1.3)$$

$$CH_3OOH + OH \rightarrow HCHO + OH + H_2O \quad (1.4)$$

In the presence of NO, especially in polluted regions with high NO_x, methylperoxy radical can react with NO to form methoxy radical (CH_3O) as in reaction 1.5:

$$CH_3O_2 + NO \rightarrow CH_3O + NO_2 \quad (1.5)$$

Methoxy radical further reacts with oxygen to produce HO_2, which can also react with NO to enhance NO_2:

$$CH_3O + O_2 \rightarrow HCHO + HO_2 \quad (1.6)$$

$$HO_2 + NO \rightarrow OH + NO_2 \quad (1.7)$$

Formaldehyde produced in reaction 1.4 and 1.6 can undergo oxidation to produce CO:

$$HCHO + 2O_2 \rightarrow CO + O_3 + H_2O \quad (1.8)$$

Subsequently the photolysis of NO_2 produced from reaction 1.5 and CO from 1.8 can generate ozone, O_3 where M in reaction 1.10 denotes any species in the air to function as a third body to help facilitate the reaction. Reaction 1.11 shows a net reaction equation for series of CO oxidation mechanism initiated by OH radicals which is the dominant sink for OH.:

$$NO_2 + h\nu \rightarrow NO + O(^3P) \quad (1.9)$$

$$O(^3P) + O_2 + M \rightarrow O_3 + M \quad (1.10)$$

$$CO + 2O_2 + h\nu \rightarrow CO_2 + O_3 \quad (1.11)$$

Tropospheric ozone is a hazardous air pollutant known to be a major component of smog as well as the cause of major health risks to mammals such as asthma, throat irritation, and emphysema (Manisalidis et al., 2020). Therefore, not only as a key to the climate change mitigation, but the reduction in methane emissions is also a viable approach to reduce health risks by air pollution. Tropospheric ozone can be reduced by 0.4-0.7 ppb per 10% reduction in anthropogenic methane emissions according to West and Fiore (2005).

The atmospheric lifetime of methane is considered to be 9.25 ± 0.6 years which is calculated from the atmospheric methane burden, *m* divided by its sinks, *L* (Myhre et al., 2013):

$$\tau_{CH4} = \frac{m}{L} \quad (1.12)$$

The chemistry of methane is involved in several complex feedback loops that alters the concentration of major oxidants such as O_3 and OH. The feedback loops increase the lifetime of methane and thus, the methane burden within the atmosphere since the availability of OH radicals decrease by an increase in methane concentration. This amplification effect leads to methane's perturbation lifetime of 12.4 ± 1.4 years. (Jardine 2004)

The availability of OH also affects the seasonal methane concentration. Observation of continental methane columns over North America by TROPOMI Satellite were plotted to show methane column methane mixing ratio of 1791 ± 93 ppb during July 10th to 17th and 1896 ± 34 ppb during December 13th to 19th with a seasonal difference of 105 ppb in the year 2021 as in Figure 1.1.

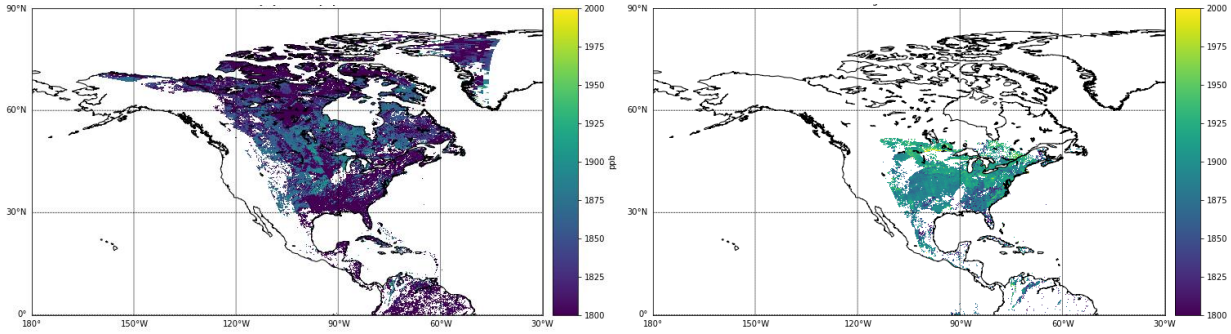

Figure 1.1: TROPOMI observation of XCH_4 over North America (Left) period between July 10 – 17 2021 (Right) between Dec 13 – 19 2021

The variability is caused by variance in UV actinic flux and humidity (Dlugokencky et al., 1997) affecting the formation of hydroxyl radicals dependent on UV < 310 nm:

$$O_3 \rightarrow O(^1D) + O_2 \text{ (with UV < 310 nm)} \quad (1.13)$$

$$O(^1D) + H_2O \rightarrow 2OH \quad (1.14)$$

Global methane concentration shows inverse correlation to the OH concentration. Methane has the lowest concentration during summer when stronger UV light enhances OH formation while methane concentration is the highest during wintertime between November to March. Aside from the photolysis of ozone as a major OH source, other minor sources include photolysis of

nitrous acid (HONO), hydrogen peroxide (H_2O_2) and a reaction of nitrogen monoxide (NO) with hydroperoxyl radical (HO_2) showing that the OH chemistry is closely linked with NO_x cycle.

In recent years, the increased use of natural gas allowed more methane to be released into the atmosphere which escalated the global concentration of atmospheric methane (CH_4). It has been shown to exacerbate the issue of climate change as methane proves to be a significant anthropogenic green-house gas with the strength of radiative forcing (RF) second to carbon dioxide (CO_2). Its global warming potential (GWP) is shown to be 28 – 86 times more effective at trapping heat per unit mass than CO_2 on 100 - and 20 -year time scales, respectively. (Myhre et al., 2013). GWP potential equates 1 kg CH_4 to 28 kg CO_2. On mole basis, 1 kg CH_4 corresponds to 62.34 mole while 28 kg CO_2 is equivalent to 1954.5 mole. Therefore, per mole basis, 100-year warming potential is equivalent to 31.3 times more effect per unit mole of CH_4 than CO_2. Similarly, its 20 years mole-basis global warming potential corresponds to 10.2 CO_2 eq. per mole of CH_4.

Anthropogenic emissions are the major drivers accounting for up to 65% of total global CH_4 emission among which natural gas and petroleum systems (30%), enteric fermentation and agriculture (27%), and landfill (17%) are the predominant anthropogenic sources. (Stocker et al., 2013).

In Canada, 13% of the country's total greenhouse gas (GHG) emissions is from methane in which oil and gas sector accounts for 36 – 40% followed by 30% agriculture and 27% waste management according to 2020 inventory report of methane sources and sinks in Canada (Figure 1.2). Canada's oil and gas sector as well as waste management especially show higher than global average methane emissions that the National Inventory Report highlights the importance of improved quantification methodology over these two sectors.

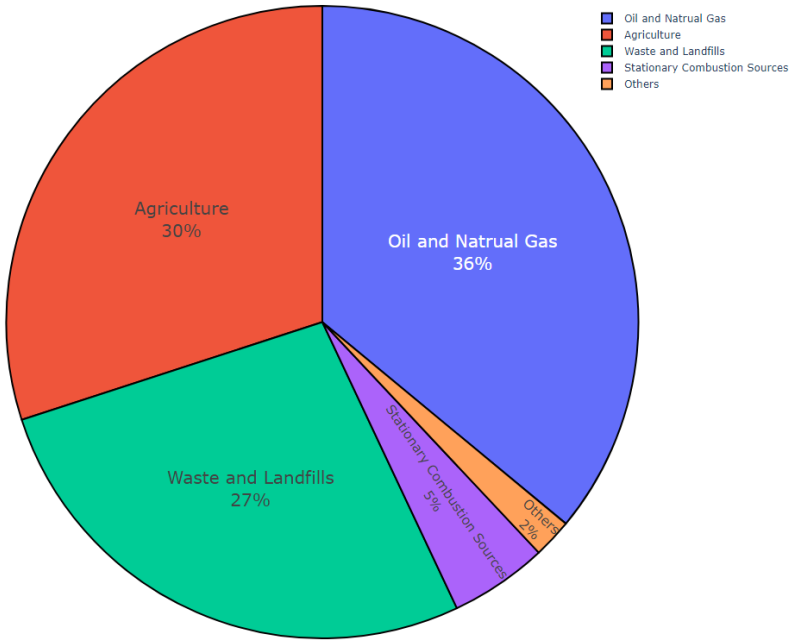

Figure 1.2: 2020 Methane Emission Summary for Canada (Total of 3700 kt)

Since anthropogenic activities have been considered as significant contributors of atmospheric methane, its concentration has shown to consistently increase since the time of industrialization. Especially, global methane mixing ratio has been shown to almost double from approximately 700 ppb in preindustrial times to 1870 ppb in 2020 (Dlugokencky, 2020).

Figure 1.3 shows the global monthly average methane mixing ratio in dry air mole fraction provided by NOAA's Earth System Research Laboratory, which is constructed from the average of globally distributed air sampling sites. The mixing ratio of methane was continuously increasing, since the preindustrial era, to early 2000s when the growth halted between 2000 to 2007. There has been conflicting hypotheses and confusion over this stabilization of methane. The modelling study by Turner et al. (2017) assumes the likely cause of the stabilization to be the increase in OH sink offsetting increasing methane emissions. Yet current surface observing system does not allow clarification over the matter, without robust constraint on OH variability and exact emissions estimates of methane. Moreover, the leveling of methane during this period may be the result of other changes uncorrelated to changes in OH concentration. This demonstrated our lack of understanding on sources and sinks of methane and highlighted the

importance of a rigorous emission quantification method.

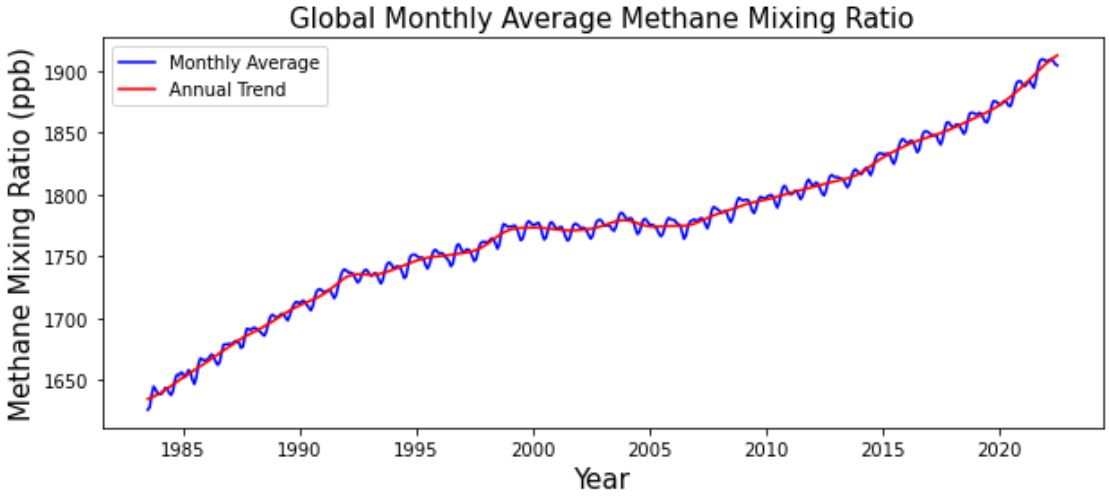

Figure 1.3: Blue line indicates globally averaged monthly mean value of methane centered on the middle of each month. Annual trend is depicted by a red line from 12-month running mean. (NOAA Earth System Research Laboratories).

Understanding the global budget of methane has a great appeal to policy makers to mitigate climate change. Accordingly, it requires a development of accurate methane emission inventories to assess the effectiveness of mitigation strategies. Field measurements and monitoring of emission sources can provide an improved understanding of site-specific processes behind the emissions as well as regional- and urban- scale plans to control the emissions.

1.2.Measurement of Methane

Bottom-up greenhouse gas inventories, often prepared at the national level by governments, are used to assess the magnitude and sources of greenhouse gas emissions to track trends over time and evaluate an effectiveness of mitigation efforts. They are constructed by 4 different methods, including direct measurement and mass balance method which include performing direct facility scale measurement of methane emissions. Often, model estimates are formed from an emission factor (e.g., emission per livestock or facility) and multiplying this emission factor by the activity data (e.g., number of livestock, natural gas usage, etc.) and based on engineering estimates which is the model estimates of emissions based on scientific principles. Small scale instantaneous measurements methods such as flux chamber techniques (static and dynamic) and micrometeorological techniques (e.g., eddy covariance and aerodynamic gradient method) provide individual source emission factor (Burba et al., 2013 and Zhao et al., 2019).

Chamber techniques cover small surface area of a source (~ 1 m^2) with a chamber to measure the flux of gas over short time period. For non-reactive greenhouse gases such as methane (CH_4) and nitrous oxide (N_2O) fluxes, a static chamber method is most commonly performed in which diffusive methane is quantified directly from the change in methane concentration for a chamber covering known volume/area (Pihlatie et al., 2013). Dynamic chambers allow flow of gas that the emission rate of gas is quantified based on the difference between inlet and outlet concentration. These techniques often provide useful information about methane variability. Yet, it is only able to cover a small area that may not represent the whole source and they are labour intensive requiring multiple measurements over a number of small areas necessary to cover a large source.

Micrometeorological techniques such as eddy covariance are based on characterizing the turbulent transport of gas by eddies within the lower troposphere from single-point on site measurements. The method employs fast response methane and wind sensors on stationary or mobile towers to obtain methane concentration and wind components at high frequency of 10 or 20 Hz (Burba et al., 2013) to calculate the covariance between the wind speed component to methane concentration. On the other hand, the aerodynamic gradient method is used to analyze the vertical concentration gradient through turbulent diffusion. Vertical flux is measured by making concentration measurement at two different altitudes simultaneously (Zaman et al., 2021).

Direct small scale on-site measurements of methane emission can provide important insight to site-specific processes that lead to emissions. This can contribute to the development of process-based emission models for the accurate bottom-up inventory as well as effective mitigation strategies, especially sources including multiple hotspots. However, it is not ideal measurement type to observe any long term spatial and temporal variations since it requires a large number of individual measurements, and the measurement is time consuming.

Recent measurements of methane include more regional scale analysis by top-down techniques from aircraft mass balance (Gordon et al., 2015 and Baray et al., 2018), surface mobile measurement (Baray et al., 2021) or satellite remote sensing and inverse modelling (Jacob et al., 2022). In the aircraft mass balance method, aircraft are often flown at upwind and downwind transects of the study region, involving different flight methods. Single height transect

measurement assumes well mixed boundary layer to calculate the mass flux of methane. Spiral pattern fight can determine the vertical profile of methane and alternatively, multiple measurements can be performed at different heights on a single transect to form two-dimensional screen perpendicular to the horizontal wind direction. Measurement of methane flux perpendicular to the wind direction on the horizontal transects is integrated along the transect and from the bottom to top of the boundary layer height to estimate the emission rate. The box method is developed from the two-dimensional screen to include multiple screens surrounding the emissions area. Top-down emissions rate retrieval algorithm (TERRA) developed by Gordon et al. (2015) employed the box method to calculate the integrated mass flux through the walls of box containing the Alberta's oil sands facilities.

Due to the availability and efficiency, many studies have been performed using satellite observations to quantify global methane (Jacob et al., 2016, and Zhang et al., 2020). Satellite retrieval obtains the methane columns by measuring the backscattered solar radiation in shortwave infrared (SWIR). Satellite measurements of atmospheric CH_4 can be performed by thermal and near-infrared sensor of Fourier Transform Spectrometer (TANSO-FTS) operated on the Greenhouse Gases Observing Satellite (GOSAT), and the Tropospheric Monitoring Instruments (TROPOMI) onboard the Sentinel-5 Precursor satellite. Satellite monitoring provides wide global coverage and consistency in year-round observation that could highlight the global methane trend by countries and any seasonal and annual variability. However, remote sensing of the GHGs has several challenges as well, including poor resolution, effects from the surface albedo and viewing angle, interference from the clouds, aerosols, and potential space debris and measurements often limited to a single overpass per day. Therefore, it is essential for the space-based observation to be compared with ground-based observations.

Recent comparison of top down and bottom-up estimates have constantly demonstrated that top-down estimates are generally 1.5 – 2 times larger than bottom-up emission inventory values (Miller et al., 2013, Zavala-Araiza et al., 2015, Vaughn et al., 2018, and Baray et al., 2018). It is crucial for bottom-up estimates to have accurate representation of total emission and relative contribution of different sources since the inventory is often used as a guide for policy decisions.

Simple multiplication of activity data by emission factors is often inappropriate to estimate the anthropogenic methane emission, especially from landfills and natural gas facilities. Emissions

from microbially driven sources such as landfills highly depends on the factors such as waste composition, temperature, pH and moisture content of wastes and soil as well as meteorological conditions such as ambient temperature, and pressure. These site-specific parameters can cause large temporal and spatial variability that often fail to correctly estimate the methane emission rate at an annual level.

Several studies (Zavala-Araiza et al., 2017, and Cusworth et al., 2022) have also emphasized that bottom-up techniques fail to characterize the super-emitters where small number of facilities contribute to a formidable portion of the total emissions. Oil and gas infrastructures can also show temporal and spatial variability that annualized estimates by emission factors are inadequate to accurately distinguish local emission occurring within short timescale. For instance, maintenance activities performed by operators during daytime work hours (manual liquid unloading, or depressurization of equipment) can trigger high level of emission rates for just a short period of time.

Accordingly, it is important to have top-down measurements of methane to be compared with bottom-up inventories and satellite imageries to fully characterize the source and understand the temporal emission trend. Yet, regional scale measurement techniques (e.g., aircraft mass balance) has multiple disadvantages including high costs, intensive labor, and limitation to the method if only a single transect measurement is made which may not be able to capture all variability in emissions. Surface level mass balance employing a mobile vehicle with a methane spectrometer can be more beneficial to perform measurement over the operating domain at a much reasonable cost, and efficiency compared to aircraft study.

1.3.Introduction to Mass Balance Method

Figure 1.4 shows the schematic diagram of the mobile mass balance method that were employed to quantify the methane emissions from Greenlane landfill and the industrial complexes of Sarnia in Chapter 3 and 4.

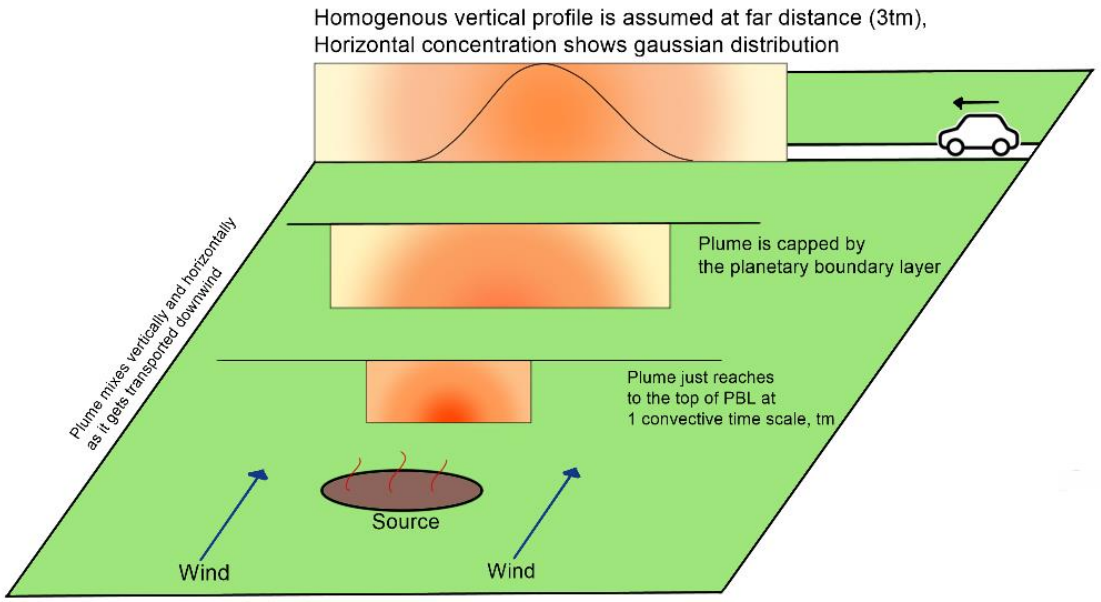

Figure 1.4: Schematic diagram of mobile mass balance method

The concept of mass balance is an application of conservation of mass to the analysis of the mass flows entering and leaving a system. As the pollutants emitted from the sources get transported by wind, the flow of mass by the wind can be expressed as a mass flux vector field:

$$j = \rho v \qquad (1.15)$$

where ρ is the mass density (mass per unit volume) and v corresponds to the velocity field of the wind.

For an imaginary 2D horizontal surface *A*, that is located at the downwind transect of the source at distance, *x*, the rate of mass, $\frac{dm}{dt}$ *or* $\dot{m}$, flowing through the surface is defined as:

$$\frac{dm}{dt} = \dot{m} = \iint_A \rho v \cdot dA \qquad (1.16)$$

Mass density of the target pollutant species, *i* can be written as $\rho_i = X_i n_{air} \frac{MW_i}{Av}$ (enhanced mixing ratio of component *i* above its background, X_i, number density of air, n_{air}, molecular weight of *i*, MW_i, and Avogadro's number, *Av)* and with the velocity field, v equivalent to the wind velocity $\vec{V}(x, y, z, t)$:

$$\dot{m} = \iint_A [X_i n_{air} \frac{MW_i}{Av}] \vec{V}(x,y,z,t) \cdot dA \quad (1.17)$$

If steady flow of the wind is assumed, $\frac{\partial \vec{V}}{\partial t} = 0$ with only the mass flowing through the cross section and only consider the component of wind parallel to the unit normal $\hat{n}$ which is in the *x*-direction downwind of the source with θ as the angle between the horizontal transect and the incoming wind angle:

$$\dot{m} = \iint_A [X_i n_{air} \frac{MW_i}{Av}] v(x) cos(\theta) \cdot dA \quad (1.18)$$

If the transect surface is assumed to be 2-dimensional vertical plane of transect length, S and the height confined by the planetary boundary layer, Z_{BL} (on the y-z plane):

$$\dot{m} = \int_{S1}^{S2} \int_0^{ZBL} [X_i n_{air} \frac{MW_i}{Av}] v(x) cos(\theta)\, dSdZ \quad (1.19)$$

Equation 1.19 is the conventional mass balance equation to calculate the mass flux of the gas. In order to apply the equation, the wind needs to be consistent in speed and direction during the measurement and within the planetary boundary layer. However, wind velocity, pressure and temperature are known to depend on height and a change in equation is required for more accurate quantification of methane if the measurement is limited to surface and vertical measurements of wind speed cannot be not made. Wind velocity in the *x*-direction can be measured at a ground station but the wind will not necessarily be consistent with height within the planetary boundary layer, Z_{BL}.

For the boundary layer's turbulent mixing, an idealized vertical profile model of the wind for a neutral boundary layer can be described by the logarithmic profile derived from Prandtl's mixing length theory (Peña, 2009) and wind profile power law. Based on the power law, near-surface wind speed can be extrapolated by:

$$v_z = v_r (\frac{z}{z_r})^{\alpha} \quad (1.20)$$

For the wind speed at height z, v_z can be calculated by the wind speed measured at a reference height, r, usually at a ground station with r = 10m. The wind profile exponent, α depends on the stability of the atmosphere and the effect of surface roughness. The parameter is obtained from

the U.S. EPA model, ISC3 dispersion model ("Industrial Source Complex") algorithm which is often used to estimate dispersion and concentration of air pollution from industrial sources over short periods (~ 1 hour) within short distances (< 50 km) of the source. The wind profile exponent used in the calculation can be found in Appendix A1.

Assuming non-uniform wind velocity depending on height, the modified mass balance equation is given by:

$$\dot{m} = \int_{S1}^{S2} \int_{0}^{ZBL} [X_i n_{air} \frac{MW_i}{Av}] v_r (\frac{z}{z_r})^{\alpha} cos(\theta)\, dSdZ \quad (1.21)$$

As number density of air is given by, $n_{air} = \frac{P(Z)}{RT(Z)} Av$, above equation can be rewritten as:

$$\dot{m} = \int_{S1}^{S2} \int_{0}^{ZBL} X_i \frac{P(Z) MW_i}{RT(Z)}\, v_r (\frac{z}{z_r})^{\alpha} cos(\theta)\, dSdZ \quad (1.22)$$

Pressure, P(Z) and temperature, T(Z) change according to altitude based on barometric laws and lapse rate. However, the integral involving changing P, and T by height result in complicated integrals that can only be estimated by numerical integration which require onsite vertical pressure and temperature profile. It is also expected that the change from these two variables is relatively less significant. For instance, temperature variation within 1 km of boundary layer would equal to ~ 9.8 °C if adiabatic lapse rate is assumed compared to 1000 m boundary layer height. Therefore, if P and T area assumed to be constant with height, separating variables and integrating gives:

$$\dot{m} = v_r \cos(\theta) \frac{{Z_{BL}}^{\alpha+1}}{{Z_r}^{\alpha}(\alpha+1)} \frac{PMW_i}{RT} \int_{S1}^{S2} [X_i]\, dS \quad (1.23)$$

Enhancement above the background $[X_i]$, is measured by the mobile vehicle carrying the methane spectrometer and travelling along the transect of length, S. However, full vertical profile of methane is unachievable by this single altitude measurement at surface level. Therefore, for the method to be valid, it requires homogenous mixing of methane within the boundary layer, so the vertical profile is consistent with height. The measurement is limited to days when planetary boundary layer (PBL) is convective from strong insolation to cause mixing and measurement transects need to be sufficiently far away as methane plume takes time to mix into the boundary

layer. Wind parameters need to be assumed consistent in speed and direction during the measurement period.

1.4.Boundary Layer Meteorology

1.4.1. Atmospheric Mixing and Stability

The atmospheric boundary layer is the lowest part of the troposphere that is strongly influenced by earth's surface and surface fluxes induced by solar and IR radiative forcing. (Stull, 2017) The diurnal cycle of radiative heating creates a cycle of static stability within the boundary layer. Depending on the buoyant force exerted on an air parcel, the stability can be classified as being stable, unstable, or neutral that can be described by the potential temperature of the air parcel. The potential temperature refers to the temperature of a dry air parcel would experience if it were to be brought adiabatically to the standard reference pressure of 1000 hPa.

For a stable boundary layer, the surface is cooler than the air above. Therefore, the air parcel experiences increase in potential temperature that the denser surface air cannot be lifted and sinks down. This resists the vertical motion and causes stable laminar flow of air on the surface in absence of other forces. On the other hand, if the air parcel experiences decreasing potential temperature, it continues to accelerate upward, with strong turbulence created within the boundary layer. This condition is classified as an unstable boundary layer. When the vertical gradient of potential temperature equals to the adiabatic lapse rate the boundary layer is considered to be neutral.

Turbulence eddies by the upward drifts of air parcel mixes the air within the boundary layer which creates uniform potential temperature per height, creating a convective boundary layer (CBL). Stable layer of air that forms on the top of mixed layer creates a sharp temperature inversion which caps the surface-induced turbulence and air pollutions within the mixed layer. In the event of weak advection by the surface wind, the convection by the solar radiation and clouds determines the stability of the atmosphere. Pasquill-Gifford (PG) stability types estimate the amount of turbulence depending on those two forcings. Table for the PG stability classes can be found in Appendix A2.

In order for the surface mass balance to be valid, it requires a relatively unstable stability condition in which moderately turbulent surface air mixes the air pollutants vertically well within the mixed layer. It also needs to allow the pollutant plumes to be transported downwind of the source with sufficient surface wind speed, *v*, which is required to be within the limit given by equation 1.24 (Deardorff and Willis, 1975):

$$1.5\ w^* < v < 6\ w^* \qquad (1.24)$$

Deardorff velocity *w**, is the convective velocity scale that represents the rate of vertical mixing, given by equation 1.25:

$$w^* = \left[\frac{g}{T} Z_{BL} F\right]^{\frac{1}{3}} \qquad (1.25)$$

$\frac{g}{T}$ term corresponds to buoyancy parameter for an ideal gas, for the height of free convective boundary layer, Z_{BL} caused by the kinematic heat flux, F near the surface. This is true for a downwelling solar irradiation, S that the F = $\frac{S}{\rho_{air} C_p}$ where $\rho_{air} C_p$ denotes density and heat capacity of the air.

If the surface wind is too weak and speed is below the limit given by the equation 1.24, the wind is relatively weaker than the eddies and plumes cannot be efficiently transported. Moreover, if *v* is too strong, the wind shear dominates the movement of the plume and competes with the thermal convection.

As Deardorff velocity describes the rate of plume rise, the time for a conservative tracer to reach the top of the boundary layer can be defined as:

$$t_m = \frac{Z_{BL}}{w^*} \qquad (1.26)$$

Based on the convection study by Deardorff and Willis (1975), plume from source is expected to be well mixed vertically when it reaches the timescale of $3 \cdot t_m$.

1.4.2. Gaussian Plume Dispersion

Air pollution models incorporate meteorological and direct measurement data such as emission rates, temperature, and wind parameters to characterize the pollutant dispersion downwind of the source. The models often play a key role in air pollution regulation and air quality management as it is an effective strategy to monitor the contributions of individual facilities to the air quality problems in a region. For example, the impact of industrial operations or power plants on pollutant emission can be modelled to show whether emissions from a power plant exceeds the regulatory level or not. The atmospheric dispersion model can be used for inverse modelling to estimate the advection of pollutant plume, predicting its movement from a source to a downwind receptor location.

Popular dispersion models such as ISCST3 (Industrial Source Complex – Short Term Regulatory Air Dispersion Model) and AERMOD (the American Meteorological Society/Environmental Protection Agency Regulatory Model Improvement Committee's Dispersion Model) by U.S. EPA are based on the steady state Gaussian dispersion model. Horizontal and vertical spread of a plume from a point or an area source are normally distributed and expand in double gaussian distributions (*y* and *z*) downwind of the source. The condition of plume spread, and shape vary in response to meteorological parameters that creates forcing within the mixed layer.

The Gaussian concentration distribution is a solution to the general diffusion equations. For a lateral dispersion, the shape of lateral concentration profile is given by the gaussian distribution:

$$C_{x,z}(y) = \frac{1}{\sigma_y(x)\sqrt{2\pi}} e^{\left(-\frac{y^2}{2\sigma_y^2(x)}\right)} \quad (1.27)$$

$\sigma_z(x)$ and $\sigma_y(x)$ are called vertical and horizontal dispersion coefficients (standard deviation from the centerline) that depend on downwind of the source, *x*. Plume spread parameters are empirically driven from field experiments and there are various parameter types depending on the model (ISC, and AERMOD). For simplicity, magnitude of dispersion coefficients is calculated by the Martin scheme (1976) in the following chapters where each dispersion parameters are given by:

$$\sigma_y(x) = ax^b \quad (1.28)$$

$$\sigma_z(x) = cx^d + f \quad (1.29)$$

Both the lateral and vertical spreads only depend on the classified stability category and location of downwind distance, *x* from the source where *a*, *b*, *c*, *d*, and *f* are stability dependent variables. Variables for the Martin Schemes are found in Appendix A3 and A4.

The vertical profile is given by the same equation as 1.27. Therefore, two-dimensional concentration profile on y-z plane is given by multiplying the two gaussian functions:

$$C_x(y,z) = \frac{1}{2\pi\sigma_y(x)\sigma_z(x)} e^{\left(-\frac{y^2}{2\sigma_y^2(x)}\right)} e^{\left(-\frac{z^2}{2\sigma_z^2(x)}\right)} \quad (1.30)$$

For the plume moving along *x*-axis, the three-dimensional distribution of plume concentration, C(*x*, *y*, *z*) can be given by the equation:

$$C(x,y,z) = \frac{Q}{2\pi\sigma_y\sigma_z v} \exp\left[-\frac{y^2}{2{\sigma_y}^2}\right]\left\{\exp\left[-\frac{(z-h)^2}{2{\sigma_z}^2}\right] + \exp\left[-\frac{(z+h)^2}{2{\sigma_z}^2}\right]\right\} \quad (1.31)$$

where Q denotes for the source rate in g/s, with *v*, surface wind velocity in m/s that carries the plume from h, the effective stack height of source released above ground (m) which is the sum of stack height, h_s with plume rise, Δh. The reflection of the methane plume off the ground is considered in the full Gaussian formulation of 1.31. However, without a term that considers the reflection from the capped inversion layer, the model is only assumed to be accurate before the methane plume reaches the top of the boundary layer (i.e. within close distances from the source).

If only the concentration at the ground level, z = 0, is considered, the equation 1.31 can be simplified to:

$$C(x,y,z=0) = \frac{Q}{\pi v\sigma_y\sigma_z} \exp\left[-\frac{y^2}{2{\sigma_y}^2}\right] \exp\left[-\frac{h^2}{2{\sigma_z}^2}\right] \quad (1.32)$$

Further simplification of equation at the plume centerline, y = 0 yields:

$$C(x, y = 0, z = 0) = \frac{Q}{\pi v \sigma_y \sigma_z} \exp\left[-\frac{h^2}{2{\sigma_z}^2}\right] \quad (1.33)$$

If the plume is assumed to be emitted from ground (stack height, $h_s = 0$) which is true for landfills, h in equation 1.33 will only depend on the plume rise, Δh. The parameter, Δh depends on the nature of the source and the atmospheric condition. In general, plume rise is proportional to the exit velocity of the plume from the source while inversely proportional to the wind speed. Moreover, plume rise is also proportional to the buoyancy parameter, which implies that the more unstable atmosphere with strong turbulent kinetic energy will have higher plume rise. There exist multiple methods of plume height estimation such as Holland formula and Briggs algorithm (Carson and Moses, 1969). However, due to the complexity of applying correct empirical estimation for the studies, a simplification of equation 1.33 will be made on the assumption that plume rise is minimal, $\Delta h \approx 0$. This simplified gaussian model can be applied to the enhancement observed at very close transects when there exists weak turbulence and strong surface wind to produce neutral stability. Assuming h = 0 in equation 1.33 results in simplified gaussian model equation of 1.34:

$$C(x, 0, 0) = \frac{Q}{\pi \sigma_y \sigma_z v} \quad (1.34)$$

1.5.Objectives of the Thesis

The main objective of this thesis is to develop an efficient and accurate alternative regional scale mass balance method to quantify methane from mobile surface measurement as an alternative to the conventional aircraft mass balance method. The goal is to measure the mixing ratio of methane at downwind transects of various sources (landfills, and industrial facilities) and quantify methane assuming the homogenous vertical profile of methane at distance when the methane is "well-mixed" (3 t_m) within the convective boundary layer. In order to verify the accuracy of the method, the emission rates will be compared to other modelling such as landfill gas emission model by U.S. EPA and gaussian dispersion models as well as the inventory values.

Chapter 2 and 3 aim at exploring the Ontario's two main landfills, Keele Valley landfill and Greenlane landfill. Chapter 2 focuses on the instrumental characterization of Tunable Diode Laser Spectrometer (TDLAS) and Cavity Ring down Spectrometer (CRDS) that are used in the

studies. General driving studies around Keele Valley landfill are performed to inspect if the landfill is still emitting considerable methane even after 20 years of its closure.

Chapter 3 is centered on quantifying methane emissions at Greenlane landfill by the surface-based mass balance method from 4 different studies performed through 2021-2022. Observed methane enhancements are characterized to identify the pattern in emission to locate potential hotpots from the landfill. Calculated emission rates of methane are compared with the inventory to confirm if the top-down measurement from Greenlane landfill also yields higher emission estimates than the bottom-up estimates. By performing multiple studies at different time of the year, any seasonal variability, and effects of meteorological parameters (e.g., temperature and pressure) on the methane emission from landfills are discussed. Moreover, carbon dioxide emission rates are also calculated from methane emissions rates through a simple correlation analysis.

Chapter 4 focuses on identifying the methane sources from the city of Sarnia, including its significant industrial complexes where major petrochemical facilities are located. The city of Sarnia has various oil refineries, chemical manufacturing, cogeneration power plants and natural gas pipelines that can directly emit or leak unknown quantities of methane, yet to our knowledge, there has not been any study to quantify them. Moreover, the emissions from the region can include other small sources such as natural gas use from residential buildings, agricultural activities, farms, and stables in and around the city. The key research aim is to analyze surface-based mass balance method for quantifying methane from oil and natural gas infrastructures compared to landfills which can highlight the effectiveness of the method in identifying emission rates from different types of sources.

Chapter 2 : Keele Valley Landfill Measurements

2.1. Introduction

As the second most important anthropogenic greenhouse gas next to carbon dioxide, methane has a radiative forcing of 0.48 Wm^{-2} which accounts for 23% of the radiative forcing by GHGs in the atmosphere. (Ramaswamyet al., 2001) While methane has a comparatively low lifetime of 9 years compared to carbon dioxide, methane's 20 years global warming potential is 84 times greater than that of CO_2 on a mass basis. (Myhre et al., 2013) This implies controlling the methane emissions will have greater impact to climate for the next two decades.

The increasing waste generation due to growth in population and urbanization has caused a major challenge for municipalities to dispose of increasing quantities of waste. Since the waste sector proves to be the second largest anthropogenic source of GHG, emitting both methane and carbon dioxide, the mitigation of GHG from the increasing waste must be addressed in the process of waste management.

Figure 2.1 shows the schematic diagram of the landfill methane mass balance. The emitted methane from the landfill is only a portion of the generated methane as methane can be collected by the gas collection pipes and lost by aerobic oxidation on the soil surface.

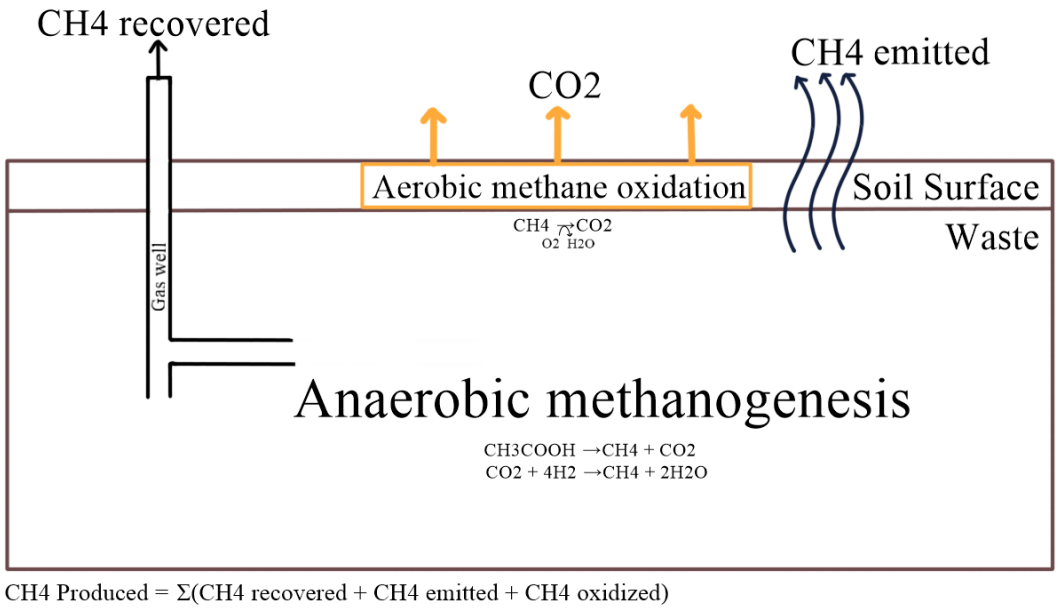

Figure 2.1: Diagram of landfill CH_4 mass balance where methane produced equals to sum of methane emitted, oxidized by methanotrophs, and recovered by gas wells.

Organic matter deposited in the landfill undergoes several fermentation processes where carbohydrates are converted to acetate and H_2. In the final step of its degradation, methanogenesis by anaerobic bacteria breaks down acetate into carbon dioxide and methane (Meyer-Dombard et al., 2020) in a 1:1 molar ratio.

$$CH_3COOH \rightarrow CH_4 + CO_2 \quad (2.1)$$

Methane can also be produced from reduction of CO and CO_2 to methane by H_2 as reductant.

$$CO_2 + 4H_2 \rightarrow CH_4 + 2H_2O \quad (2.2)$$

$$CO + 3H_2 \rightarrow CH_4 + H_2O \quad (2.3)$$

It is estimated that the landfill gas (LFG) from the landfills is composed of roughly 40-60% CH_4 and 40-60% CO_2 by volume with trace amounts of volatile organic compounds and other pollutants of less than 1%. However, only a portion of produced landfill methane gets emitted. LFG in most municipal landfills is captured by the gas wells where the pipes are buried in the landfills vertically and horizontally to collect emitted LFG. Collected LFG is treated by removing moisture, impurities such as siloxane and sulfur, and CO_2 to collect purified methane that can be compressed to be used as fuels for electricity generation or flared to destroy excess gas (U.S. EPA). Methanotrophic microorganisms also reduces the produced methane from the landfill by oxidation on the soil surface. Aerobic methane oxidation by methanotrophs convert methane to methanol which is further oxidized to formaldehyde and converted to CO_2 on final stage (Guerrero-Cruz et al., 2021).

Keele Valley Landfill (KVL), located in Vaughan, Ontario, operated from 1983 to 2002. As the largest landfill in Canada, it accumulated a total of 28 million tonnes of waste. Even 21 years after its closure, KVL is suspected to emit large amount of methane. In previous years, the GreenHouse Gas Reporting Program (GHGRP) estimated Greenlane landfill to emit roughly 20 kt of methane per year which sharply dropped to 9.8 kt and 11 kt in 2019 and 2020 respectively (Figure 2.2). These methane emissions were reported by direct measurement of methane from on site monitoring between 2010 to 2015, then estimates were calculated by emission factor between 2016 to 2018 and by engineering estimates between 2019 and 2020. The cause of this drastic drop in methane emissions in recent years may be due to the change in estimation methods. Yet, the apparent reason for this discrepancy is unknown. Even after this decline in the

emission estimate, methane from KVL is still ranked as 3rd largest methane source in Ontario accounting for 4.7% of 207 kt of total methane from Ontario which includes methane emissions from all sectors (Figure 2.3).

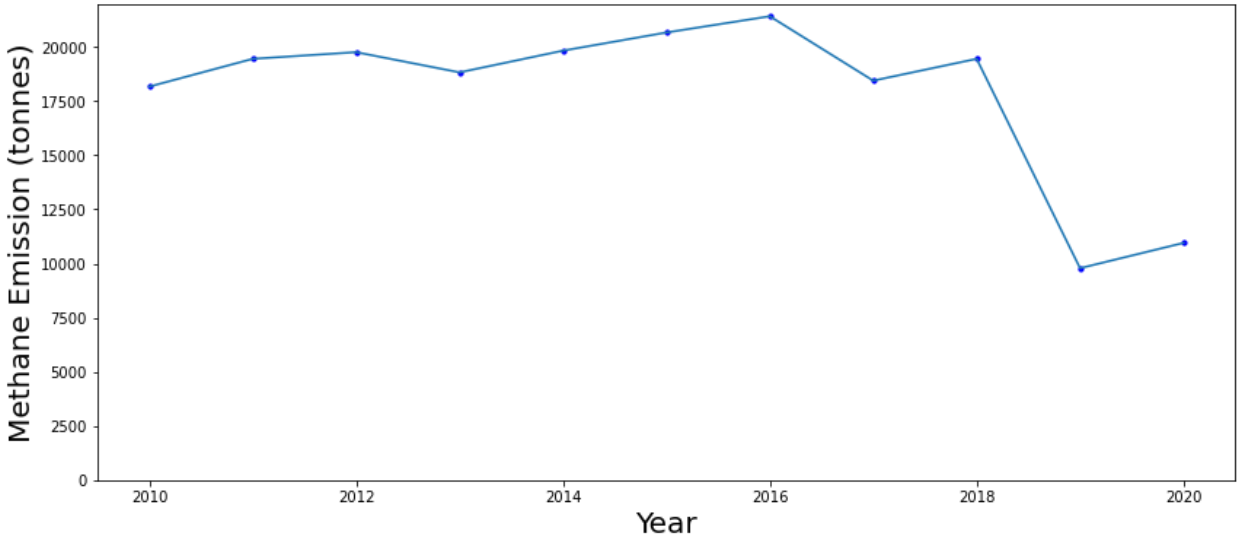

Figure 2.2: Annual reported methane emissions (in tonnes) at Keele Valley Landfill from GHGRP past decade to 2020. Emission values are estimated by either engineering estimates or emission factor depending on year.

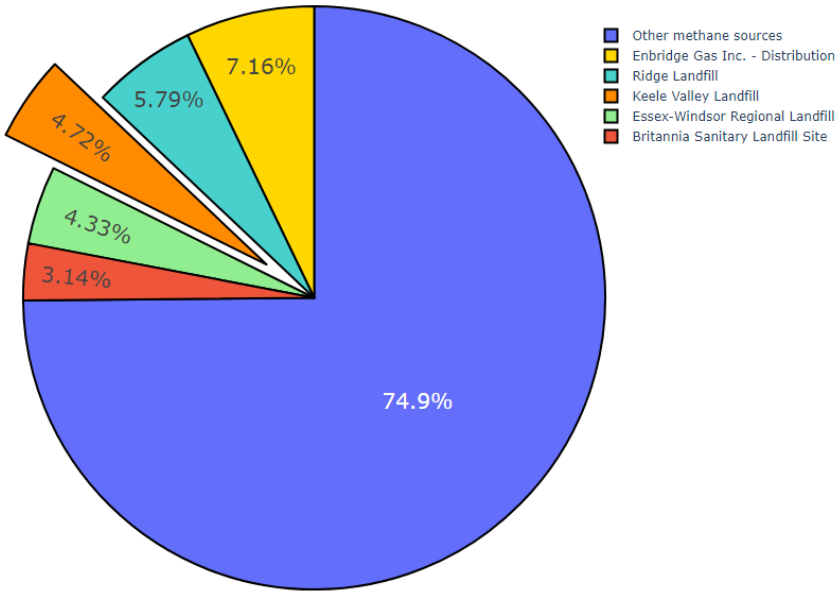

Figure 2.3: Ontario's methane emission in 2020 reported by GHGRP (Total: 207 kt including all sectors) with top 5 methane source named, with KVL as 3rd largest source (9.8 kt or 4.7%).

Measurements of methane were performed at the Keele Valley landfill sites by Tunable Diode Laser (TDL) absorption spectroscopy and Cavity ringdown spectroscopy (CRDS). The study aimed at validating and investigating the performance of instruments and to observe methane enhancements emitted from KVL by performing upwind and downwind measurements and driving around the landfill.

The current annual emission rate by GHGRP is also compared to a methane generation rate estimated using the landfill gas emission model (LandGEM) by U.S. Environmental Protection Agency. The model is used to estimate the total landfill gas generated, including methane, from landfills. The model employs a first order decomposition rate equation:

$$Q_{CH4} = \sum_{j=1}^{n} \sum_{j=0.1}^{1} kL_o(\frac{M_i}{10})e_{ij}^{-kt} \quad (2.4)$$

Q_{CH4} is the estimated methane rate, n = years of operation, i,j = 1 year and 0.1-time increment each, k = methane generation rate, L_o = potential methane generation capacity, M_i = mass of solid waste disposed in i^{th} year, t = age of the j^{th} section of waste mass disposed in the i^{th} year.

2.2. Experimental Methods

2.2.1. Instrumentation

A LasIR Gas Analyzer (Unisearch Association Inc.) was employed to measure the methane mixing ratios at downwind locations of the landfills. The internal components of the instrument are depicted in Figure 2.4. The instrument uses a near IR tunable diode laser (TDL) to measure the concentration of target species along the path length by the principles of absorption spectrometry:

$$\text{Transmittance} = \frac{I_t}{I_0} = e^{-\sigma NL} \quad (2.5)$$

Transmittance is the ratio of transmitted light intensity compared to the incident light intensity. Cross section of the target species can be represented by, σ in $cm^2molecule^{-1}$, along with number density of the gas in $molecules \cdot cm^{-3}$ and path length of the media, L in cm.

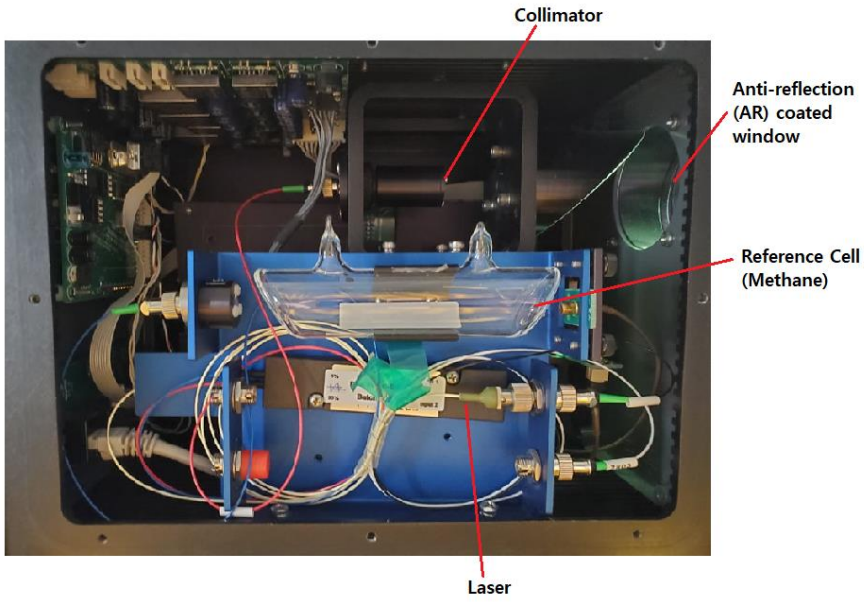

Figure 2.4: Picture of the internal components of TDL with major optical components labeled.

The TDL scans across an absorption line of methane by tuning the output wavelength of the diode laser. The emission wavelength of the laser is tuned over the transition in the $2\upsilon_3$ vibrational absorption band of methane at 1.65 μm where the absorbance is narrow (0.06 nm FWHM) and has the least interference from other atmospheric species, such as CO_2 and H_2O (Paige et al., 2006).

The LasIR TDL has open path transmission optics employing a gold-plated retroreflector to return the beam back to the instrument. This dual pass system creates greater path length and increased sensitivity while open path configuration allows acquisition of real-time data of high temporal resolution (200 μs). The TDL can be used in upwind-downwind method to observe the enhancement of methane in the area. Subtraction of upwind background data from the downwind data shows the enhancement of methane concentration in the target area and is also capable of depicting the temporal variation in the methane flux by its extremely fast response time < 1s.

The Cavity Ringdown Spectrometer (CRDS)(model: G2401-m) from Picarro incorporates three single-frequency laser diodes in a cavity of three highly reflective mirrors (R~99.99%) to simultaneously measure the mixing ratios of CH_4, CO_2, CO, and H_2O (Figure 2.5).

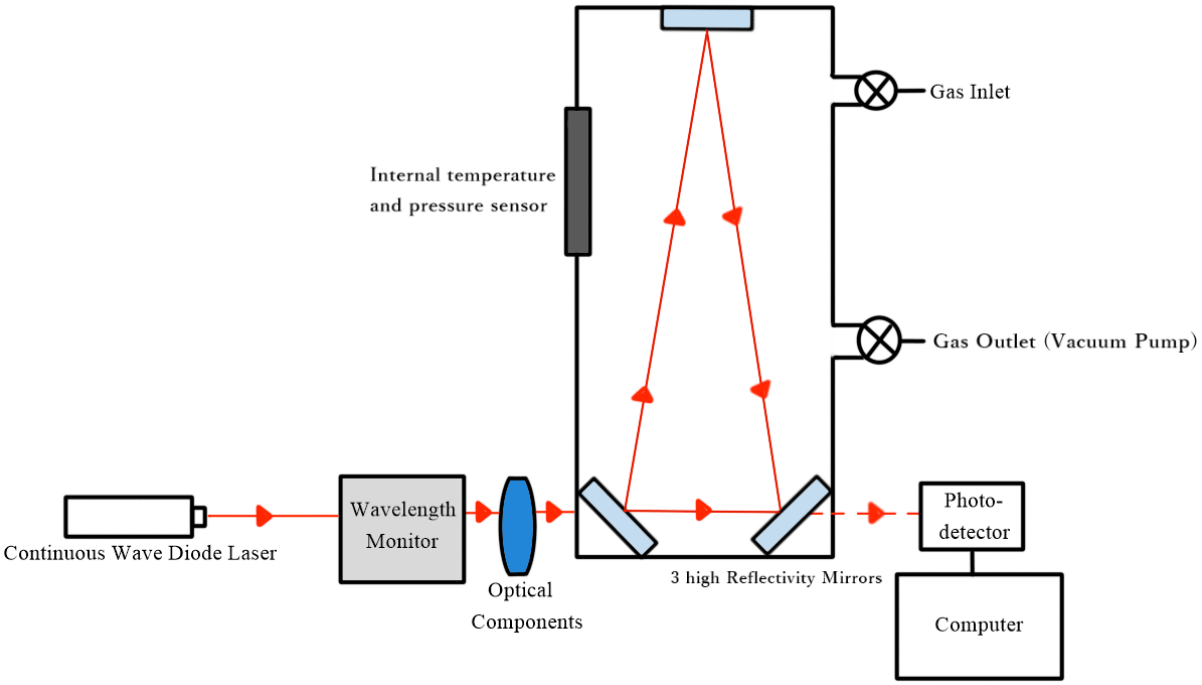

Figure 2.5: Diagram of CRDS system.

When the photodetector detects a threshold level of signal, the light source is turned off and light introduced within the cavity slowly decays in intensity as a small portion of light escapes. The difference in ringdown time between the empty cavity and cavity with the gas is used to calculate the concentration of target species. Therefore, unlike absorption spectroscopy, CRDS measures the decay rate (ringdown time) of light from the cavity to determine the concentration of the gas within. This configuration creates a pathlength of over 10 km and the multipass nature grants CRDS extremely high sensitivity. Moreover, as the relative ringdown time is independent of fluctuation in laser intensity, the instrument is seen as an adequate standard for comparison with other spectrometry instruments. The Picarro CRDS maintains a constant cavity temperature and pressure of ~45.0 °C and 140 kPa. The low sampling pressure narrows the spectral line widths by limiting the effect of pressure broadening. This closed configuration makes CRDS robust, best stability in measurement. Filtering of the sample air that enters the cavity, narrow

spectral bandwidth of CRDS lasers as well as short measurement time in order of nanoseconds minimize the effect of any aerosol particles in the sample to minimize the aerosol extinction.

The Picarro CRDS was employed for the mobile measurement around the Keele Valley Landfill. The instrument was mounted inside a Tesla vehicle operated using a Goal Zero Yeti marine battery. The inlet was connected by a polytetrafluoroethylene (PTFE) tubing and mounted 1 m above the ground onto the sideview mirror of the vehicle. The temporal offset by the tubing was measured by introducing sample air to measure the average delay time (~ 11 s) and was used to correct the measurement time. A GPS app was used to measure the position of latitude and longitude which was used along with CRDS data to construct mixing ratio map of methane.

2.2.2. Upwind and downwind sampling of methane

Methane enhancements around the KVL landfill were performed with the TDL on July 12th 2021 between 2:07 – 4:43 PM (EST). One upwind location and two down wind locations were selected according to the wind direction (Figure 2.6). Wind data was obtained from EMOS station at York University which is appxoimately 11 km far way from the landfill site as this site provided the data of wind speed and angle closest to the meausrement locations. For all meausrmenet locations, the retroreflector was placed 56 m away from the laser optics which provided the path length of 112 m, and distance was measured by using a laser range finder that measured the distance between the TDL instruemnt and the retroreflector.. The instrument set up onsite is shown in Figure 2.7. Dwell time of the instrument was set to 5 seconds based on the preliminary experiments performed to characterize the performance of TDL since 5 seconds was optimal to capture real time changes in methane flux while having precision of ±3 ppb.

Figure 2.6: Map of upwind and downwind site locations and landfill sites highlighted in red (Keele Valley Landfill) and purple (Vaughan township landfill). Wind blowing from east.

Figure 2.7: Pictures showing the set up of TDL at measurement downwind location 1 where retroreflector was placed 56 m away from the TDL instrument powered by the battery mounted in a car.

2.2.3. Driving study with CRDS

On October 13th, 2021, a driving study was conducted around the KVL and in the city of Vaughan, ON between 2:15 – 4 PM (EST) to identify the level of methane enhancements from KVL as well as any potential local sources of CH_4. The measurement locations were mostly focused on observing potential fugitive methane emission from TransCanada pipelines and compressor stations at 130 Maple station and along the Dufferin street to the east of the KVL. The forecast wind direction was NE during the survey and the driving routes were chosen such that the wind direction would allow measurements of methane enhancements at the downwind locations.

2.3. Results and Discussion

2.3.1. Observation of methane emissions from the KVL using TDL

Table 2.1 provides a summary of the measurement made at two downwind and an upwind location. The wind condition was gentle with low-speed ranging between 2 – 3 m/s. The local wind blowing from SE which was slightly different from the York's EMOS data (East) since the station at York is 11 km away from KVL location.

Table 2.1: Summary of measurement period and wind data obtained from EMOS station for each measurement site on July 12th, 2021.

	Measurement Period (EST)	***Longitude***	***Latitude***	***Wind speed (m/s)***	***Wind angle (deg)***
Downwind 1	14:07 – 14:37	43.8665	- 79.5154	2.5 ± 0.5	87 ± 20
Upwind	15:16 – 15:46	43.8676	- 79.4888	3.3 ± 0.8	83 ± 30
Downwind 2	16:12 – 16:42	43.8717	- 79.5224	3.3 ± 0.9	73 ± 20

Enhancements of methane mixing ratio at downwind sites were observed over 30-minute measurement period compared as in Figure 2.8 and intercompared to the upwind data in Figure 2.9. The upwind data showed nominal change in observed methane mixing ratio, representing background value of 1.933 ± 0.006 ppm. Each of downwind site showed methane mixing ratio of 1.99 ± 0.03 ppm (site 1) and 2.04 ± 0.04 ppm (site2). The respective enhancement at downwind site 1 was 57 ppb, and 111 ppb at downwind site 2. Twice the enhancement was observed at

downwind 2 location which implied the downwind 1 location was not fully capturing the methane plume from the landfill. These observed enhancements are summarized in table 2.2.

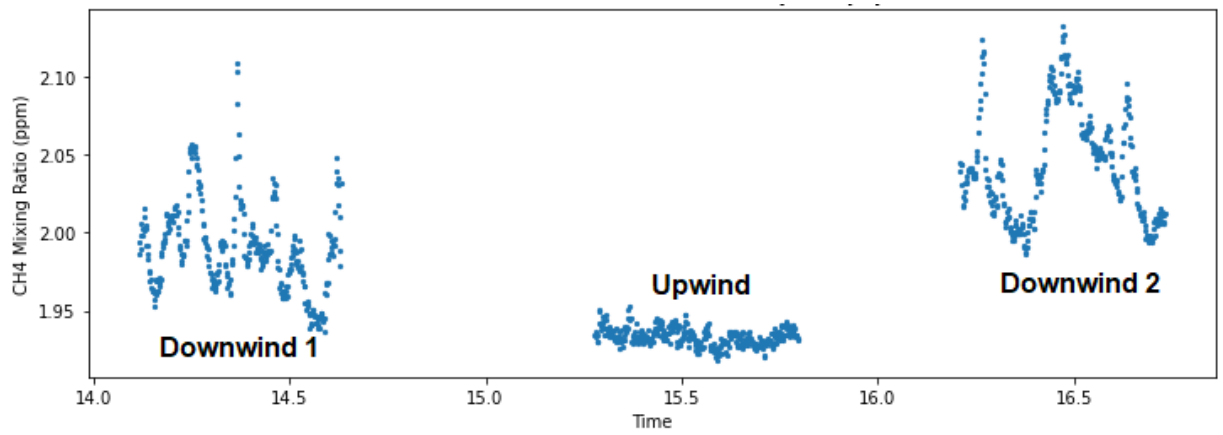

Figure 2.8: Time series plot showing the background (upwind) and methane enhancement observed at the two different downwind locations using TDL spectrometer, on July 12th, 2021.

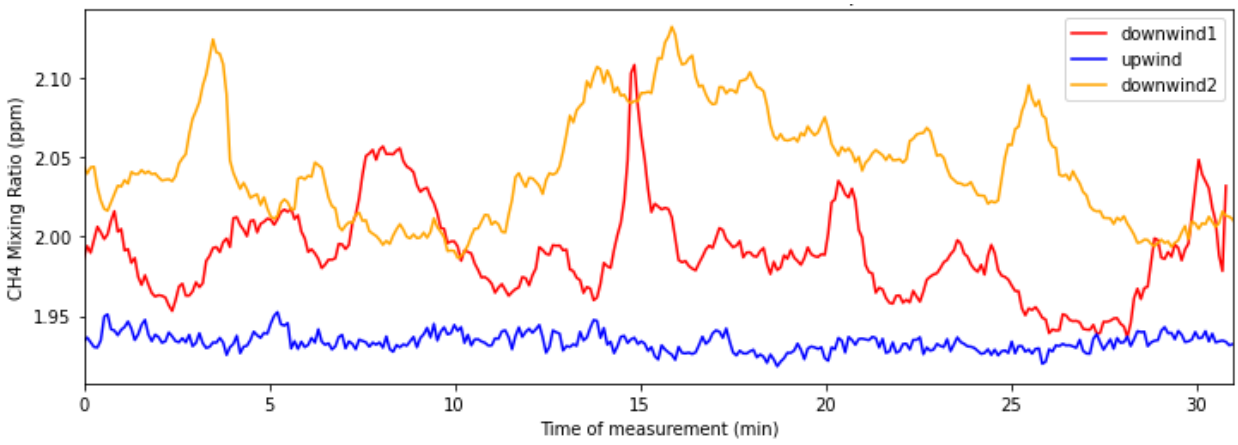

Figure 2.9: Intercomparison plot of methane mixing ratio observed at 3 different measurement sites.

Table 2.2: Methane mixing ratios determined by TDL at each measurement sites.

Site Location	***Measured methane mixing ratio (ppm)***	***Enhancement (ppb)***
Upwind	1.933 ± 0.006	Background
Downwind 1	1.99 ± 0.03	57
Downwind 2	2.04 ± 0.04	111

The back trajectory modelling in figure 2.10 showed that the wind direction had southerly component, blowing from SE. The wind passing through downwind site 2 also passed the bottom left corner of KVL. Back trajectory from downwind site 1 did not directly pass through KVL which agreed with lower enhancement observed compared to site 2.

Figure 2.10: HYSPLIT backward trajectory modelling of methane observed at each measurement site for Oct 12th, 2021. Backward trajectory is generated for plume at height 10 m above ground.

TDL shows relatively good performance in depicting any temporal variability in methane at downwind locations when it is set up to measure methane flux for a period of time. However, it is difficult for the instrument to fully capture methane plume which relies on the maximum pathlength the instrument can be set up at depending on the transect condition. Moreover, it is not capable of showing any enhancement pattern relative to the transect distance as the instrument only reports averaged mixing ratio of methane within its path length. Therefore, a further driving study with the CRDS was necessary to fully characterize and be able to quantify the methane plume from the landfill.

2.3.2. Keele Valley Landfill Mobile Measurements

Figure 2.11 shows a full spatial map of mobile measurement of methane mixing ratios in the city of Vaughan. The measurement period was between 2:15 – 4:00 PM (EST). Measurement started from York University and continued to TransCanada Pipelines and compressor station at Woodbridge. Keele Valley Landfill was surveyed next by driving along the Dufferin St. to the east of the landfill. The wind was blowing from NE direction and was confirmed by the York's EMOS station. The wind condition from the station is summarized in Table 2.3. The methane enhancements from both the compressor station and KVL were captured at downwind locations and depicted on a methane mixing ratio time series plot (Figure 2.12).

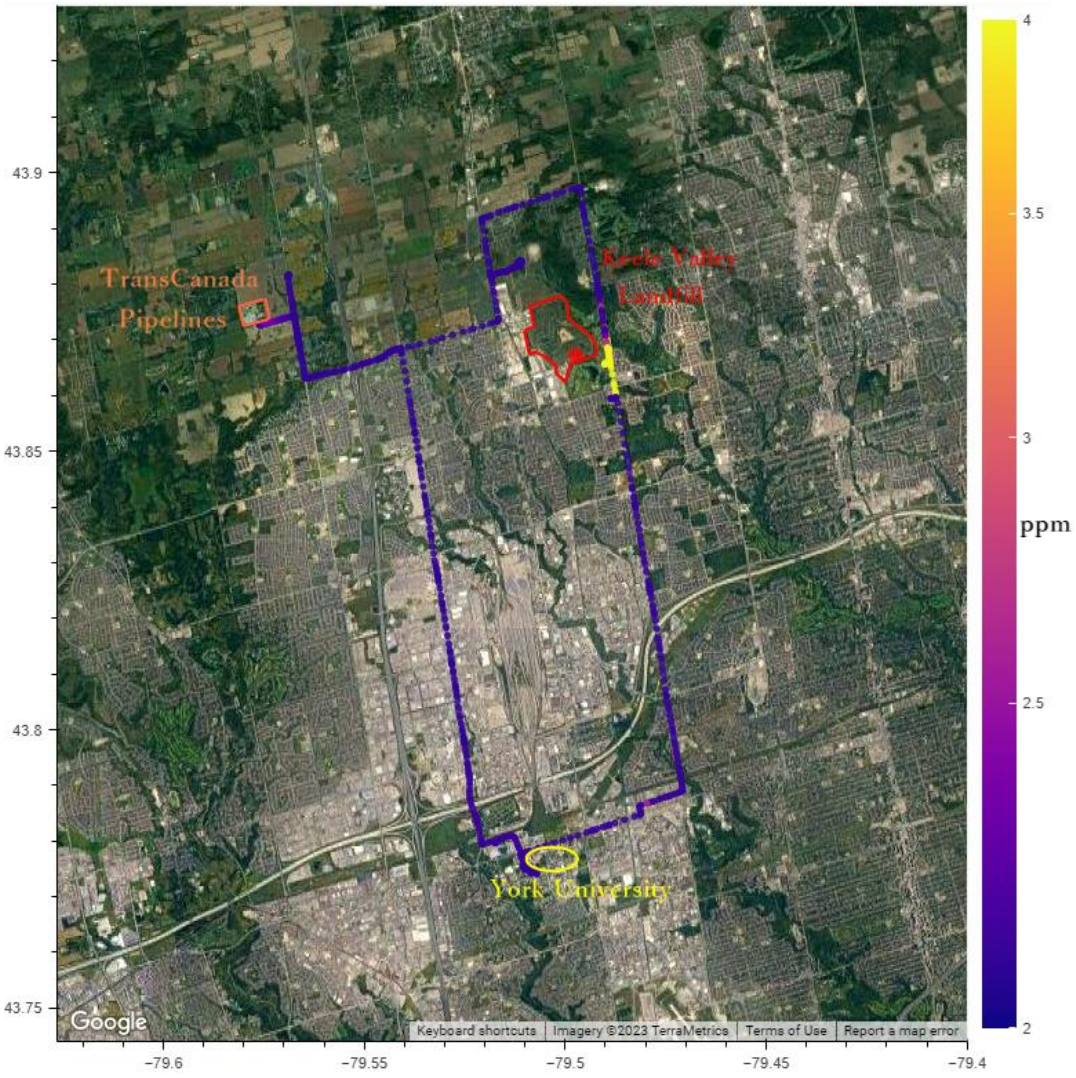

Figure 2.11: Mobile survey of CH_4 from Oct 15, 2021, between 2:15 – 4 PM (EST). Measurements were conducted in Vaughan, ON.

Table 2.3: Meteorological condition from Vaughan station for Oct 13th, 2021.

Time (EST)	***Wind speed (m/s)***	***Wind angle (deg)***	***Temperature (°C)***	***Pressure (kPa)***
2:00 – 3:00	1.4	300	20.2	99.12
3:00 – 4:00	2.2	310	20.7	99.10

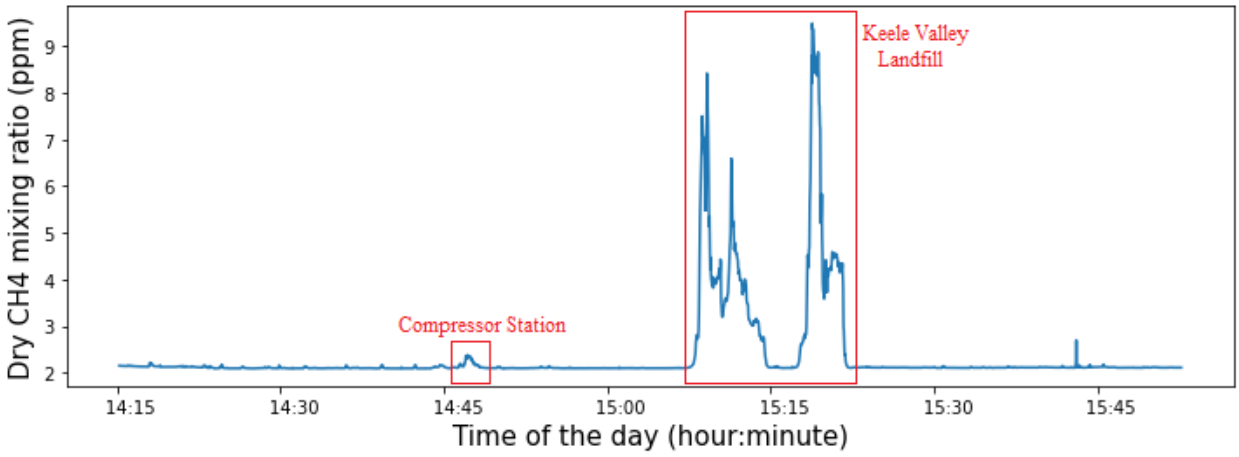

Figure 2.12: Time series plot from driving study on Oct 13th, 2021. The enhancement of methane at compressor station and KVL are highlighted in red box.

Figure 2.13 shows the enhancement pattern of methane mixing ratio observed along the transect located south of the compressor station. Broad peaks with multiple smaller features indicates that the station represents a broad area source with hotspots, potentially including fugitive emissions from gas pipelines.

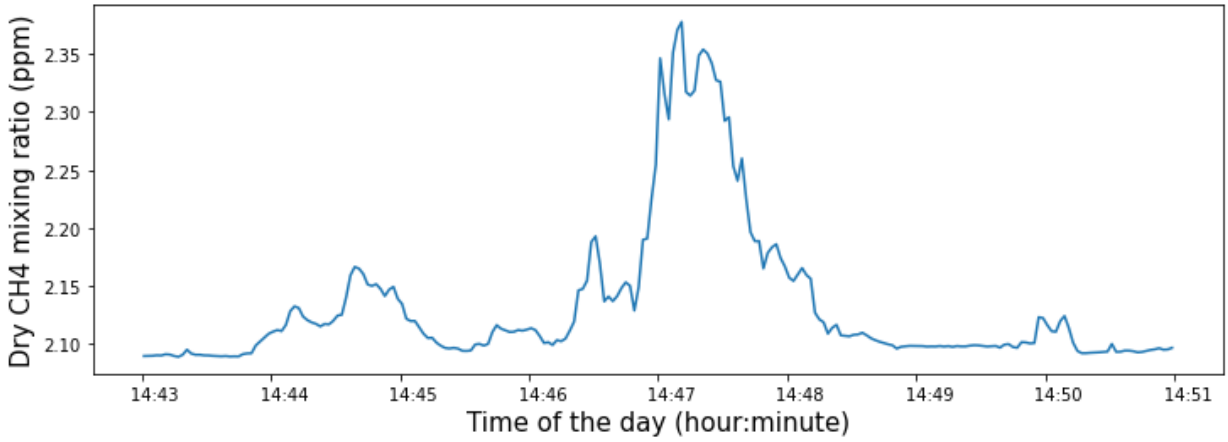

Figure 2.13: Methane measurement performed while driving near the TransCanada pipeline compressor station.

The HYSPLIT back trajectory was generated for the peak observed at the transect to confirm the plume was indeed originating from the compressor station. The back trajectory generated for the plume at 10m height showed the plume was from NE direction and passed through the facility (Figure 2.14). The observed maximum around the station was 2.37 ppm, with the enhancement of 282 ppb.

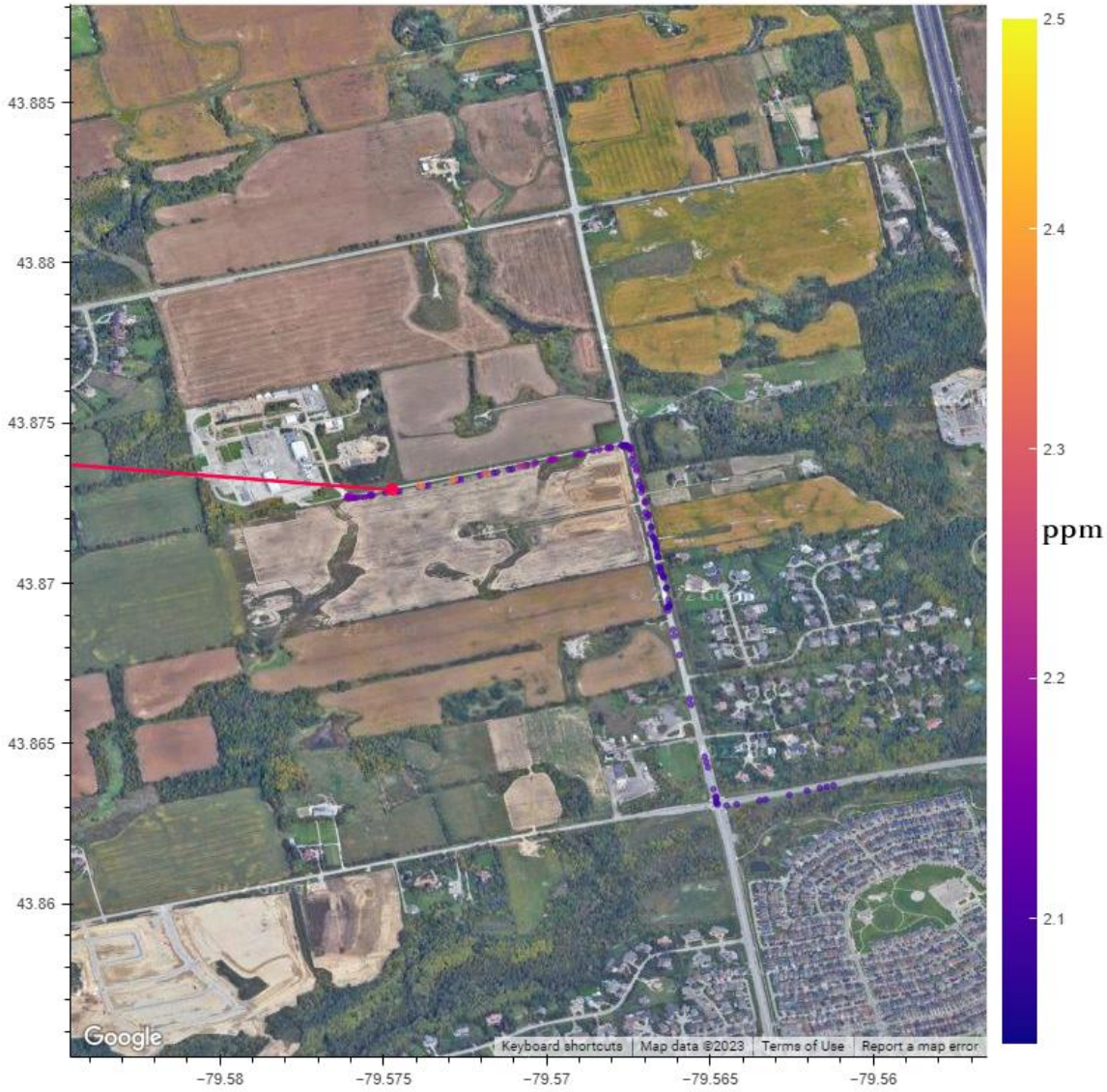

Figure 2.14: Methane map with mixing ratios corresponding to the time series plot in Figure 2.13. Red dot indicates the coordinate at which back trajectory was generated (maximum of the methane peak), and the red line depicts the HYSPLIT back trajectory from the maximum of the peak.

The vehicle travelled along the Dufferin street twice to make two measurements, labelled as travel 1 and 2. Figures 2.15 and 2.17 show the corresponding methane mixing ratio maps for each travel, depicting high enhancement observed to the south of the landfill with enhancements of 6.4 ppm from travel 1 and 7.0 ppm from travel 2. These enhancements were much higher than the result of the July 14th study with the TDL. This was most likely due to the instrument location not being able to fully capture the methane plume. The instrument was required to be set up an exact downwind location of the major hotspot of the landfill aligning to the wind direction. This was difficult on July study without the information of local wind direction and location of potential hotspot on KVL. Both travel 1 and travel 2 of the survey depict strong methane enhancements from the southern region of the landfill. There exists a power generating station located just below the landfill site, where the collected methane gas through collection pipes is used to produce electrical power. During the measurement, visually, heat shimmer was observed from the stack, which implied that even though landfill site was shutdown, their gas collection system and power generation with flaring stacks were still in use. Figures 2.16 and 2.18 represent the methane mixing ratios against the travelled distance which show that the width of each enhancement corresponded to 1911 m and 1983 m respectively. Compared to 56 m distance set up between the retroreflector and the TDL spectrometer, the study also confirmed TDL instrument was not suitable for measuring the broad methane emissions from large landfills such as KVL. The path of methane plume could have also deviated from its initial path by a change in wind direction during measurement. The TDL has limitation as the instrument set up is immobile and only multiple measurements can be made at more downwind locations to account for potentially shifting wind direction.

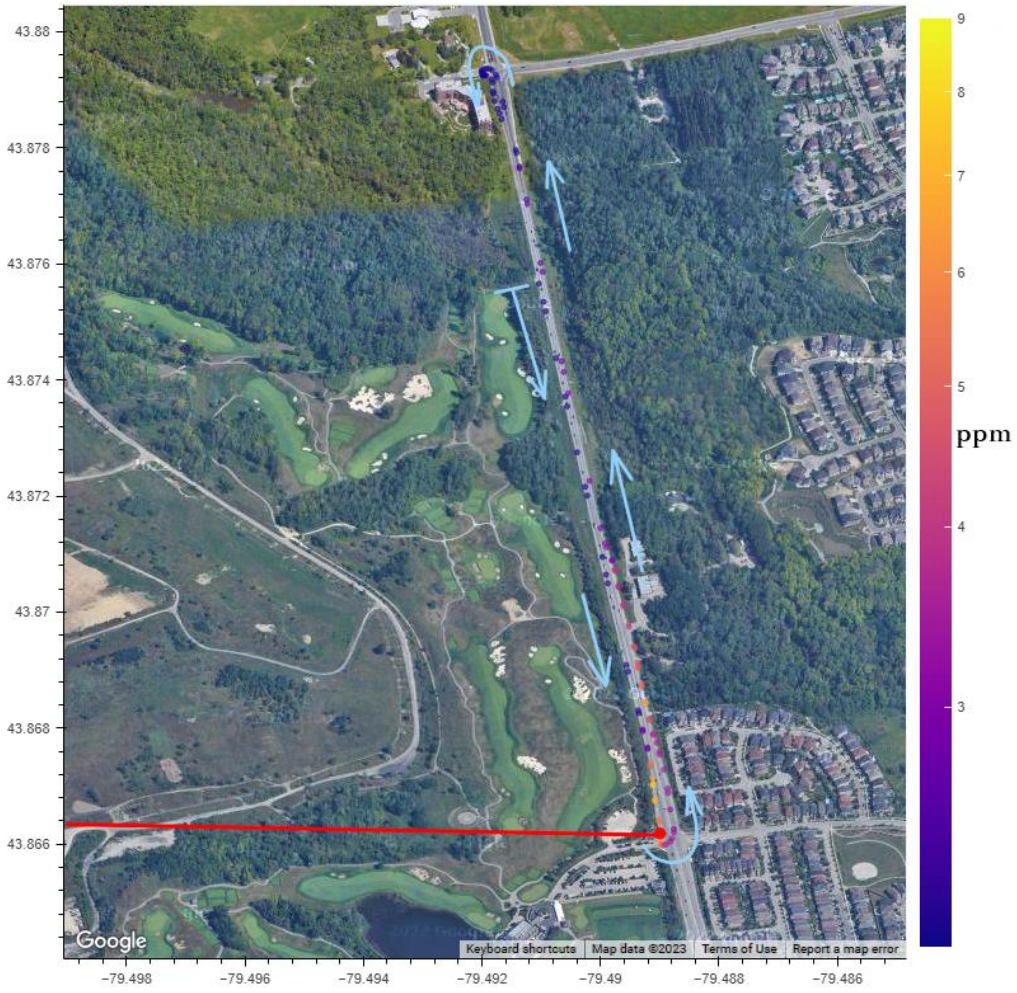

Figure 2.15: Part 1 (15:07 – 15:16 EST) of methane map of mixing ratio to the east of KVL. Light blue arrows indicate the direction of travel. Red dot and line indicate the HYSPLIT back trajectory from the location of maximum.

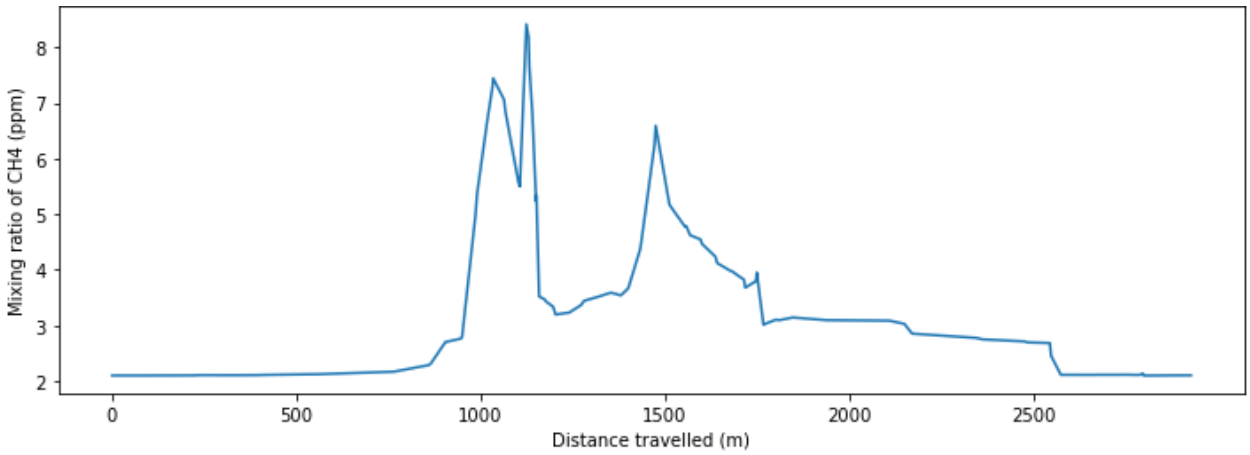

Figure 2.16: Methane mixing ratios plotted against the distance travelled for the concentration map 2.14.

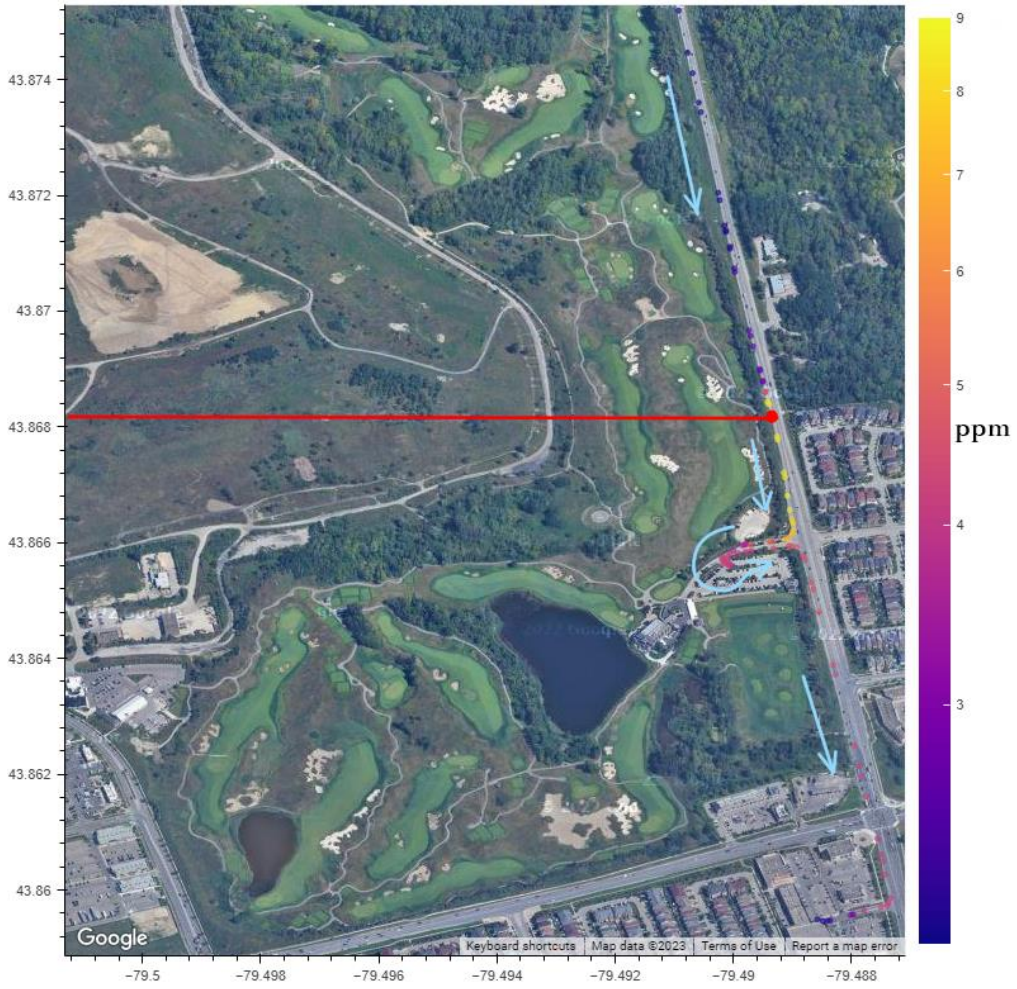

Figure 2.17: Part 2 (15:17 – 15:22 EST) of methane concentration map near KVL. Light blue arrows indicate the direction of travel. Red dot and line indicate the HYSPLIT back trajectory from the location of maximum.

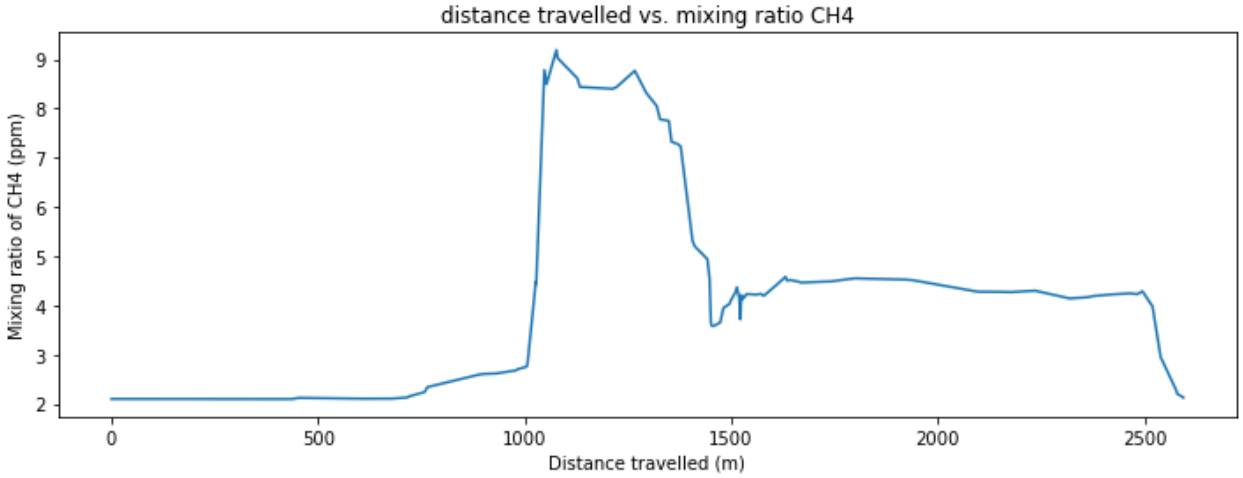

Figure 2.18: Methane mixing ratios plotted against the distance travelled for the concentration map 2.16.

2.3.3. Comparison of inventory value to Landfill Gas Emission Model

The landfill gas emission model (LandGEM) estimates the total landfill gas generated at the landfill, including methane, CO_2, and other minor air pollutants. The model can either employ site specific data or inventory default parameters which are based on the emissions factors that are employed to build the U.S. EPA emissions inventories. Keele Valley Landfill operated between 1983 and 2002 in which the landfill had a total of 28 million tonnes of waste deposited over 19 years or 1.47×10^6 tonnes of waste per year. Methane content was assumed to be 50% by volume in total landfill gas. The methane generation rate constant, k, depends on the landfill moisture, pH, and temperature of the waste mass. Conventional inventory considers k to be 0.04 $year^{-1}$, and 0.02 $year^{-1}$ for arid area. 0.7 $year^{-1}$ is considered for an extreme wet condition such as bioreactor landfill where liquids are added to the landfill soil for fast breakdown of organic matters. A Clean Air Act (CAA) value of k = 0.05 $year^{-1}$ is the U.S. regulatory parameters serving as an emission standard for municipal landfills. The potential methane generation capacity, L_0, depends on the type and composition such as cellulose content of waste deposited in the landfill. Based on the multiple possible default parameters, Figure 2.19 shows the methane generation over time for the KVL up to year 2050. The methane generation is shown to peak 1

year after the landfill closure, in 2003 then continues to decline. It should be noted that due to the limitation on input data such as waste quantities per year and other conventional parameters used, the result is not an adequate representation of the actual Keele Valley Landfill site and should be considered as a rough estimate.

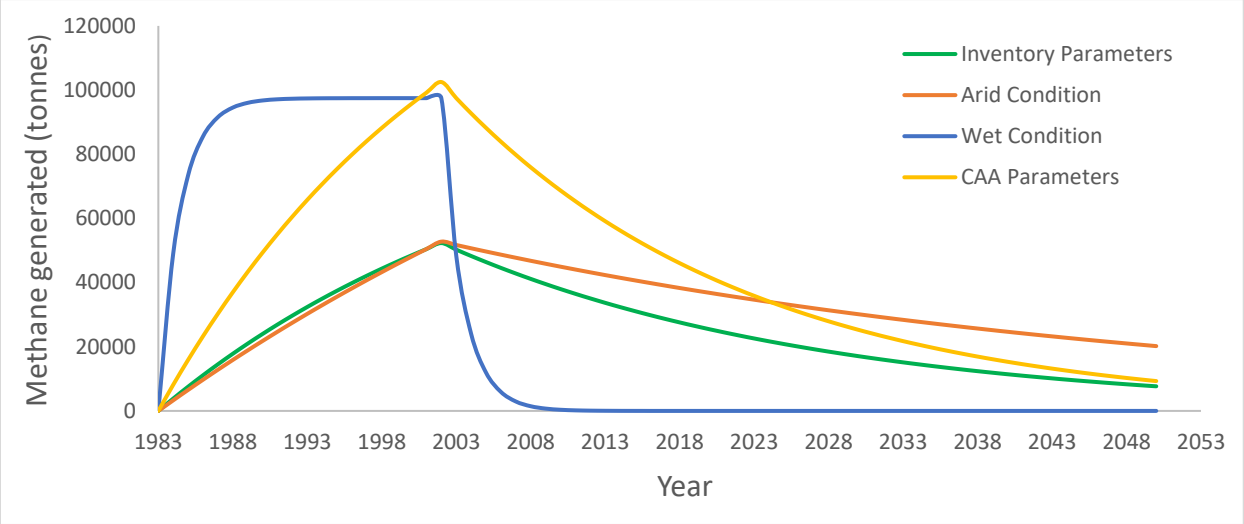

Figure 2.19: Methane emissions calculated by U.S. EPA Landfill Gas Emission Model (Land GEM) with 4 different parameters, plotted up to year 2050.

The methane generation is calculated to be ranging between 24.5 to 39.6 kt in 2021 depending on the input conditions, excluding wet bioreactor type. The summary of the estimated methane generation rate is presented on table 2.4. Since the model only calculates the methane generation rate, losses of methane by LFG collections and oxidations by methanotrophs should be considered. Landfill gas mass balance was previously introduced in Figure 2.1 and can be written as:

$$Net\ CH_4\ emission = (G_{CH4} - R)(1 - OX) \qquad (2.6)$$

From the total methane generated, G_{CH4}, the net CH_4 emission is only a portion which depend on the oxidation factor, OX, and the quantity of CH_4 recovered, R. Default value of 10% oxidation rate is used to build both the inventory and GHGRP (Bronstein et al., 2012). If no gas is recovered, R = 0, 10% of oxidation would imply loss of 2.45 kt methane if 24.5 kt methane generation rate is used (Inventory default). Emission rate of 22.05 kt is similar to the average KVL landfill inventory values of ~20 kt up to 2018. Actual inventory values are expected to be lower as more methane is recovered, R, by the recovery system.

It is unlikely for the methane generation rate or oxidation rate to change drastically in just 2 years between 2019 and 2020. Therefore, even though exact reason of recent declines in the inventory value is unknown (9.8 kt and 11 kt from ~ 20kt), based on the estimation made above, it is reasonable to conclude that the likely cause is the increase in the amount of gas collected, R, either by employing new gas pipelines and/or flaring system.

Table 2.4: Summary of model input parameters for the LandGEM and calculated methane emission in 2021.

	Methane Generation Rate, k ($year^{-1}$)	Potential Methane Generation Capacity, L_0 (m^3/Mg)	NMOC Concentration (ppmv)	Methane Content (% by volume)	Methane Emissions in year 2021 (kt)
Inventory Conventional Parameters	0.04	100			24.5
CAA Parameters	0.05	170	600	50 %	39.6
Inventory Arid Condition	0.02	100			36.1
Inventory Wet Condition	0.7	96			0.000163

2.4. Conclusion

Preliminary assessments over the performance of the TDL and the Picarro CRDS proved that they can provide robust and accurate reading of methane with fast response time with high precision in the unit of few ppb. TDL was capable of monitoring the change in methane mixing ratio and capture any real time change in methane flux for a defined path length while Picarro CRDS was adequate for mobile study.

However, due to the open path nature of TDL, the instrument had higher variability in its measurement and noise compared to the CRDS. Moreover, there was a limit to how long the path length could be set up depending on the measurement site. Considering the observed methane plume was as broad as ~ 1900 m at KVL, the TDL instrument was shown to be not suitable to perform measurement over large area sources. On the other hand, mobile survey performed on Oct 13th, 2021, with CRDS demonstrated that the method could be used to monitor ambient methane in and around the city. Unlike the measurement performed on TDL on July 2021, the result form the mobile study showed that KVL was still emitting high levels of methane. Observed maximum enhancement of main plume from the southern region of landfill was 6.4 ppm (part 1) and 7.0 ppm (part 2) with a broad plateau of ~ 4 ppm over 1900 m distance. Both the TDL study and the mobile survey imply that methane from landfill is majorly emitted from the southern part of landfill in which the power generation facility and gas collection pipes leading to the facility are likely a fugitive hotspot for methane emission from landfill along with broad methane exuding from landfill site. The landfill gas emission model estimated that the landfill was likely still generating methane by 24.5 kt in year 2021 (from Inventory default parameters). The model estimate was in good agreement to the inventory value up until 2018 when precipitous decline in methane emission were observed, close to 50 % reduction. Based on the simple calculation performed using landfill gas mass balance, it is suspected that the landfill site has updated the gas collection systems to reduce fugitive methane from the landfill site.

Chapter 3 : Quantifying Methane Emissions from Greenlane landfill

3.1. Introduction

As anthropogenic greenhouse gas emissions present as a significant challenge to control the contemporary climate change issue, Canada supports the goal of net-zero global greenhouse gas emissions by 2050 and by 2030, plans to reduce its emission by 40 – 50% below 2005 levels. Landfilling continues to be the most common means for disposal of waste in Canada and the sector is reported to be the 2nd largest source of methane, accounting 27% of total methane emissions based on 2020 national inventory report. However, current policies taken by the federal government over landfill GHG emissions are not expected to achieve significant reduction required to meet 2030 goal (ECCC, 2022). Since there exists a strong correlation between the waste management, and Canada's goal in reaching the climate change mitigation, implementing the right waste management strategies is a key contribution to curbing greenhouse gas emissions. Proper quantification of greenhouse gas emissions will provide the necessary knowledge base and inventory reports for regulatory authorities to assess, modify and establish regulations and laws.

In 2019, 11,986,000 tonnes of Ontario's waste were disposed of in landfills (OWMA Report, 2021). Many of Ontario's largest methane emitters are closed down landfills located in Southern Ontario which have accumulated wastes over decades, including Keele Valley Landfill. Ontario still has 805 active landfills, with over 60% of the province's disposal capacity located in just seven large landfills which significantly contribute to the total methane emission. Greenlane municipal landfill is currently serving as one of the seven largest landfill which accepted 1,100,000 tonnes of waste from the GTA region in 2021 (Figure 3.1).

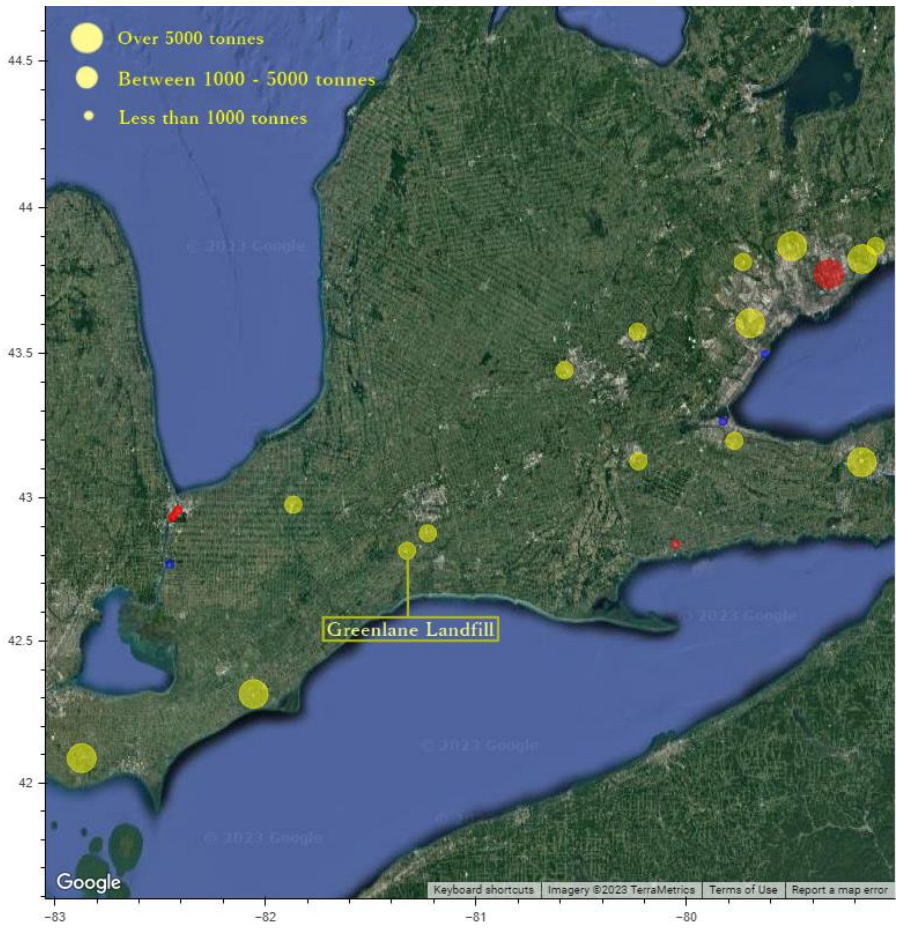

Figure 3.1: Map of major methane sources in southern Ontario based on GHGRP 2020. Yellow circles indicate landfills and waste management sites, red is oil and gas operations and pipelines, and blue represents chemical, steel factories and fossil-fuel electric power generation. Landfill sources include both of currently operating and closed down landfills.

The breakdown of organic waste in landfill from methanogens produce landfill gas (LFG) that is 60-40% CH_4 and 40-60% CO_2 by volume with minor volatile organic compounds (VOC) and trace pollutants (< 1%) (ATSDR, 2001). Landfill gas emission is a complicated process in which the source rate of pollutants can depend on various factors such as type of landfill cover, daily and seasonal variation in weather (pressure, precipitation, and temperature), gas collections systems, as well as soil condition that can affect the anaerobic microbial decomposition and oxidation (Meyer-Dombard et al. 2020, Agdam et al., 2019). Previous studies by Xu et al. (2014) have shown that the surface atmospheric pressure has strong negative correlation with the landfill gas emission which can supress the emission or cause “barometric pumping” phenomenon to emit increased methane at lower surface pressure. For the temperature range between 2 to 25 °C in dry soil condition, increasing surface temperature can potentially lead to a

decrease in landfill gas emission due to bacterial methanotrophic oxidation, creating a methane oxidation barrier on surface. (Su et al., 2014).

Furthermore, landfill gas is often emitted from discrete hotspots rather than diffusive heterogenous emission across the landscape (Röwer et al., 2011, Riddick et al., 2018). This fugitive emission can be due to the preferential gas flow paths from the soil cover and the potential fractures or leaks in the landfill gas extraction pipes. A lot of modern landfills employ methane gas collection and flaring system including Greenlane landfill to produce electricity (WSP Report, 2017). Such leak from the extraction network can potentially account for up to 73% of methane emission from the landfill from just 10% of the surface (Delgado et al., 2022). Therefore, this highlights the importance of understanding the methane hotspot systems from the landfills as large-scale remediation across the whole landfill is not economically desirable. Locally confined hotspot can benefit from local remediation strategies to mitigate the major methane emission. Moreover, methane gas combustion in flares further produces well known ozone precursors such as nitrogen oxides and formaldehyde (Olaguer, 2021).

This chapter focuses on quantifying the emission of anthropogenic methane from Greenlane landfill over 4 different study periods. Greenlane landfill was selected as an appropriate measurement stie as it is a currently the largest active landfill in GTA region which can provide a good comparison to methane emissions characters from the Keele Valley landfill which was a landfill that was closed down 20 years ago. Measurement by the mobile mass balance method is a fast and cost-effective techniques, especially for the quantification over small areas like Greenlane landfill (2 km by 0.5 km rectangular area). The site is also ideal for studying the plume characteristics and emission patterns as there are no other known major methane emitters in the area that can potentially interfere with the measurements other than small agricultural sources and potential vehicle emissions.

The main objectives of the investigation were i) to observe the methane enhancement, and characterize methane plumes to identify the emission pattern as hotspots or diffusive area source ii) to measure the emission rate of methane by the mobile mass balance method and compare the estimated emission rates to the bottom up inventory iii) to observe potential seasonal variability and effects of the meteorological parameters such as temperature, solar insolation, wind speed and pressure on the emission rates and plume characteristics iv) to compare the measured

methane points to the dispersion modelling and assess the effectiveness of the Gaussian dispersion approach to obtain representative methane emission, v) to observe the correlation between methane and carbon dioxide emissions and subsequently to calculate carbon dioxide emission from the landfill.

3.2. Experimental Methods

3.2.1. Study Domain

Site Description and Selection of Measurement days Surveys were conducted for the Greenlane municipal solid waste landfill, Ontario, Canada. To the southeast of the landfill, at a distance of approximately 13km, lies the small city of St. Thomas, while the city of London is situated northeast at a distance of about 20 km. Apart form this, the landfill is located in a rural area that is largely agricultural. Measurement days were selected according to forecast windspeed and direction with wind speed condition of 10 – 20 km/h (2.8 – 5.6 m/s) to achieve homogenous vertical mixing of methane plume at effective distances. Atmospheric condition would ideally be classified as moderately unstable, category B. There is no adequate road system to the west of the landfill for mobile measurements due to the Thames River and the city of London and St. Thomas to the east that can affect the measurement from urban methane emissions. Therefore, wind directions were selected when there was a northerly or southerly component to the wind direction. In total, there were 4 different field studies conducted between October 15th, 2021, and October 1st, 2022, as shown in table 3.1.

Table 3.1: Summary of the field studies performed and the corresponding conditions at the Greenlane landfill.

Field Study	Dates	Wind Direction	Pasquill Stability Classes
A	October 15th 2021	NE – E – SE (Shifting from N to S)	C
B	February 21st 2022	SE to ESE	B - C
C	July 7th 2022	SW to W	A
D	October 1st 2022	NE	B

3.2.2. Instrumentation

The measurement of real-time atmospheric methane was performed employing a G2401 Picarro Cavity Ringdown Spectrometer (CRDS) which was mounted in a car. The instrument simultaneously measured mole fractions of CH_4, CO_2, CO, and H_2O. Water-corrected dry mole fraction of CH_4 was used in the study. The reported precision of the Picarro was 1 ppb (CH_4), 50 ppb (CO_2), and 15 ppb (CO) over the 2 seconds integration period.

The inlet was mounted approximately 1 m above the ground onto the sideview mirror of the Tesla vehicle. The length of the inlet tube caused temporal offsets between the sampling and measurement times. Therefore, for each study, the offset was measured by introducing sample air of enhanced mixing ratios into the inlet and measuring the response time of the instrument. This was repeated three times and the average delay time (10 – 12 seconds) was used to correct GPS-location and mixing ratio data for each study. The response time of the instrument is separately estimated to be 2 – 3 seconds. The average driving speed of the vehicle was typically 40-60 kmh^{-1} during the measurement. Due to the nature of the GPS software, the recorded GPS did not have consistent spacing between the recorded coordinates. Therefore, Picarro data was synced to the recorded GPS coordinates and the corresponding spatial resolution varied between 2 to 130 m after sync with an average of 48 m.

3.2.3. Assessment of Meteorological Parameters

Since the velocity field of the wind dictates the dispersion of methane, quantification of landfill gas emission requires measurement of meteorological parameters such as prevailing wind speed, direction, temperature, and pressure. For all field studies, wind, pressure, and temperature data were obtained from the government of Canada historical weather data, which was measured at the London international airport, located approximately 26 km far from the landfill. Since these parameters were assumed to be steady during the period of measurements, their average values were used along with their corresponding standard errors. For field study C and D, a meteorological tower was deployed and set up at a downwind transect location close to the source to be compared and averaged to the station data.

The height of the planetary boundary layer was estimated from several sources. First, the National Center for Environmental Prediction (NCEP) North American Regional Reanalysis (NARR) was used as a model estimate of boundary layer height. Reanalysis products are forecasts that are corrected based on the surface and upper-air observations (Lee et al., 2016). NARR assimilates boundary conditions from the NCEP Eta Model, and surface and rawinsonde observations with 3 h temporal intervals. The uncertainty in the height of planetary boundary layer is proposed to be approximately ± 40% based on NCEP products-sounding data comparison result from study by Guo et al (2016). Additional boundary layer height data was obtained by the ceilometer at Windsor (Vaisala CL51 ceilometer). The ceilometer employed pulsed diode lidar on single lens optics to measure the cloud base height. Using the experimental algorithm developed by ECCC using a 1D gaussian filter and minimum gradient method, 30-min average of PBL heights were computed and averaged. Aircraft Meteorological Data Relay (AMDAR) data was also employed if there was an aircraft that was flown during the measurement period near London. AMDAR can provide vertical profile of temperature and wind data with meteorological sensors equipped on the aircraft which can be used to locate inversions to identify the height of the boundary layer.

For the calculation of kinematic heat flux, the amount of downwelling shortwave radiation was obtained by the Advanced Baseline Imager (ABI) level 2 product of GOES satellite. Surface shortwave radiation data was generated per hour and average of them was used for the study.

3.2.4. Detection of Methane Enhancement

The enhancement of methane above background levels is proportional to the emission rate of the source. As the plume becomes harder to identify as the shape broadens in transects further away from the source, it is necessary for a statistical method of identifying the location of the maximum (center of the plume), and lateral deviation.

A gaussian curve fitting algorithm was developed to identify the location of the plume and the background in which the algorithm locates plume centerline and perform gaussian curve fitting to the measured data points. From the fitted data, data points within the region of ± 3σ (99.7% of data points) were considered to be the plume points while data outside of the curve were considered to be the background points. Data points within the plume's curve fit were

numerically integrated by the Simpson's method along the path of lateral y-distance to obtain the integrated crosswind concentration in g/m^2.

3.3. Results and Discussion

3.3.1. Study A on October 15th, 2021

The field measurement performed on October 15th, 2021, included measurements made between 10:17 AM to 12:44 PM. The purpose was to make preliminary measurement of methane enhancements around the Greenlane landfill. Figure 3.2 depicts the full driving map of methane mixing ratio from the city of London to the roads that encloses the landfill as well as farther downwind transects.

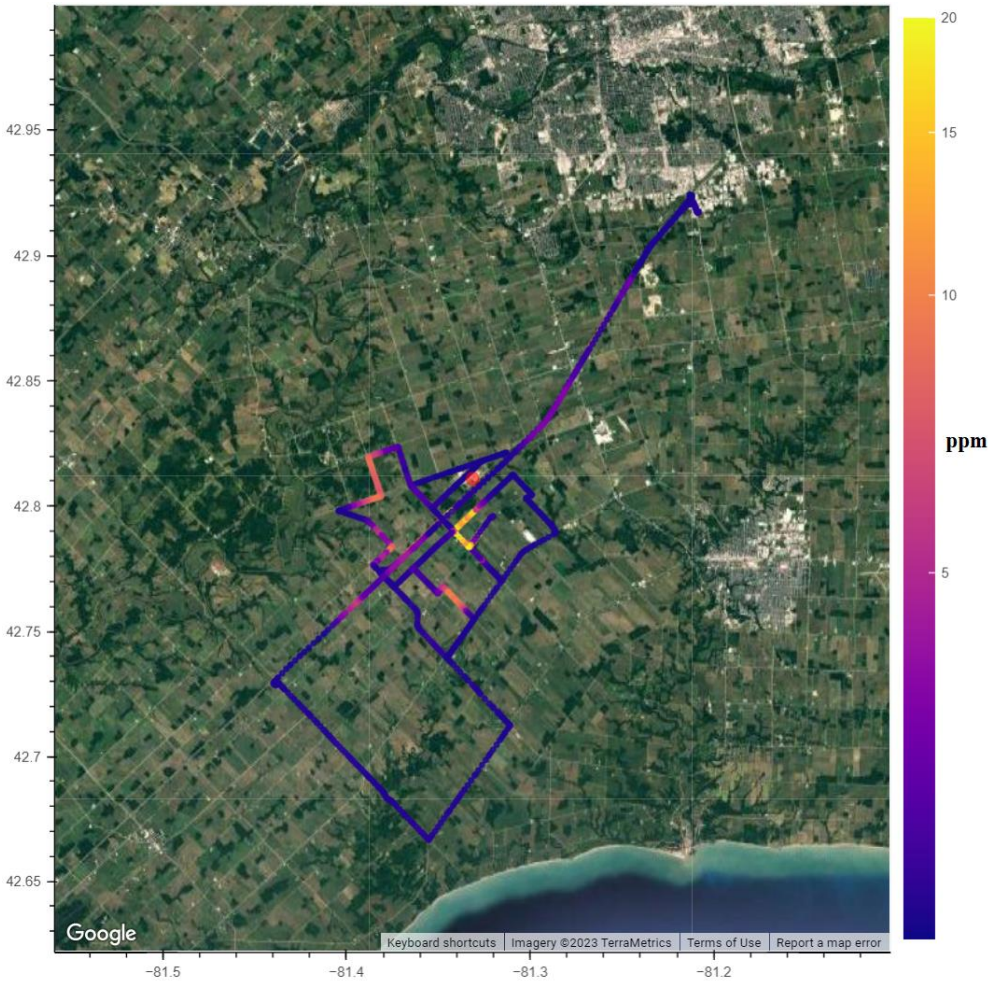

Figure 3.2: Concentration map of methane for the survey on Oct 15th, 2021, driving between London and Greenlane landfill during study A with red dot indicating the location of the Greenlane landfill.

Figure 3.3 shows a times series plot of observed methane for the study. From multiple plumes observed during the measurement, they can be classified into two types. Narrow plumes, which are close to the source, indicate the presence of a local point source (hot spot) while wider plumes with more complex shape indicated more diffusive and distant source. It should be noted that a large observed methane enhancement does not necessarily correlate to a large methane source as the observed enhancement depends on the distance from the source as well as the atmospheric conditions during the survey. For example, less vigorous vertical mixing due to lack of solar insolation during winter can cause ground level emission to stratify near the surface. Therefore, even when the emissions are consistent over time, the mixing ratio enhancement for that specific study can be higher than other times.

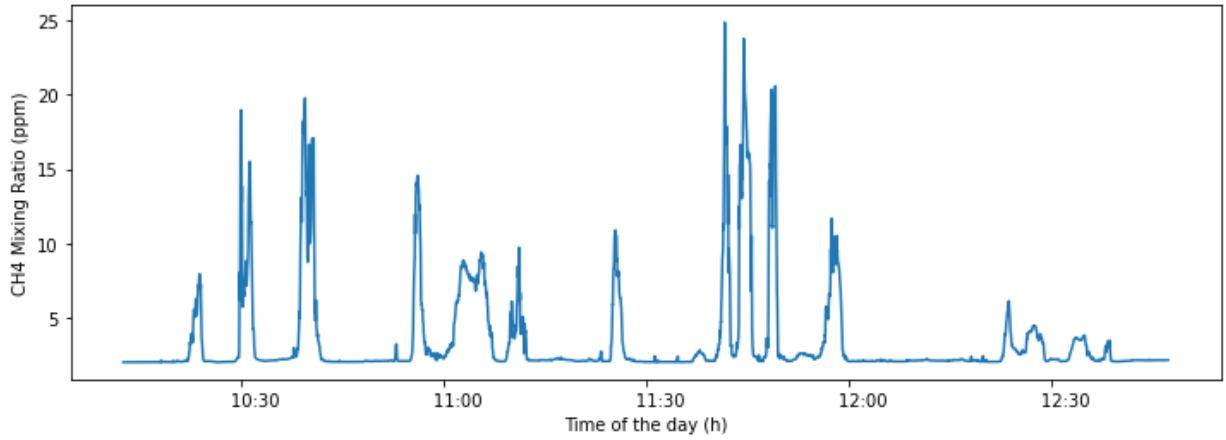

Figure 3.3: Time series plot of dry CH_4 mixing ratio during study A, with the measurement starting from the city of London at 10:17 AM, travelling to Greenlane landfill and back to the London at 12:44 PM.

The wind data obtained from the London international airport showed discrepancies with the actual observed wind direction during the measurements. The wind direction was observed to be NE to NNE on site which shifted to SSE by the end of measurement period. However, station recorded data showed the wind speed to be from E – SE (Table 3.2).

Table 3.2: Summary of key meteorological parameters for study A.

Time (EST)	*Wind speed from station (m/s)*	*Wind direction from station (deg)*	*Wind Direction Observed*	*Pressure (kPa)*	*Temperature (K)*
10:00 – 11:00	2.5	120 (ESE)	NE - NNE	98.02	288.25
11:00 – 12:00	1.1	100 (E)	NE - SE	98.01	289.35
12:00 – 13:00	0.8	140 (SE)	SSE	97.88	289.55
Average	1.5 ± 0.7	120 ± 20		97.97 ± 0.06	289.1 ± 0.6

The forward HYSPLIT trajectory model (Figure 3.4) shows shifting wind direction from NW in the morning at 9 – 10 AM which shifted to S (11PM) then SE wind by 12 PM. Locally, it was also observed that the wind direction was shifting much faster than the hourly direction change depicted by the HYSPLIT. Due to the inconsistent wind directions, especially for early morning trajectories, HYSPLIT backtrajectories could not be used to estimate the movement of the plume. As it can also be seen from the 9 AM trajectory (red), drastic shifts in wind direction could have caused locally circulating plume around the landfill.

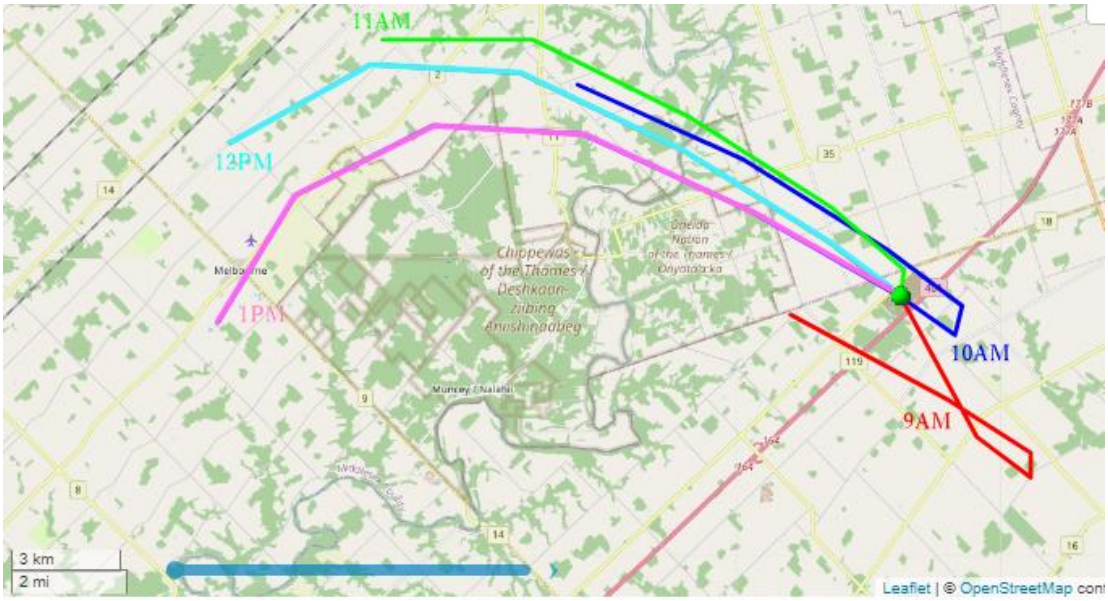

Figure 3.4: Forward HYSPIT Trajectory Modelling from the landfill, starting from 13 UTC (9 AM EST) represented by red line. New path is created every hour up to 17 UTC (1 PM EST) to visualize the shifting wind direction: Red = 9 AM, Blue = 10 AM, Green = 11 AM, Light blue = 12 PM, Pink = 13 PM, indicate the starting time of each trajectory with 5 hourly data points.

There are other potential methane sources nearby to the city of London and St. Thomas, which are located east of the landfill, including farms and multiple waste management sites (Waste Connections Canada, Proactive Waste Inc., etc.). The preliminary measurement along highway 401 confirmed a strong influence from the city of London landfill which is depicted as a blue dot in Figure 3.5. The observed enhancement is 5.90 ppm above background at 10:23 AM. The plume is assumed to be transported by the NE wind during measurement which coincides with the location of the landfill, NE to the highway 401. The width of this plume is broad, 2970 m at a distance approximately 3.5 km away from the landfill site.

The enhancement observed to the south of the landfills shows much higher enhancements, with maximum values of 18.96 ppm and 19.25 ppm for each peak, corresponding to enhancements of 16.89 ppm and 17.18 ppm respectively. This observed enhancement could be the plume that was directly transported from the landfill by the N – NE or the plume that could have been circulating around the landfill.

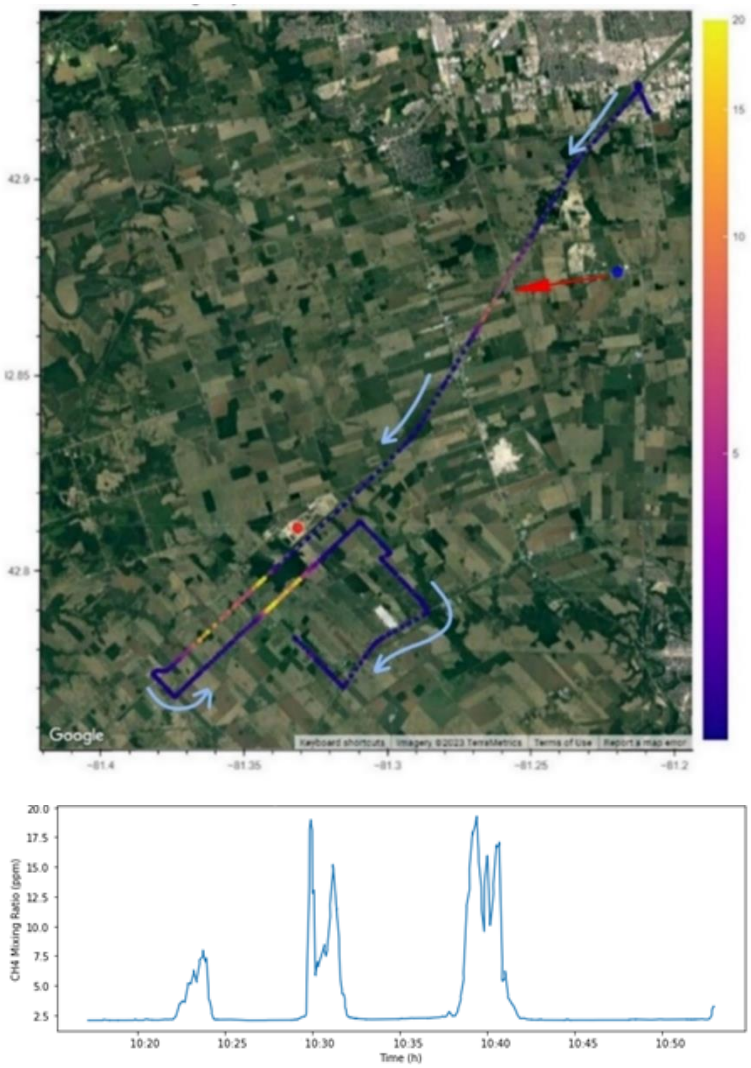

Figure 3.5: Part 1 of survey from London to Greenlane landfill between 10:17 AM - 10:53 AM (EDT) (Top) with corresponding time series plot of mixing ratio (Bottom). Red dot indicates the location of potential hotspot at the Greenlane landfill. Blue dot shows the location of city of London landfill site. Light blue arrow indicates the direction of travel.

Figure 3.6 shows the measurement made from 10:53 AM to 11:18 AM. NE wind carried the plume to the SW of the landfill, depicting 3 different types of plume. Enhancement 0, closest to the landfill shows a relatively clean guassian shape which implies methane source from landfill is likely a single hotspot. The enhancement above background corresponded to 12.5 ppm. The Gaussian dispersion estimation is made with following parameters: distance between a potential hotspot location to the peak enhancement: 2 km, average wind speed: 5.3 km/h (= 1.47 m/s), temperature and pressure given on table 3.2, and stability category, C. Stability is assumed based on 266 W/m^2 low downwelling solar radiation and weak wind condition that most likely formed

neutral boundary layer during measurement period. The calculation results in the source rate of 862 g/s, equivalent to 3103 kg/h.

Plume 1 and 2 are the plumes from two different time frames. Plume 2 is likely a newer plume that is carried by NE wind which aligns with plume 0. Enhancement pattern shows multiple smaller peaks within its broad enhancement region which can imply presence of smaller nearby sources. However, considering the distance to the landfill is only 5 km with no other known sources in between, it is possible that the drastically changing wind and the topography could have caused such features in the peak.

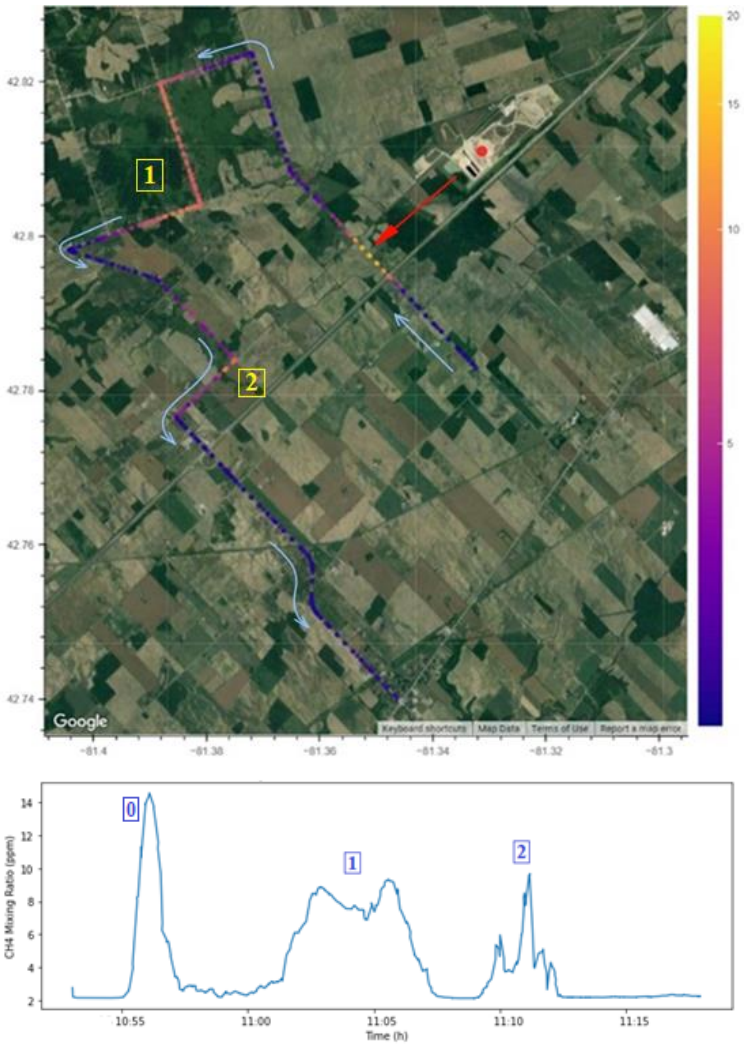

Figure 3.6: Part 2 of survey between 10:53 AM - 11:18 AM (EDT) (Top) with corresponding time series plot of mixing ratio (Bottom). 3 different types of plumes depicted by the CRDS are labelled.

Due to changing wind conditions and discrepancy with the station data, measurement surrounding the landfill was made to ensure there was no south wind carrying the plume. Driving back to the landfill and the transect just above it confirmed there was still NE wind carrying the plume to the south of the landfill at 11:26 PM (Figure 3.7). Clean and sharp enhancement feature observed during this time period implies direct methane plume from the landfill. The peak has enhancement of 8.72 ppm. Using the same parameters for the gaussian, with new downwind distance of 2.5 km, the estimation of source rate yields 900 g/s, or 3240 kg/h close to what is calculated from part 2 of the survey (Figure 3.6).

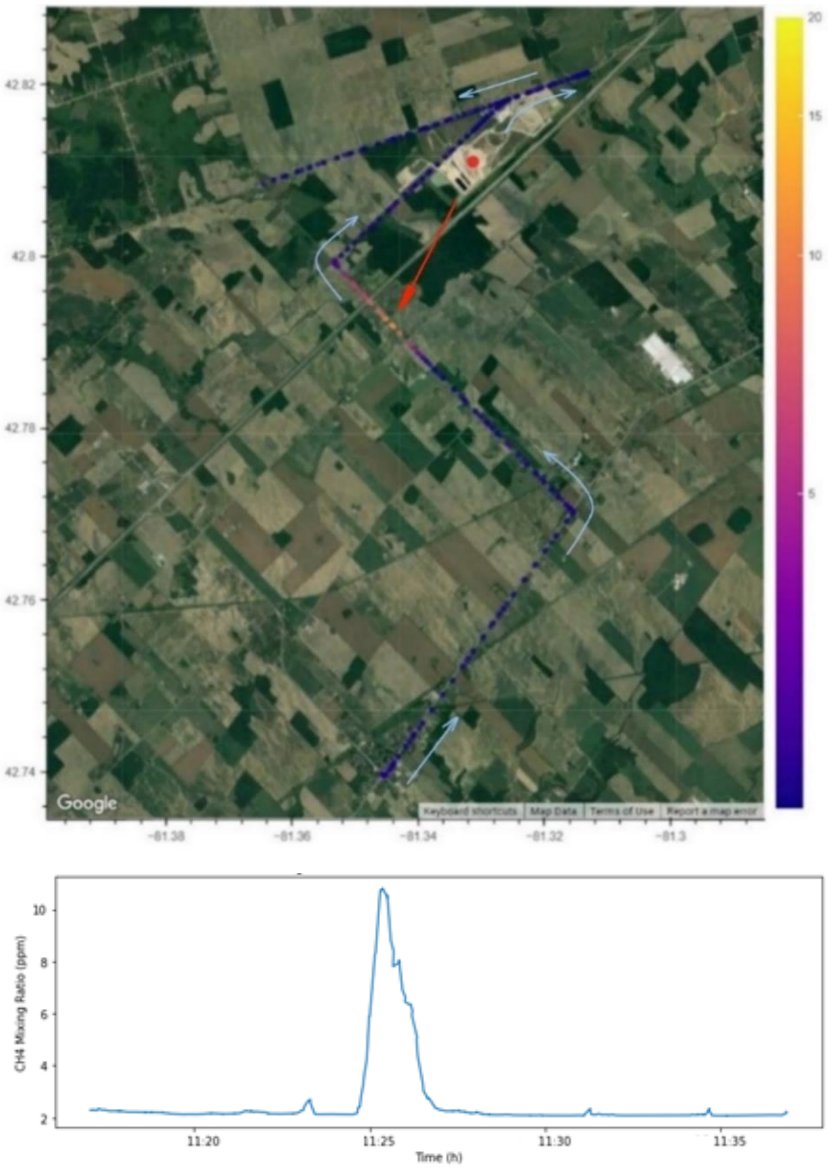

Figure 3.7: Part 3 of survey between 11:17 AM - 11:37 AM (EDT) (Top) with corresponding time series plot of mixing ratio (Bottom).

Between 11:40 to 11:50 AM, multiple large enhancements were observed at location 1 with maximum enhancement up to 21.6 ppm (Figure 3.8). It is reasonable to hypothesize that the three peaks at location 1 are all from Greenlane landfill since they show similarity in shape and maximum enhancement. However, most likely they are from different time frames, affected by rapidly shifting wind direction.

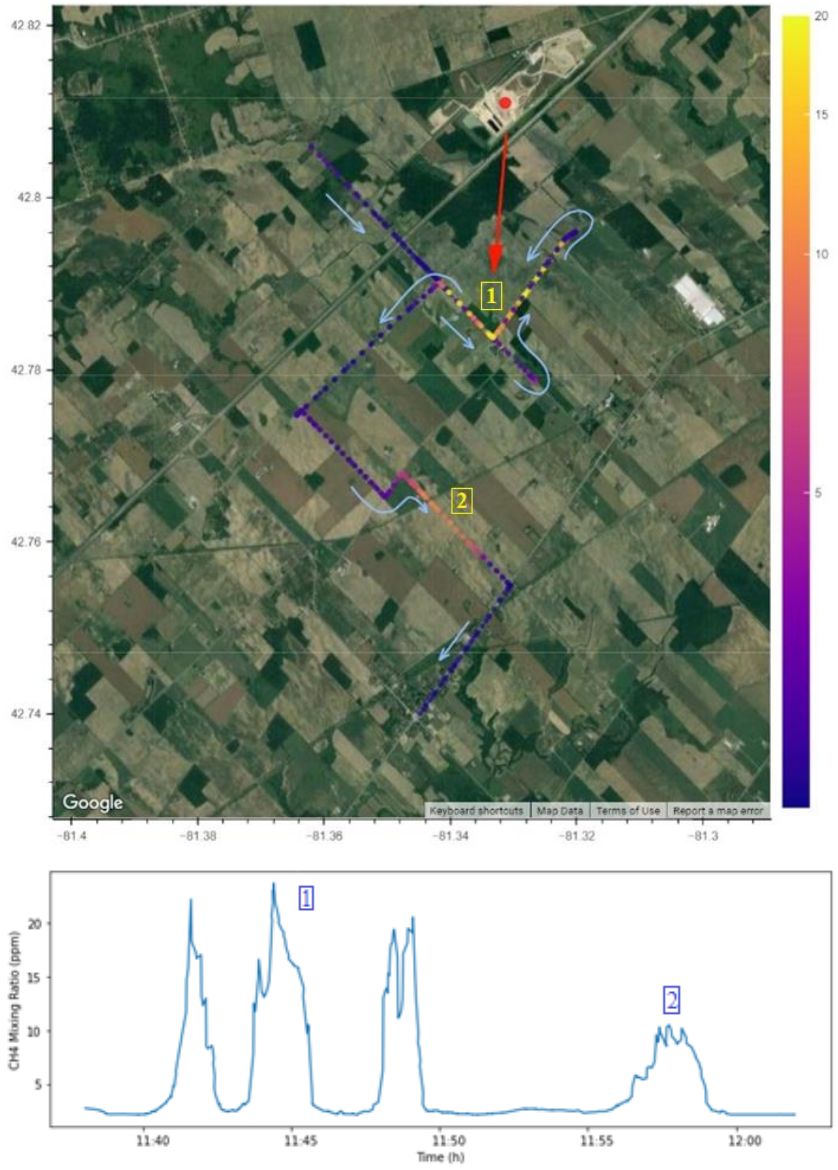

Figure 3.8: Part 4 of survey between 11:38 AM - 12:02 PM (EDT) (Top) with corresponding time series plot of mixing ratio (Bottom).

As expected from shifting wind directions that would have been carrying the plume in multiple direction at different times, the farthest measured transect shows multiple broad enhancements. At 16 km distance away from the landfill, the maximum mixing ratio of methane is observed to be 2.25 ppm which corresponds to 0.17 ppm enhancement above background (Figure 3.9).

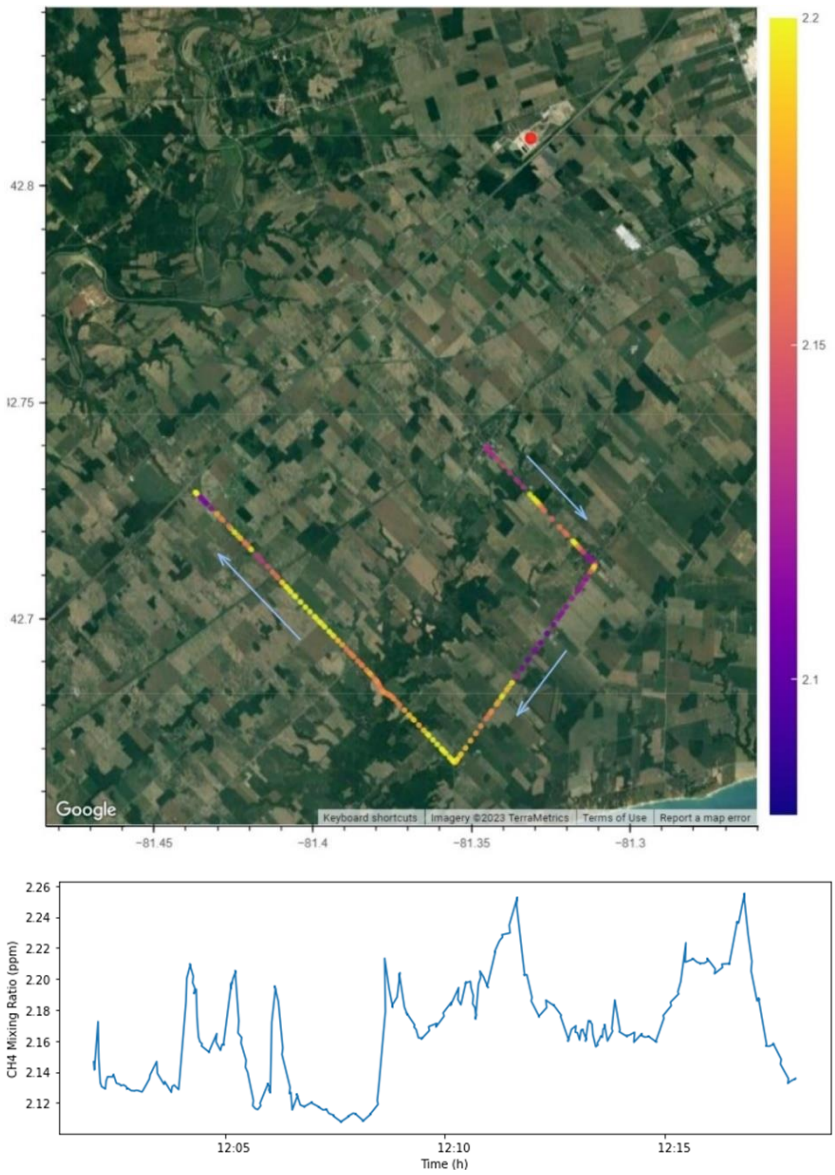

Figure 3.9: Part 5 of survey between 12:02 PM - 12:19 PM (EDT) (Top) with corresponding time series plot of mixing ratio (Bottom).

3.3.2. Study B on February 21st, 2022

A wintertime field measurement, Study B was performed on February 21, 2022, with measurements made between 2 to 4 PM (EST), along transects northwest of the landfill as illustrated in Figure 3.10. The color coding for the map was maximized at 4ppm to allow visualization of smaller enhancements (e.g., 2.58 ppm at T5) further from the source. Closer transects demonstrated high maximum methane mixing ratios of 20 - 24 ppm, with the highest

value observed on T0 of 23.38 ppm. These observations were consistent with the enhancement measured from study A. The driving route was chosen so that the transect was a relatively straight line and perpendicular to SE and ESE wind direction. The differences in angle between the transect and wind direction were accounted for to find the exact perpendicular component of the wind speed for an incoming slant wind direction required for mass balance calculation. The terrain downwind of the landfill was relatively flat without any large buildings or geographical features that could alter the transport of the plume.

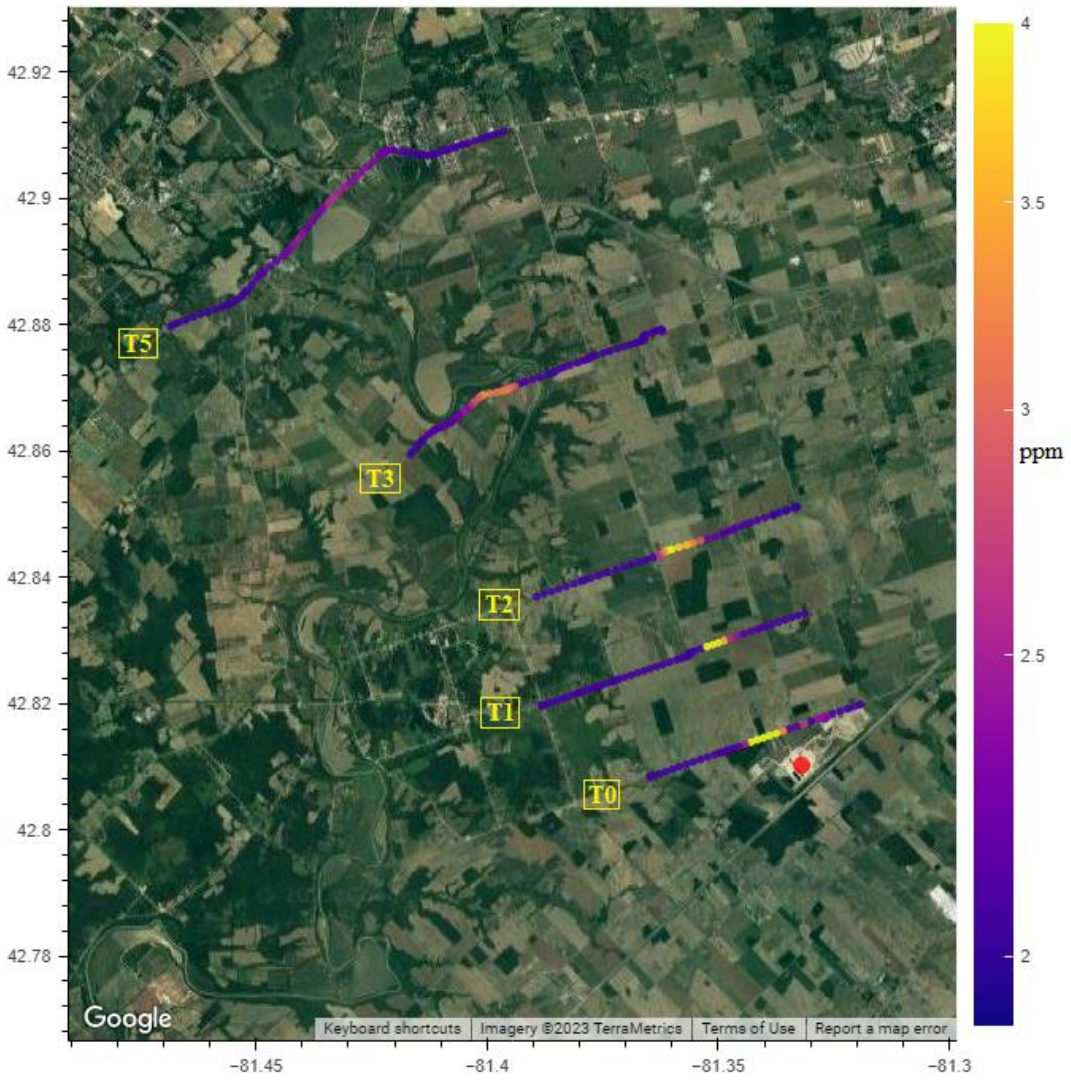

Figure 3.10: Map of color-coded methane mixing ratio along transects during study B, between 2 to 4 pm (EST) on 21 Feb 2022. Red dot indicates the location of the center of Greenlane landfill. Wind direction was ESE to SE during most of the measurements.

Table 3.3: Summary of meteorological parameters and averages used in the calculation of mass balance. Uncertainties calculated as standard errors.

Time (EST)	*Wind speed (m/s)*	*Wind direction (deg)*	*Pressure (kPa)*	*Temperature (K)*
14:00	5	100	98.58	278.05
15:00	5.6	130	98.57	279.15
16:00	3.9	130	98.6	278.65
Average	4.8 ± 0.5	120 ± 8	98.58 ± 0.01	278.62 ± 0.26

Figure 3.11 shows methane mixing ratio along each transect with plume enhancement that are roughly gaussian in shape. The plume follows the gaussian distribution very well for T0 (Figure 3.12) and starts to broaden while σ_y and σ_z increase with the plume spreading for farther transects. It is also noted that the shape of the curve becomes irregular as the surface turbulence and obstacles hinder the plume's spread and trajectory.

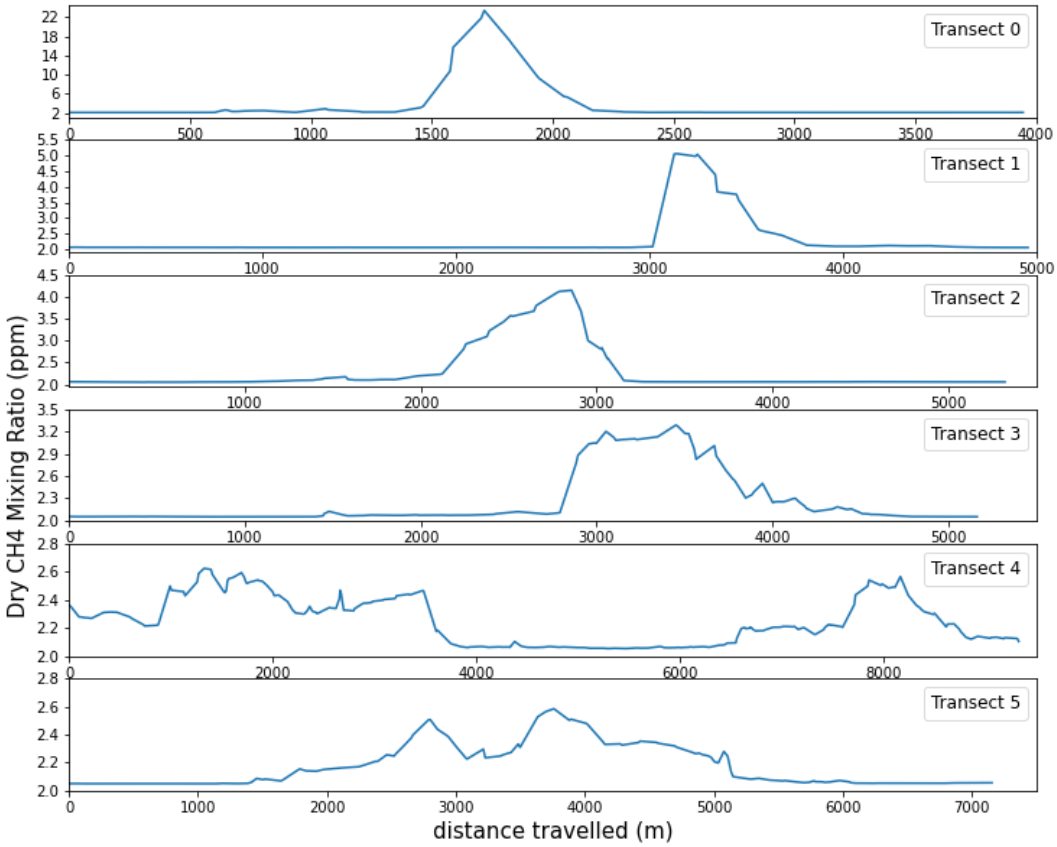

Figure 3.11: CH4 mixing ratios observed per transect plotted against the lateral distance travelled.

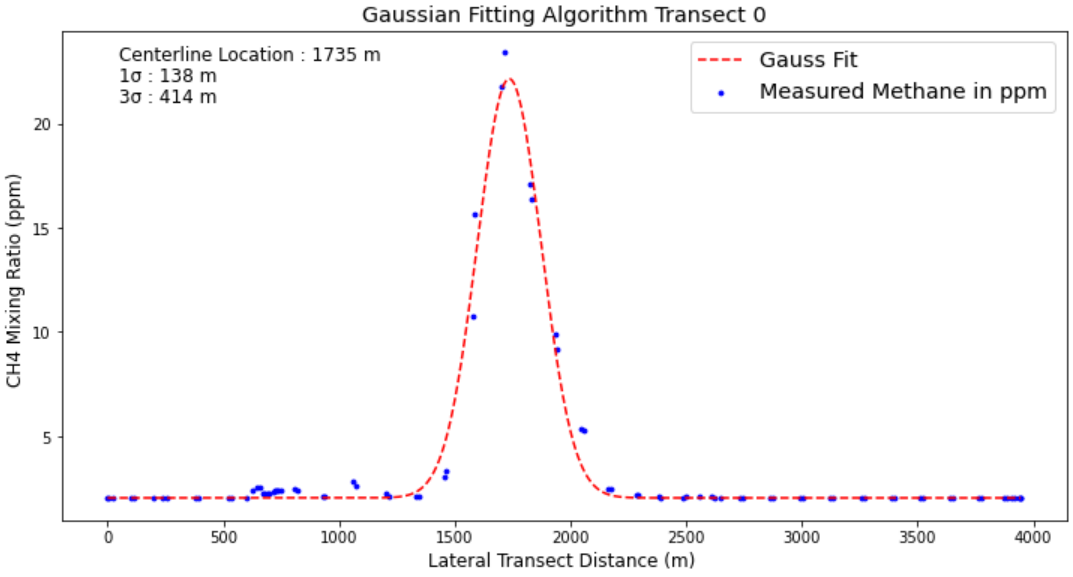

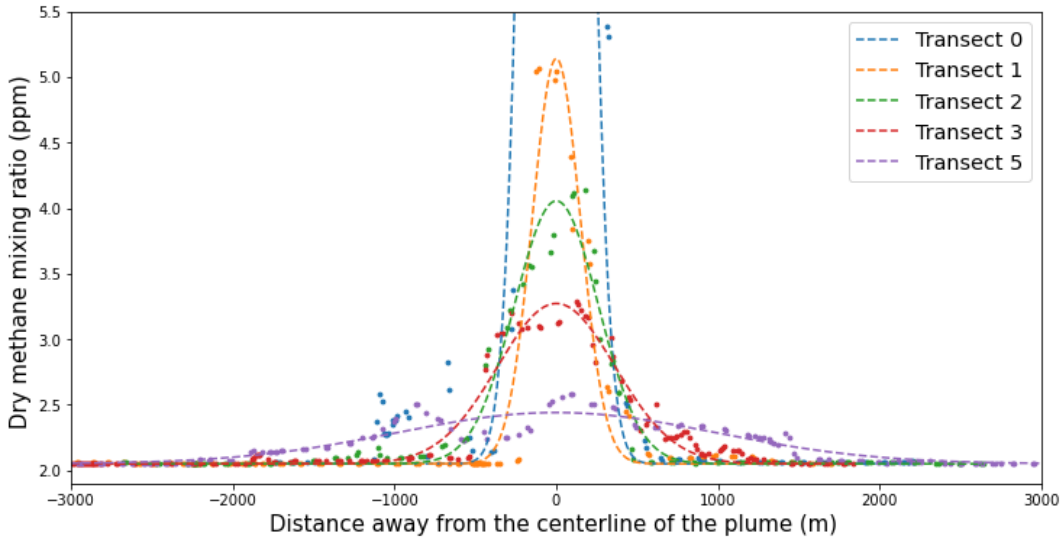

Figure 3.12: Plots of gaussian curve fit of the lateral concentration for transect 0 (top) and a plot of curve fitted enhancements centered at the centerline of the plume.

Background values, X_{CH4_bg} for each transect are calculated from the data points outside of 6σ of the gaussian curve which were subtracted from measured CH_4 to obtain enhancement values.

For the closest transect, T0, source rate was estimated by the gaussian model with the following parameters: 4.8 m/s wind speed, 770 m downwind distance between the peak location and the speculated hotspot location of the landfill, atmospheric stability of C, with the enhancement of 21.28 ppm, the model outputs 888 g/s, which corresponds to 3197 kg/h.

Downwelling shortwave radiation value is obtained from the GOES-16 satellite (DSR – Downward Shortwave Radiation – Surface) which estimates the total amount of shortwave radiation that reaches the Earth's surface. As the CONUS product has a resolution of 0.25 degrees (approximately 27 km), coordinate at 42.875, -81.375 is selected close to the landfill measurement locations as shown in Appendix Figure B.1 with the cell enclosing all transects and the landfill. The averaged DSR value at this location corresponds to 550 ± 40 W/m^2.

Two different planetary boundary layer heights are estimated by NCEP NARR and the ceilometer data from Windsor. The estimated PBL height from the 3-hour averaged NCEP NARR data is 350 ± 150 m. The estimated 3-hour averaged PBL height from the 30 min interval ceilometer data is 485 ± 100 m. The average of those two values is used as 420 ± 100 m. Based on this PBL height, Deardorff velocity is calculated to be 1.746 ms^{-1}. Calculation for the

Deardorff velocity and mixing distance is attached in Appendix B.1 along with the calculation of corresponding uncertainties. Therefore, it is expected for methane to mix to top of the PBL by $t_m = \frac{Z_{PBL}}{w^*} = 241\ s$.

Based on the assumption that plume is well mixed by the time it reaches 3 t_m = 726 s, given the average transport velocity the tracer to be 4.8 ± 0.4 m/s, the mixing distance equals to 3500 m. This distance is depicted as a blue line in Figure 3.13. Three data points beyond this line are presumed to be valid for mass balance estimation, and emission rates can be averaged. The average estimated methane emission rate is 3200 ± 830 kg h^{-1}.

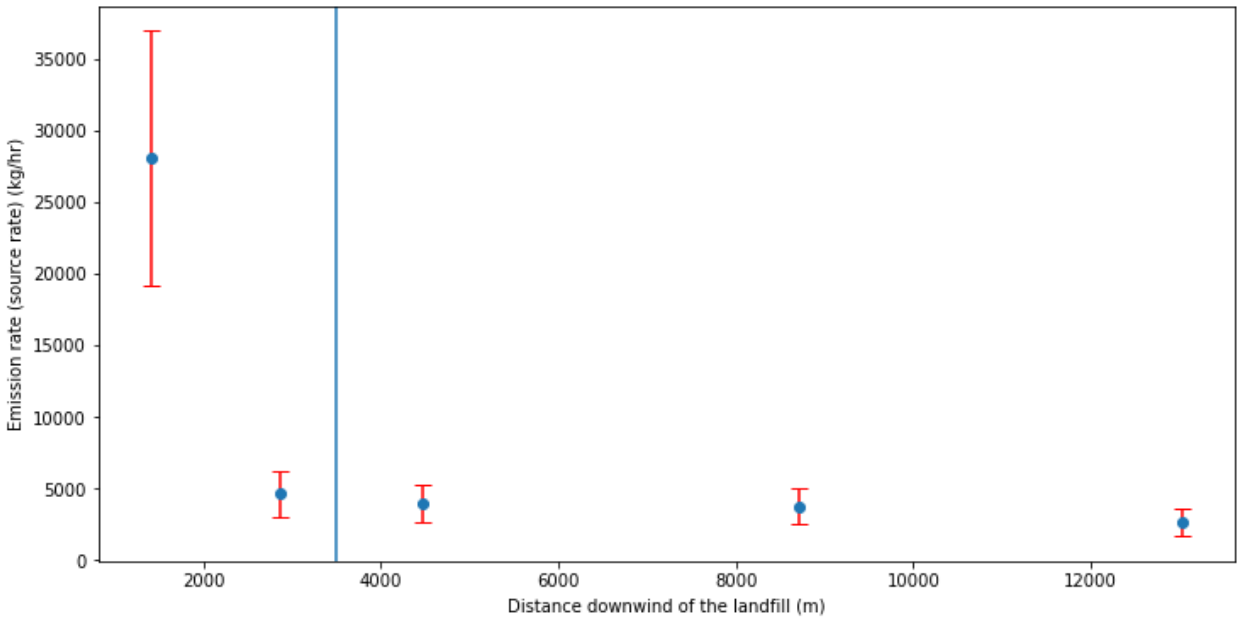

Figure 3.13: Estimates of methane emissions calculated by mass balance method for study B. Blue line indicates the distance 3 t_m at which the plume is well mixed within the PBL.

3.3.3. Study C on July 7th, 2022

On July 7th, summertime field study was performed to compare with previous studies performed during October and February in order to identify any potential seasonal variation in the emission rate of methane. However, due to the inadequate meteorological conditions, the data from this study could not be used to quantify methane emissions.

The measurements were made between 11:08 AM and 13:06 PM. Maximum observed methane was a sharp 2.73 ppm peak which was much less than what was measured from Study A and B. The overall driving map and the time series plot of methane are shown in Figure 3.14.

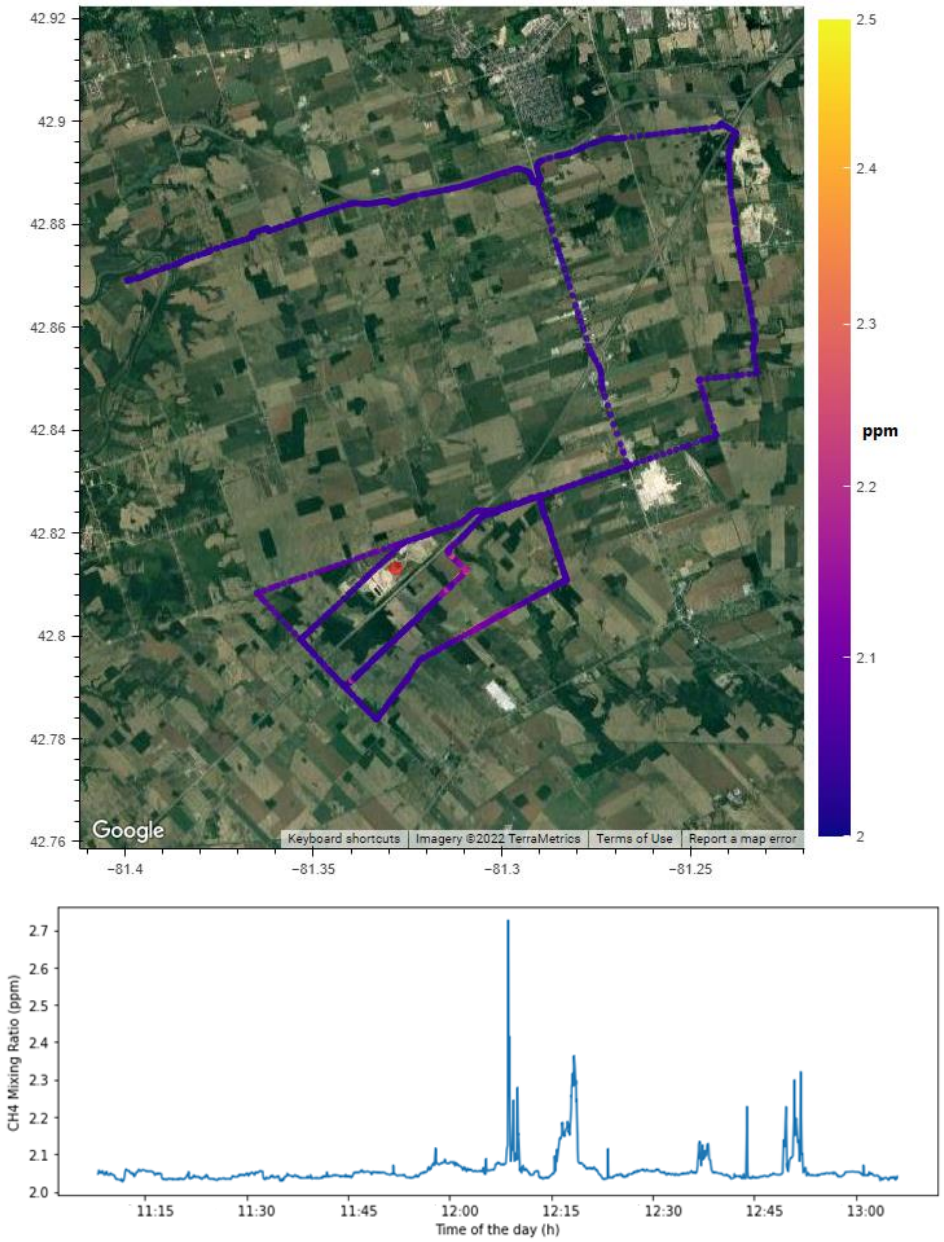

Figure 3.14: (Top) Map of methane mixing ratios from study C between 11:08 AM to 13:06PM (EST) (Bottom) Time series plot showing multiple sharp peaks. No strong methane enhancement was observed similar to previous studies A, and B.

The meteorological conditions were extremely unstable on this day. The wind direction had high variability, frequently shifting between N and S. Initial measurement was performed at

north transects of the landfill since wind forecast predicted south wind. However, on site measurement revealed wind direction shifted to NW. Wind speed were extremely low, much lower than the forecast. Wind speed recorded by both Met tower and London station were ranging between 0 – 2 m/s (Table 3.4).

Table 3.4: Summary of meteorological parameters for study C.

Time (EST)	*Wind speed (m/s)*	*Wind direction (deg)*	*Pressure (kPa)*	*Temperature (K)*
11:00	2.2	30 ± 80	98.48	295.9
12:00	1.4	290 ± 90	98.49	296.9
13:00	1.9	60 ± 80	98.44	296.7
Average	1.8 ± 0.3		98.47 ± 0.02	296.5 ± 0.4

It was a clear sky day with strong solar insolation. The Downwelling Solar Radiation obtained by the GOES satellite is 693 W/m^2. Boundary layer height is estimated to be 1100 m by NCEP model which is much greater compared to study A and B. In an extremely unstable boundary layer from lack of mechanical wind shear (< 2 m/s) and strong solar radiation (> 600 W/m^2), vertical updraft can quickly mix and dilute methane within its high boundary layer. Further meteorological analysis can be performed based on the aircraft landing data from ADMAR. Ascent sounding data from London on July 7th at 16:31 UTC is obtained and plotted in Figure 3.15. At approximately 900 m above ground, an isothermal point is observed which corresponds to the potential boundary layer height and another elevated inversion layer is noted at 2070 m. Linear regression of temperature gradient up to the isothermal point shows superadiabatic lapse rate of -10.6 °C/km, greater than dry adiabatic lapse rate of –9.8°C/km. The superadiabatic (unstable) atmospheric condition results in rapid up and down vertical mixing, which creates a looping plume below the isothermal layer as in Figure 3.16 (Weiner et al., 2003). This can create a zone, especially close to the source, where no plume is observed as most of the emitted methane plume is transported upward before it falls back down to create a zone with high level of methane near ground at further downwind distance. This can potentially account for low level of methane observed compared to study A and B as measurement was only performed close to the source. As it is difficult to predict and capture the movement of plume under such condition, extremely unstable atmospheric condition is highly undesirable for the mobile measurement.

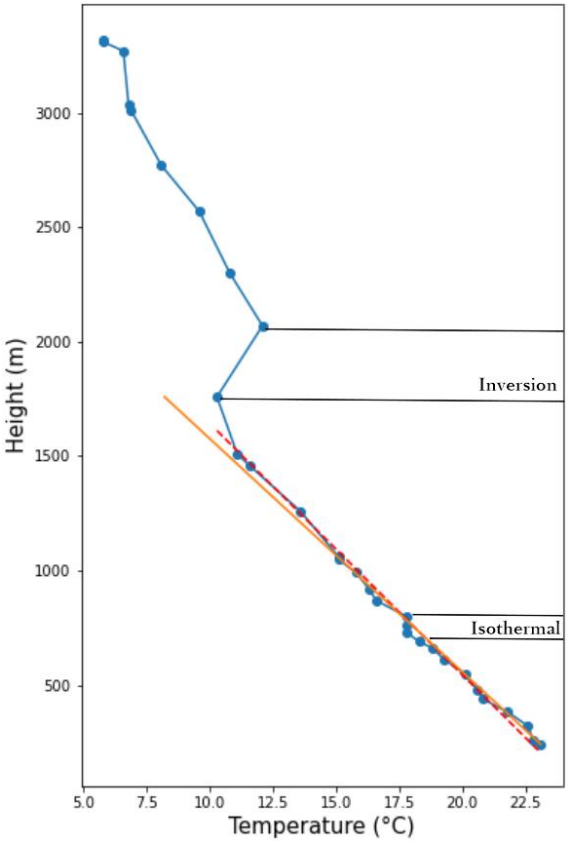

Figure 3.15: Vertical temperature profile from AMDAR, London ascent sounding data 16:31 UTC July 7th, 2022. Dotted red line indicates linear regression lapse rate and solid orange line depicts dry adiabatic lapse rate.

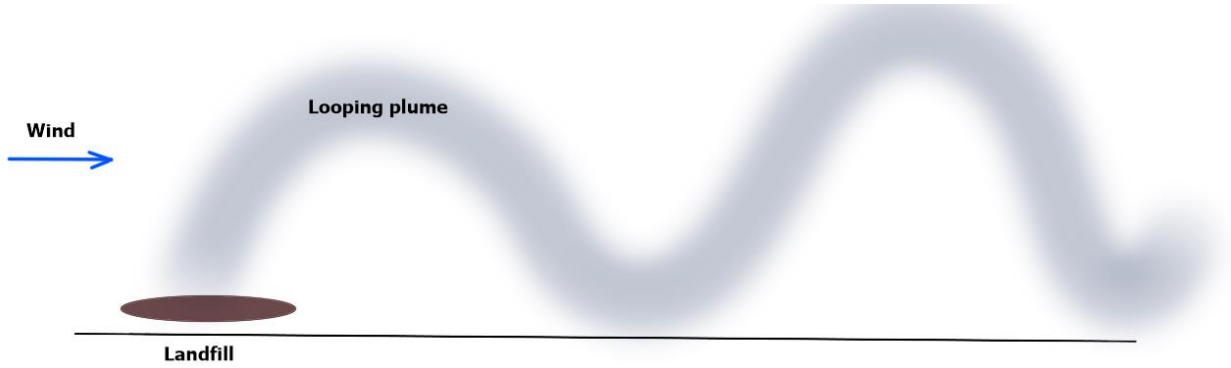

Figure 3.16: Diagram of looping plume created from the strong lapse rate condition.

Another potential explanation for low observation of methane on this day is from a lower emission rate at the surface due to methanotroph oxidation. Community of methanotrophs on the surface of the landfill uses CH_4 as source of energy and such aerobic CH_4 oxidation plays an important role in mitigating CH_4 release from landfills to the atmosphere (Su et al., 2014). As

previously noted in the introduction, landfill CH_4 emission decrease with increased ground temperature in dry soil conditions, (Scheutz et al., 2004; Riddick et al., 2016) between 2 to 25 °C. Temperature on the day was 23.35 °C which signifies an ideal temperature for methanotroph activity. Therefore, surface oxidation barrier by methanotrophs could have potentially oxidized methane emitted from landfill to a greater extent compared to the winter study with temperature of 5 °C.

3.3.4. Study D on October 1st, 2022

Study D was performed on October 1st, 2022, between 1:28 PM to 3:22 PM. Since the forecast predicted wind direction to be from northeast, methane mixing ratios were measured downwind along 4 different transects southwest of the landfill as illustrated in Figure 3.17. The meteorological conditions are presented in Table 3.5.

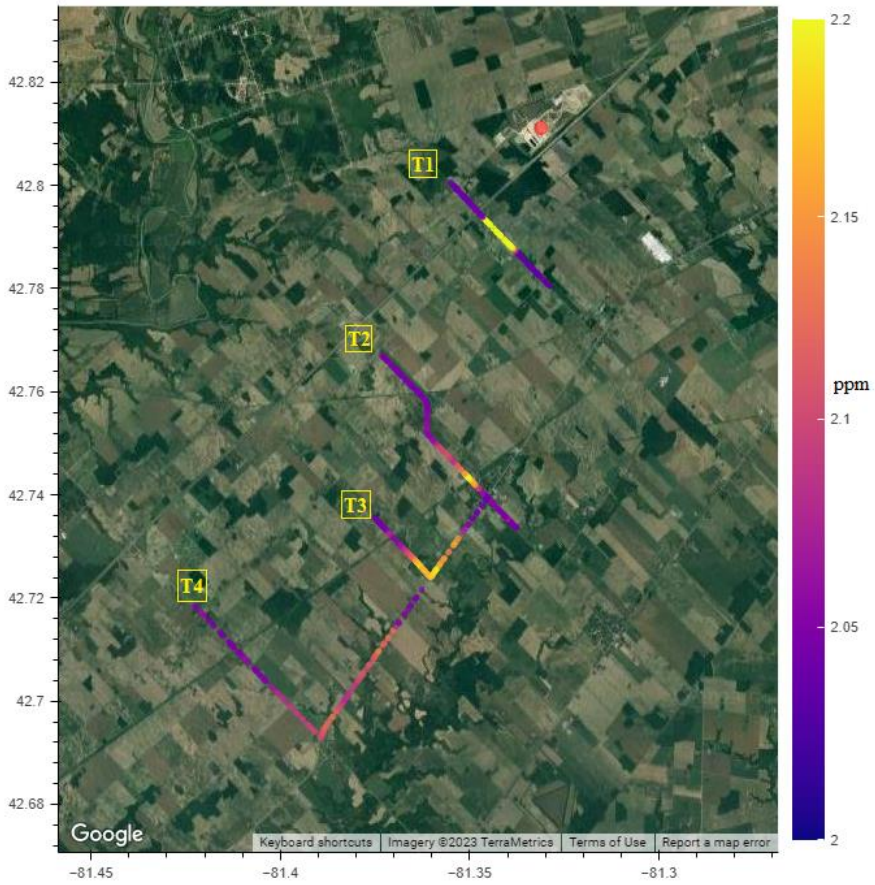

Figure 3.17: Map of CH_4 mixing ratios from Study D. Red dot indicates the location of potential hotpot on the landfill.

Table 3.5: Summary of meteorological parameters for study D.

Time (EST)	*Wind speed (km/h)*	*Wind direction (deg)*	*Pressure (kPa)*	*Temperature (K)*
14:00	3.9	20	98.80	291.35
15:00	5.8	40	98.74	291.75
16:00	4.7	10	98.70	292.45
Average	4.8 ± 0.6	20 ± 10	98.75 ± 0.03	291.9 ± 0.3

Compared to study A which showed a high methane enhancement with maximum value of 23.38 ppm at 770 m from the landfill, study D demonstrated much smaller enhancements at all downwind transects. The highest observed maximum methane mixing ratio was 3.31 ppm on the closest transect T1, at a downwind distance of 2200 m from the source. At the furthest transect,

peak maximum corresponded to 2.14 ppm on T4. The differences in angle between the transect direction and wind direction were taken into account to find the perpendicular component of the wind speed. For transect 3 and 4, the road system was not exactly perpendicular to the wind direction to capture the plume. Therefore, the transect was divided into 2 sections (left and right transects), and the flux along each component was calculated and summed to provide a total emission rate. Along with the NCEP and ceilometer data, aircraft landing data by AMDAR was used to estimate the boundary layer height as seen in Figure 3.18. Appendix Table B.1 provides a summary of the boundary layer and the kinematics parameters for study D.

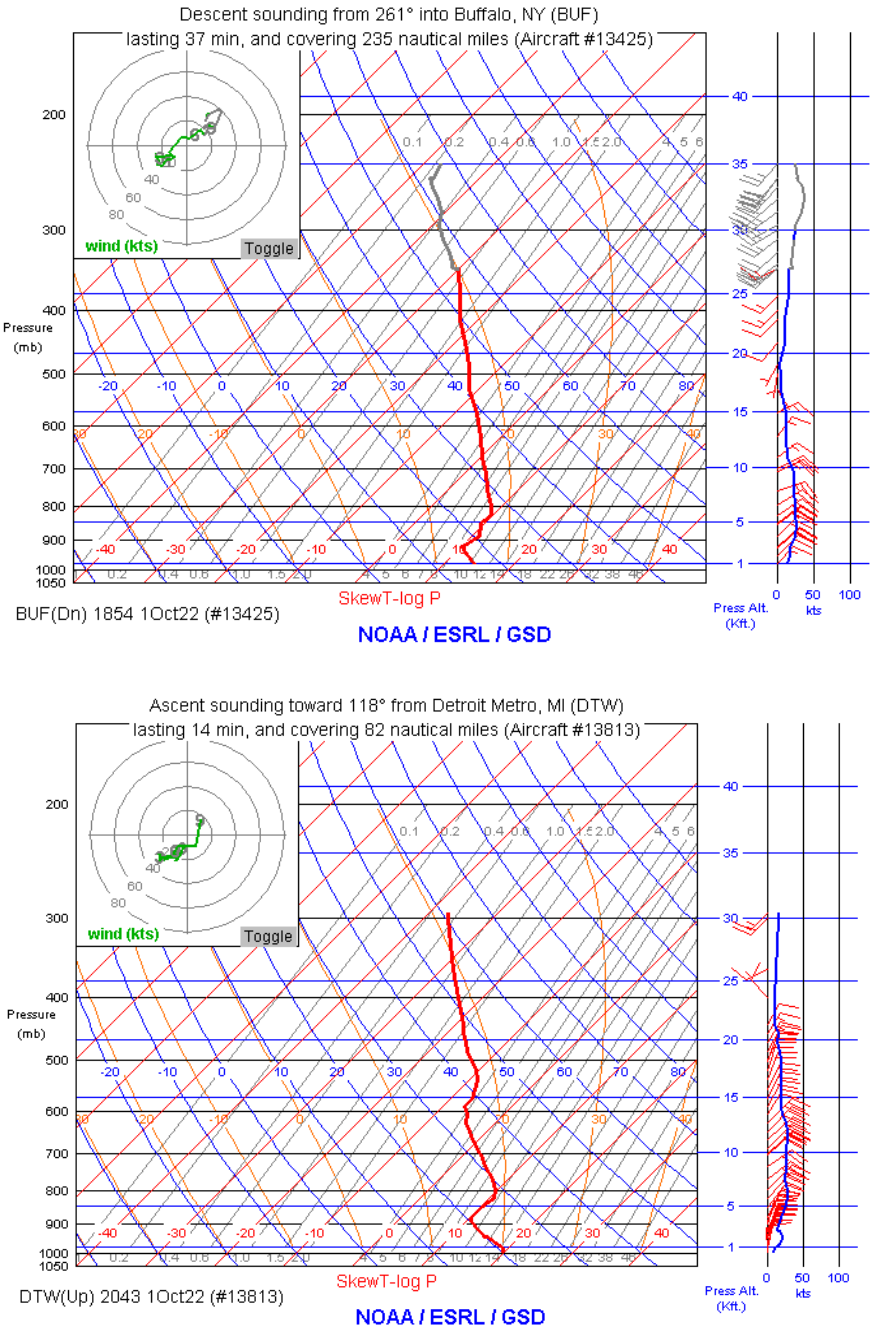

Figure 3.18: Temperature profiles from the flight landing data on October 1st. (Top) At BUF airport on 18:54Z showing temperature inversion at 925 mb (0.8 km) (Bottom) At DTW airport on 20:43Z with temperature inversion at 891 mb (1.1 km)

Based on the following parameters: T0 peak at 2.2 km downwind distance, methane enhancement of 1.26 ppm, and stability class of B, estimation by gaussian formulation at the

closest transect, T0 results in methane emission rate of 1040 g s^{-1} equivalent to 3744 kg h^{-1} The calculated value is slightly higher than the rates estimated in previous studies A and B.

Convective mixing time was calculated to be 438 s which makes the homogenous mixing distance 6300m. The calculated emission rates are plotted against the downwind distance in Figure 3.19. The 3 data points beyond the line are presumed to be valid, and the average of emission rates is 3200 ± 830 kg h^{-1}.

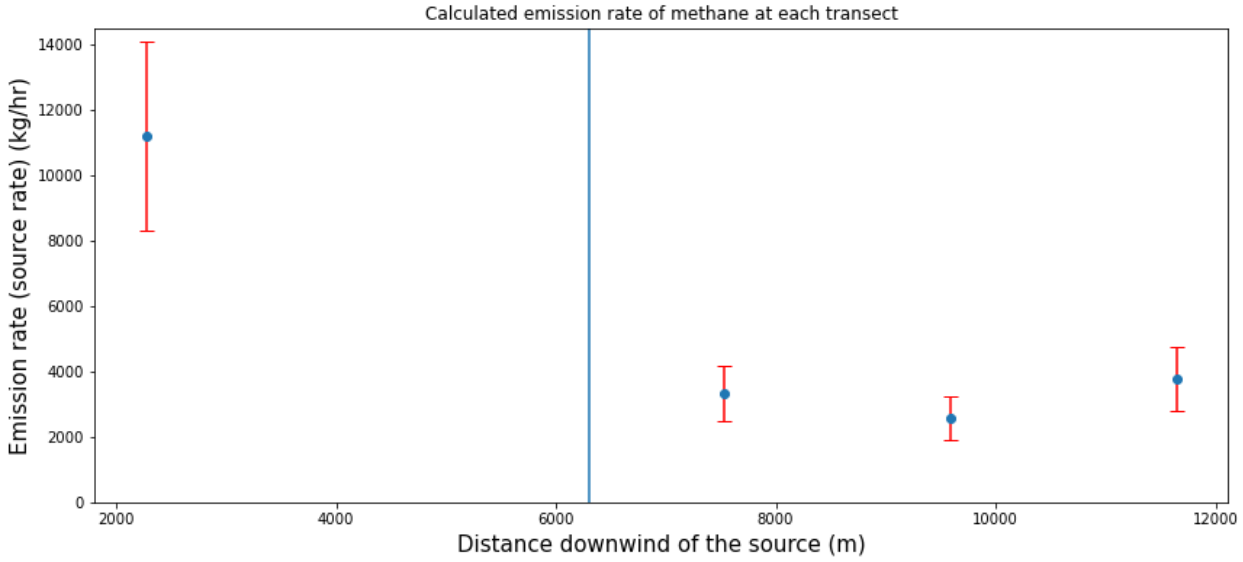

Figure 3.19: Mass balance calculated emission rates for study D along T1, T2, T3 and T4. The blue line indicates the distance $3t_m$ at which the plume is well mixed within the PBL.

3.3.5. Discussion

For the mass balance estimation, Study B corresponded to 3400 ± 1200 kg h^{-1} and Study D was 3200 ± 830 kg h^{-1}. The average calculated emission rate of methane from Greenlane landfill was 3300 ± 730 kg h^{-1}. Figure 3.20 shows the comparison of the study B and D which depict the converging emission rates to approximately 3300 kg h^{-1}, depicted by a green line on the plot on both studies past the well mixed distance that describes the minimum downwind distance from the source to assume homogeneous vertical methane profile.

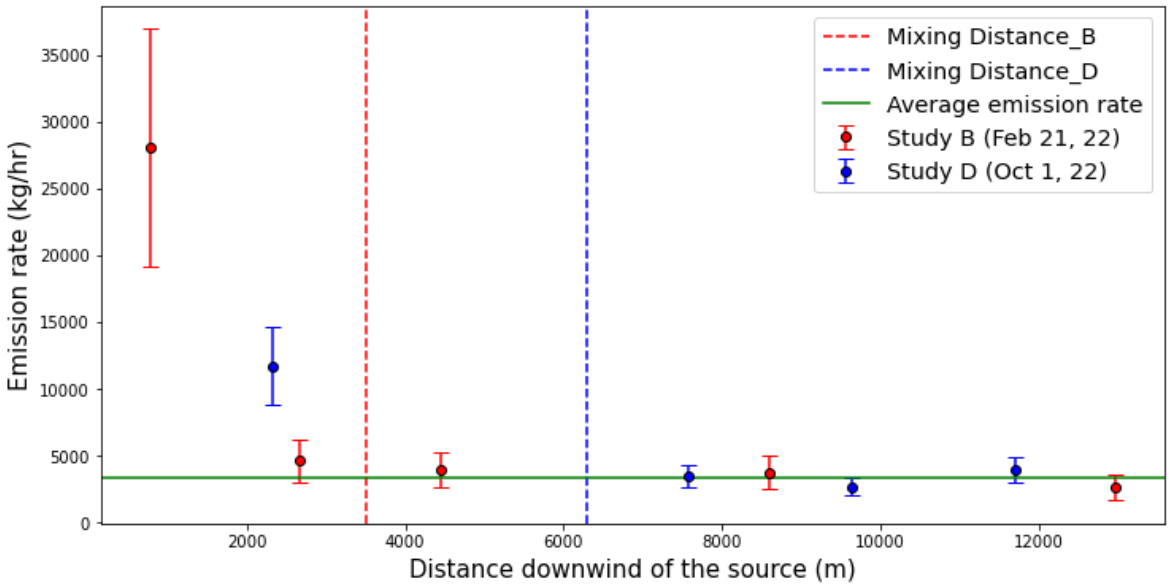

Figure 3.20: Comparison of the emission rates calculated for study B and D by mass balance method showing the converging emission rate to the average emission rate of 3300 kg h^{-1} depicted by the green horizontal line.

Table 3.6 summarizes all methane emission rates estimated by the Gaussian model on the closest transects during the study. Excluding study C, which had extremely unstable meteorological condition, the average of source rate estimated by Gaussian formulation was 3320 ± 250 kg h^{-1}. The calculated rate is in good agreement with the emission rate estimated by the mass balance method.

Table 3.6: Summary of Greenlane landfill's methane source rate estimated based on gaussian model.

	Downwind distance, x (km)	*Enhancement above background (ppm)*	*Source rate based on gaussian model (kg/h)*
Study A Peak 1 at 10.56 AM	2	12.5	3103
Study A Peak 2 at 11:26 AM	2.5	8.72	3240
Study B	0.77	21.28	3197
Study D	2.2	1.28	3744
Average			3320 ± 250

Despite similar emission rates, there were quite large differences in the methane mixing ratios observed close to the landfills in these studies (see Appendix Table B.2). The observed maximum mixing ratios at each transect for each study A, B, and D are shown in the plot in Figure 3.21. The curve fit by a general Gaussian function shows that the observed maximum values follow the trend, except for Study A, which is likely inaccurate due to inadequate meteorological conditions.

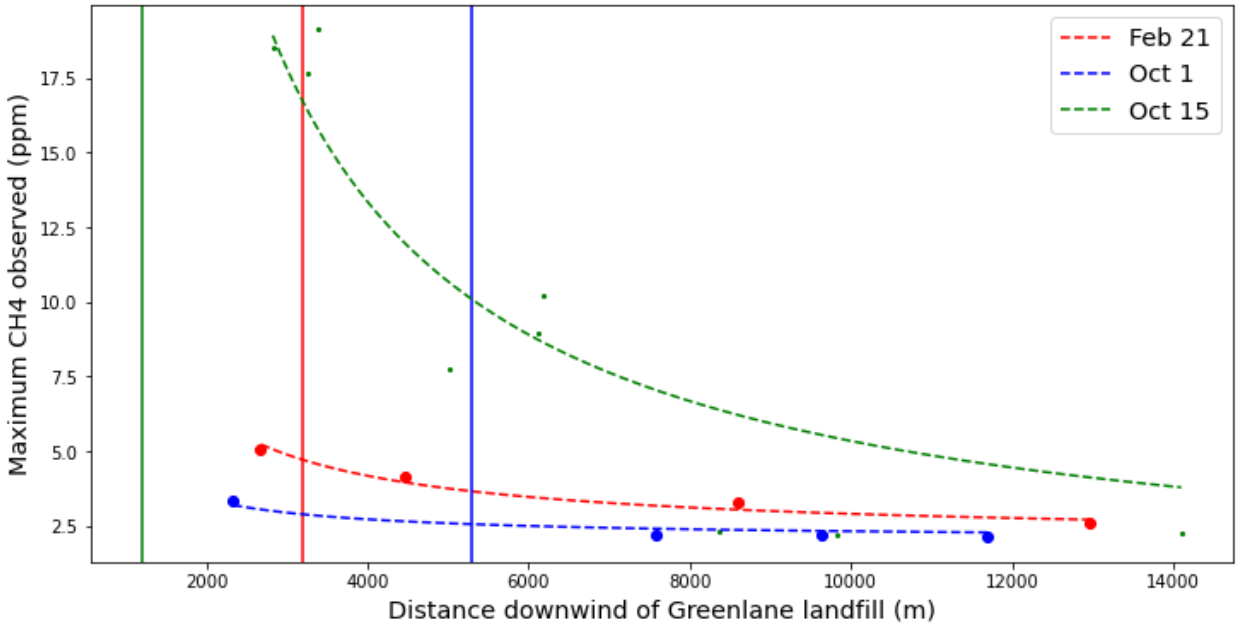

Figure 3.21: Maximum CH_4 enhancement for each transect plotted together for comparison between study A, B and D. For A and D, closest transect value was excluded. Dotted lines indicate curve fit lines by gaussian function.

The methane enhancement observed in all studies showed a negative correlation with the boundary layer height, as expected. Study A, B, and D had boundary layer heights of 360 m, 420 m, and 1000 m, respectively, and higher maximum enhancements were observed for lower boundary layer heights. Appendix Table B.3 provides a summary of the meteorological data for four studies discussed here. Between Study B and study D, the downwelling solar radiations were similar at, 443 W/m^2 for Study B and 433 W/m^2 for Study D. However, the atmospheric temperature was much lower in Study B at 5 °C compared to study D, 18 °C due to the insulation effect of snow coverage. Snow on the surface reflects part of shortwave radiation, resulting in much lower absorbed energy for the surface energy budget. This also resulted in drastic difference in Deardorff velocities and mixing times, as they are proportional to the

surface atmospheric temperature. Furthermore, PBL development was affected by multiple meteorological factors, not just solar insolation reaching the surface. These factors include atmospheric stability, surface temperature, albedo, and relative humidity (Zhang et al., 2013). Elevated surface temperatures lead to increased sensitive heat flux, which results in higher boundary layer development during daytime. It can be understood that higher surface temperature had a stronger influence on the development of boundary layer height than direct solar insolation, and the development of higher boundary layer height caused stronger vertical mixing and dilution of methane. Therefore, for study D, greater surface heat flux caused higher boundary layer height, leading to much faster updraft speeds in convective thermals and resulting in rapid mixing and lower observed maximum enhancement. Conversely, for study B, the snow cover reduced the surface heat flux, which prevented the development of a boundary layer and resulted in higher mixing ratios of methane trapped in lower boundary layer.

The differences in pressure between studies were not significant, but they followed the expected inverse relationship with the observed maximum mixing ratios. The observed station pressures from London station can be ranked in order of study D (98.75 kPa) > B (98.58 kPa) > A (97.97 kPa), with a difference of 0.78 kPa between D and A. This correlation could suggest that higher pressure supresses methane emission from the landfills. However, study C shows lower station pressure relative to B, which does not clearly follow the trend. The effect of pressure on methane emissions seems minimal compared to the greater influences from the effect of temperature and the development of boundary layer.

3.3.6. Inventory Evaluation

Based on the calculated average emission rate of 3300 ± 730 kg h^{-1}, Greenlane landfill would have an annual emission rate of 29 ± 6 kt/year, assuming no seasonal variability and constant emissions throughout the year. According to the 2020 GHG emission inventory for Ontario, shown in Figure 3.22, the total methane emissions from the province were 516 kt CH_4 with 270 kt attributed to solid waste disposal at landfills. Therefore, the methane emission from Greenlane landfill represents 5.6% of Ontario's total methane emission and 10.7% of the methane emission from the waste management sector.

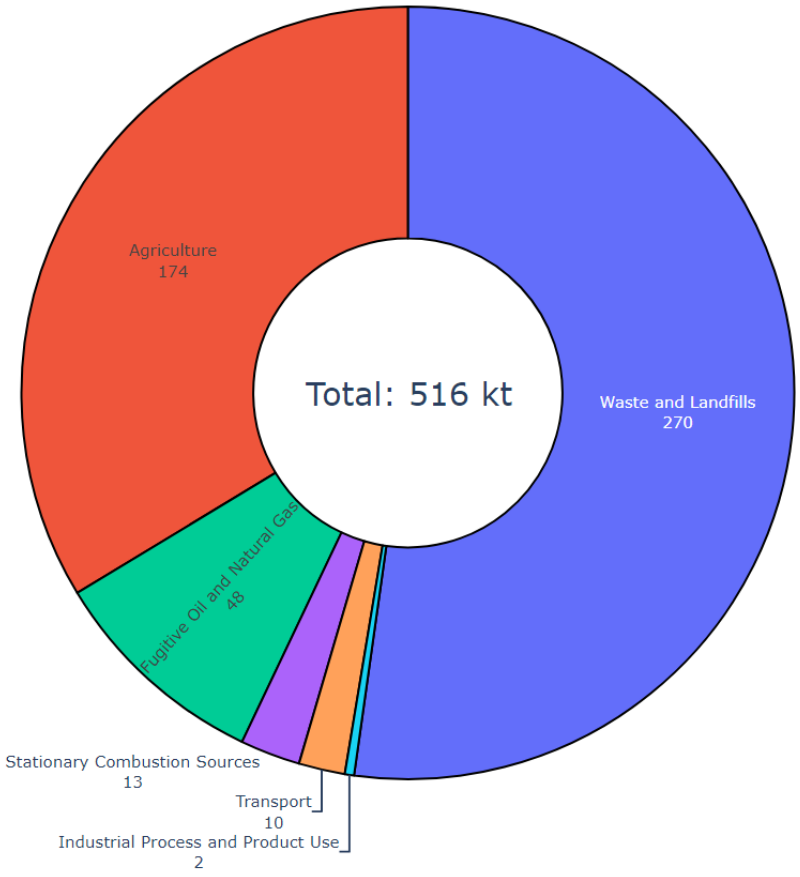

Figure 3.22: 2020 Ontario Inventory methane emissions by sector, values reported in kt (total emission of 516 kt)

The Greenhouse Gas Reporting Program (GHGRP) collects annual information of facilities that emit more than 10 kt of GHGs in CO_2 eq. across Canada. According to the GHGRP 2020 database, emissions of CO_2 from green lane landfill was 3951 tonnes and CH4 was 2100 tonnes. Summary of the annual inventory values from the GHGRP values are plotted on Figure 3.23.

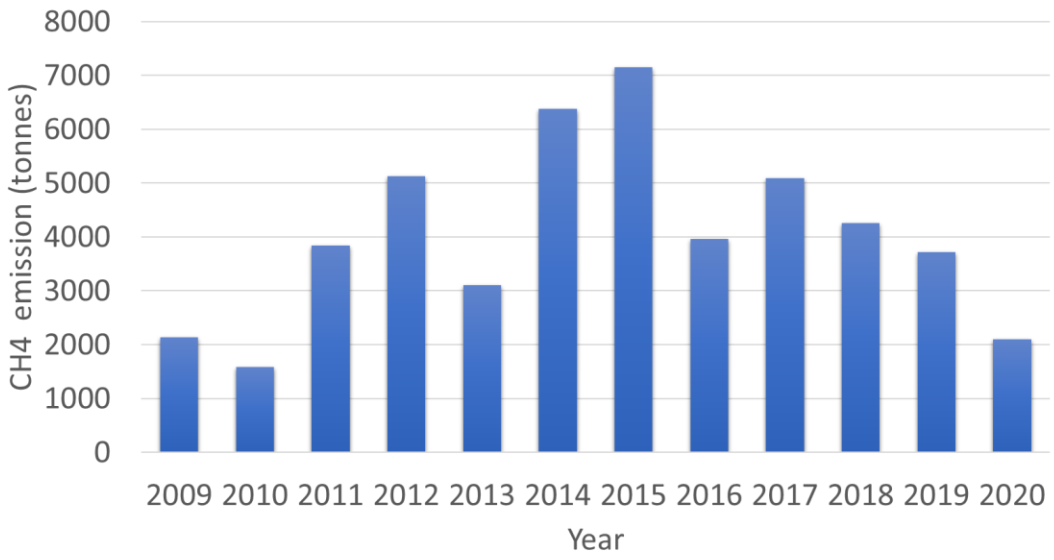

Figure 3.23: Annual CH_4 emission from the Greenlane landfill by GHGRP

The notable trend is that the GHGRP inventory is estimating a decrease in methane emissions from 2015 onward, even though the landfills is accepting an increasing number of wastes. Comparing the 2017 Greenlane landfill annual progress report from WSP and 2021 report from Ontario Waste Management Association, the amount of waste disposed of at the landfill almost doubled in 4 years, from 502,210 tonnes/year to 1,100,000 tonnes/year. This increase in waste generation should indicate a rise in methane emissions in the upcoming years. However, this decrease in methane emissions trend is observed for many landfills, including both currently operating and closed down landfills (KVL in Chapter 2). One possible explanation for this trend is that the landfills are equipped with better landfill gas collection system and increased composting of organic wastes. Similarly in US, even though the amount of waste generated increased each year between 1990 to 2010, the actual net methane emissions decreased over years due to similar reasons (Bronstein et al., 2012).

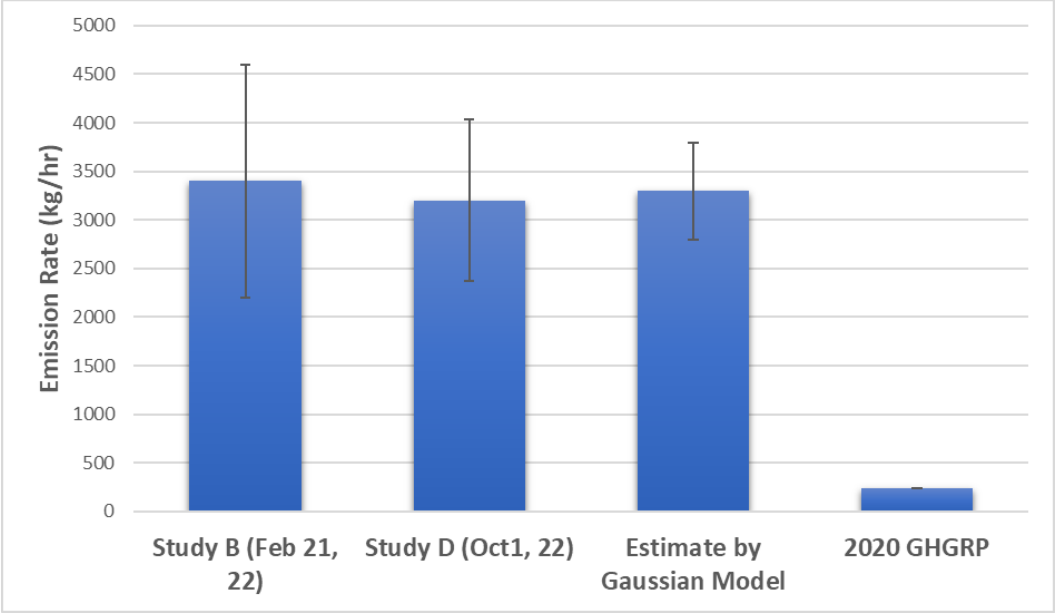

Figure 3.24: Comparison of methane emissions estimates by different methods: mobile mass balance estimates from 2 different studies B and D, average of gaussian model estimate throughout study A - D, and 2020 GHGRP inventory value based on emission factor.

There is a good agreement between the mobile mass balance estimates from studies B and D, as well as the average of emission rates estimated by the Gaussian model in multiple studies. However, the reported 2020 GHGRP value of 240 kg h^{-1} for Greenlane landfill is significantly lower compared to 3300 ± 730 kg h^{-1} (average mass balance estimate) and 3320 ± 250 kg h^{-1} (average Gaussian model estimate). The on-site measurement estimates are 10 times larger than the GHGRP value, representing a large discrepancy between top-down measurement and the bottom-up inventory.

This discrepancy between the top-down measurements to the bottom inventories has recently been highlighted and observed for many different studies across US and Canada and likely implies that the core problem lies in the inventory model. There exist two different bottom-up approaches for US and Canada to quantify methane emissions from landfills: National Inventory of Sources and Sinks, and the Greenhouse Gas Reporting Program (GHGRP) which is relatively newer program by the EPA and ECCC since 2010. Both methods rely on the primary first order decay model to estimate methane generation rates from landfills. The main difference lies in the estimation of recovered landfill gas. The Inventory uses the data from the combination of secondary data sources for the amount of waste and recovered landfill gas. In addition, the

method assumes landfills are equipped with gas recovery systems with an average efficiency of 75%. These assumptions present as the most significant uncertainties in estimating the amount of gas recovered. On the other hand, the GHGRP is based on the onsite flow rate measurement data reported by the facility. By incorporating the data of measured recovered gas and estimating the efficiency of the gas collection system, the GHGRP is expected to have lower uncertainty of ~5% (Bronstein et al., 2012). Yet, the result from this study compared to GHGRP shows that the method is not adequately estimating the gas collected throughout the landfills.

Since both the inventory and the GHGRP relies on 2006 IPCC methodology, they do not consider soil or climate factors for potential seasonal variability in methane generation and oxidation rates (Spokas et al., 2015). This provides an additional uncertainty, especially on the oxidation by cover soils as both methods employ 10% as default value. However, even if the model estimates assume oxidation rate of 0%, the 10% increase in emission value would not be enough to cover the gap between the result of mobile measurements to the GHGRP estimates which imply uncertainty from oxidation rate is relatively minor compared to the uncertainties on methane generation rate and the loss by the gas collection system.

3.3.7. Estimate of CO_2 emissions from the landfill

As discussed earlier in the introduction. it is known that landfill gas (LFC) generated by the anaerobic activity of methanogens generates approximately 1:1 methane to carbon dioxide by volume, depending on the type and amount of waste disposed at the landfill, as well as moisture, and soil conditions. About 1 year after the waste is deposited at the landfill, it enters phase 1 and starts to produce landfill gas. Figure 3.25 depicts the landfill gas development through different phases after wastes disposal. It takes up to 5-7 years for the landfill gas to mature to phase 4, where methane becomes the major component of the landfill gas (EPA, 1995).

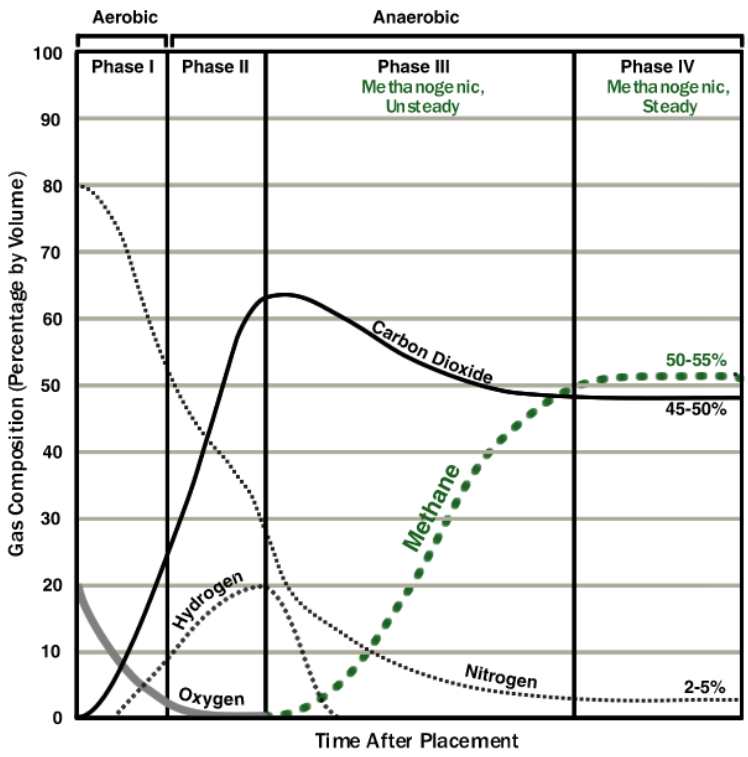

Figure 3.25: Figure of landfill gas development over different phases (EPA, 1995)

If the ratio of enhanced CH_4 to CO_2 is measured, it is possible to calculate the source rate of CO_2 once the rate of CH_4 has been calculated by the mass balance method. This correlation of CO_2 with CH_4 was calculated using the data from studies A, and B when the vehicle was travelling in the plume measuring the enhancement. Figure 3.26 illustrates the CH_4 and CO_2 mixing ratios during the measurement on October 15th, 2021, for study A. Secondary CO_2 sources, notably traffic could affect measured CO_2. Therefore, the times at which the traffic was observed nearby was subtracted from the dataset. The methane shows good agreement in the enhancement pattern compared to the measured CO_2 values. Figure 3.27 illustrates the linear regression between CO_2 and CH_4 showing strong correlation, with a slope of 1.13 ± 0.04 mole mole^{-1} which shows almost 1:1 enhancement of CO_2 to CH_4. The *y*-intercept of 435.6 ± 0.3 ppm indicates the background CO_2.

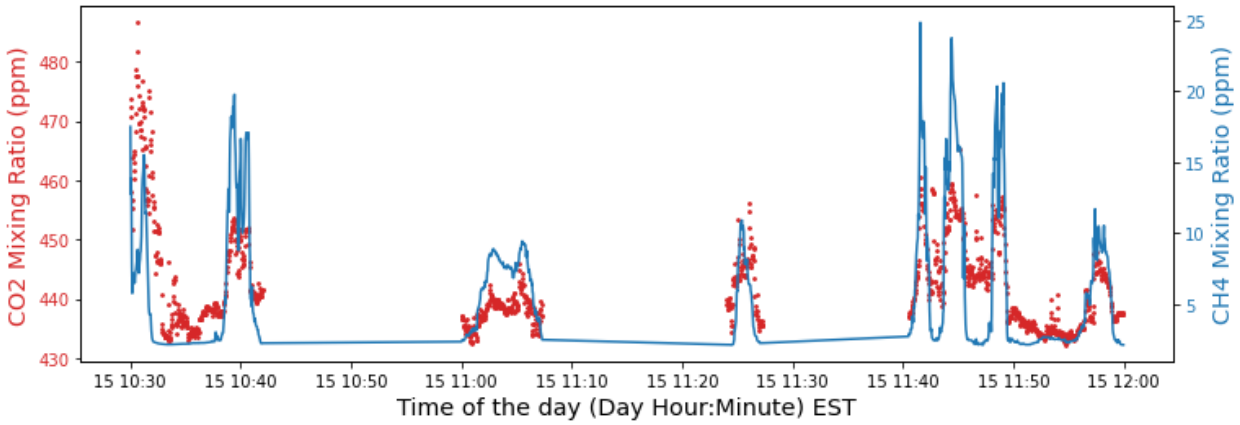

Figure 3.26: Comparison plot of CO2 and CH4 mixing ratios observed on October 15, 2021, preliminary study. CO2 data points with nearby traffic excluded.

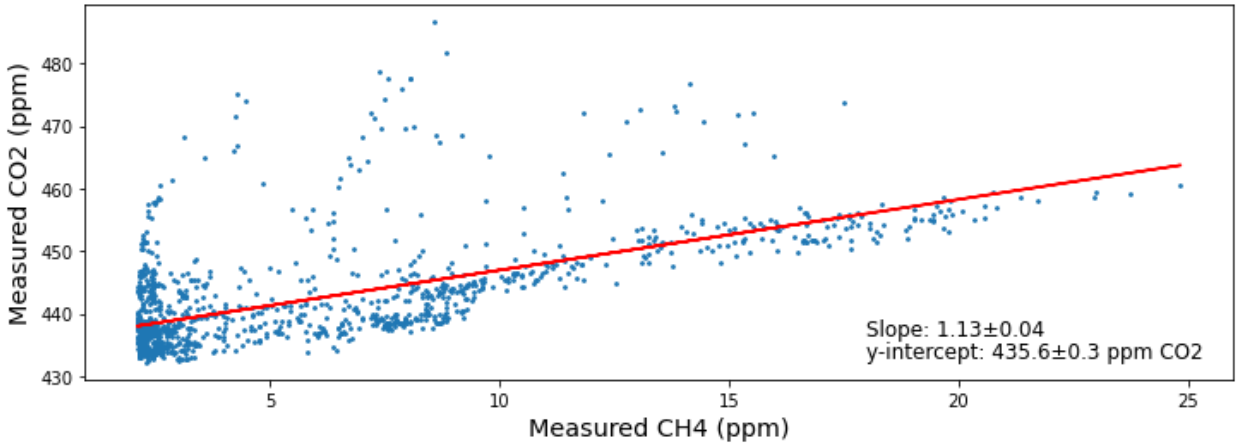

Figure 3.27: CO_2 vs. CH_4 linear regression plot showing strong 1:1 correlation for Study A

Similarly, correlation between CO_2 and CH_4 was calculated for the data from study B on February 21st, 2022. However, it was observed that the shape of CO_2 plumes depicted the presences of several nearby interferences by showing irregularities and multiple sharp peaks for further downwind transects since there were various local CO_2 sources mainly nearby traffic and the agricultural activities. Therefore, only the data points from the first two transects were used to calculate the correlation to eliminate the interferences from other CO_2 sources. The correlation calculated for Study B shows linear regression slope of 0.84 ± 0.02 mole mole^{-1} with a *y*-intercept of 425.8 ± 0.2 ppm CO_2 as shown in Figure 3.28.

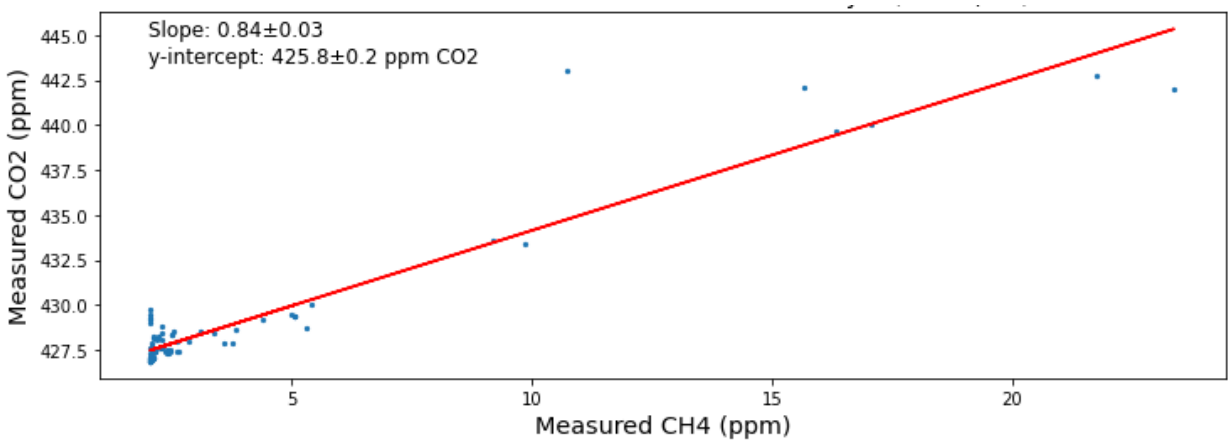

Figure 3.28: CO_2 vs. CH_4 linear regression plot with only nearby transect 0 and transect 1 data points where CO2 mixing ratios were least affected by secondary emissions such as traffic (February 21 study)

Excluding study C, when the plumes could not be identified clearly due to the inadequate meteorological condition, study D showed similar correlation between CH_4 and CO_2, but enhancements were much smaller being more prone to local sources and noises, so they were not used. Assuming theoretical 1:1 emissions of CO_2:CH_4, it is likely that CO_2 had similar maximum enhancement of 0.16 ~1.26 ppm even on the two closest transects. Considering the background fluctuation in the CO_2 value was much greater than the possible enhancement from the landfill CO_2 emission, it would have not been possible to pick out the enhancement and masked by the background CO_2 fluctuation as well as various nearby CO_2 interferences.

From the mass balance equation shown previously in chapter 1, combining all terms that share the same value for both CO_2 and CH_4, the equation can be simplified to equation below where MW is molecular weight of the species, X_{enh} is the enhancement of the species in ppm.

$$Emissions\ of\ X = MW_X \times constant \int_{-s}^{s} X_{enh}\, ds$$

From the correlation plot from both studies, $[CO_2]_{enh} = 0.99 \pm 0.04$ mole mole $^{-1}$ $[CH_4]_{enh}$. Therefore, emission of CO_2 can be calculated by calculating the ratios,

$$\frac{Emissions\ of\ CH_4}{MW_{CH4}} = \frac{Emissions\ of\ CO_2}{0.837 MW_{CO2}}$$

Using the average emission rate of 3300 ± 730 kg h^{-1} emission rates of CH_4, calculated CO_2 rate is 7600 ± 1700 kg h^{-1}. As a comparison, the land GEM model employed in chapter 2 was

used to estimate 73400 Megagrams/year emission of CO_2 equivalent to 8380 kg h^{-1}, falling within the uncertainty range of the estimated CO_2 rate.

3.4. Conclusion

The study demonstrates a convenient and cost-effective methodology to investigate and estimate the methane emissions by the surface-based mass balance method employing the cavity ringdown spectrometers on a mobile vehicle. During 2021 to 2022, 4 different field studies were performed at Greenlane municipal landfill to determine the emission rates of methane as well as emission characteristics and potential season variability. The result showed that nominal seasonal variability in methane emissions with good consistency observed between late summer (study D) and wintertime measurement (study B), with calculated source rates of 3200 ± 830 kg h^{-1} and 3400 ± 1200 kg h^{-1} respectively. The average methane emission rate of 3300 ± 730 kg h^{-1} was much lower than the 240 kg h^{-1} reported by the National Greenhouse Gas Reporting Program (GHGRP) which is likely due to model's inability to take site specific variables into account such as climate, soil, and operational variables, especially land fill gas collection system and efficiency. Since the methanotrophic oxidation barrier on the surface of landfill as well as the landfill gas collecting system has significant influence on the emission rate, which are not well considered in the inventory modelling, it is important to design further studies to analyze their impact on emission rates along with the effective top-down measurement methods to abate the current gap between the two approaches. Especially, the bacterial methanotrophic oxidation will also depend on the meteorological parameters and soil conditions which can produce different seasonal variations in emission rates that the annual emission cannot simply be estimated by extrapolating the data obtained from few discrete studies.

The 4 different case studies showed that the boundary layer and surface temperature had a major influence on the observed methane enhancement at downwind transects, with higher boundary layer developed by greater sensible heat flux from the surface heat causing methane to be diluted vertically. This can potentially make the measurement more difficult as smaller enhancements at the level of tens of ppb values are difficult to identify as it was observed in study C and the data is most likely not usable to observe the CO_2 correlation. Although it is

difficult to conclude with lack of sample size and proper barometer to measure the pressure, pressure seemed to have a negative correlation with the observed methane enhancement.

The transport of the plume was majorly determined by the wind vector and in order for the field measurement to give correct estimate, it is especially important for the wind direction be consistent throughout the measurement. For the quantifiable studies, B and D, the observed lateral dispersion followed a gaussian curve shape with the maximum enhancement in good agreement with the values estimated by the gaussian dispersion calculation. Further inverse dispersion modelling can be used to backtrack the plume source and identify the location of hotspots which would be essential in planning out the local mitigation strategy.

The method also showed that in case of landfills with known ratio of gas emission, CO_2 rate can be estimated based on simple correlation using CH_4 data. From the average CO_2:CH_4 ratio 0.99 ± 0.04 mole mole $^{-1}$, it is shown that the landfill also emits large quantity of CO_2 of 7600 ± 1700 kg h^{-1}.

Chapter 4: Quantifying Methane Emissions from Sarnia

4.1. Introduction

Methane is a relatively short-lived greenhouse gas compared to carbon dioxide but 86 times more potent on a 20-year timescale (Myhre et al., 2013). Therefore, curbing down emissions of methane have been highlighted as a key strategy to mitigate the effects of climate change. Predominant anthropogenic sources of atmospheric methane are the fugitive emissions from oil and natural gas production. According to 2020 methane emissions summary for Canada, 1340 kt out of 3700 kt, equivalent to 36% of total methane emissions was the oil and natural gas fugitive sources (ECCC, 2020). The majority of these emissions came from the provinces of Alberta (780kt out of 1500kt province total) and Saskatchewan (361 kt out of 620kt total) where the emission from this sector accounts for more than half of the province's total methane emissions. Ontario's oil and natural gas emissions only account for 9.3% of total methane emissions which was 48 kt in 2020. Even though Ontario's methane emission may not appear as considerable as Alberta and Saskatchewan, the province has the second largest refining capacity after Alberta. 20% of Canada's total oil refining capacity is located in 4 major refineries within Southwestern Ontario: Imperial Oil, Suncor, and Shell in Sarnia and Imperial Oil in Nanticoke. (Canada Energy Regulator, 2022).

Sarnia is a Canadian city located in Southwestern Ontario on the Canada and United States boarder to the east of Port Huron, Michigan. The city has high levels of air pollution from an industrial complex with chemical and oil processing facilities. The immense usage of combustible gases and oils at power plants and petrochemical facilities emit high levels of nitrogen oxides (NO_x) and sulfur dioxide (SO_x). A previous air quality study performed by Davis et al. (2019) employing mobile MAX-DOAS (Multi-Axis Differential Optical Absorption Spectroscopy) showed a NO_x source rate of 1.60 ± 0.34 t h^{-1} and SO_2 emission of 1.81 ± 0.83 t h^{-1}. As petrochemistry is the major business in Sarnia, potential methane sources include the refinery and fractionation plants, chemical plants, and cogeneration facilities. According to GHGRP (2020), 5 contributors accounting for 95% of total methane emissions were Imperial Oil refinery, TransAlta Cogen facility, Imperial Oil Cogen plant, Imperial Oil chemical plant and Suncor refinery, as shown in Figure 4.1.

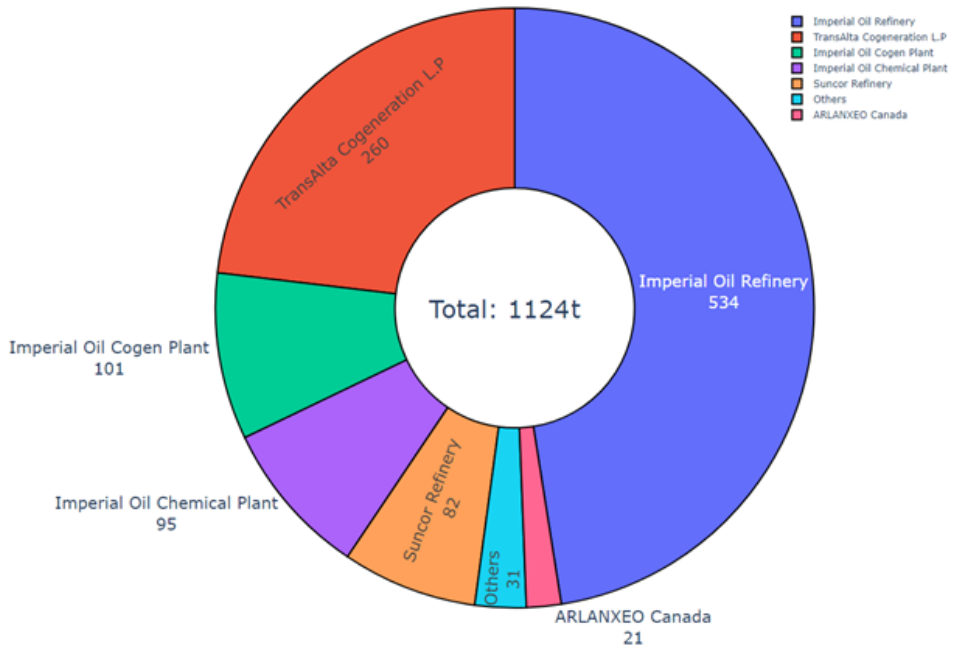

Figure 4.1: Sarnia's industrial methane emission sources (tonnes per year) by facility reported in the GHGRP for 2020

Refineries and power plants employ crude oil and natural gas as primary fuels, and chemical plants use them to create chemical products (e.g., plastics). Therefore, Methane emissions can originate from an incomplete combustion in furnaces of refineries, cold venting, and fugitive emissions across facilities and transportation pipelines (Lavoie et al., 2017).

Even though it is acknowledged that natural gas production and oil refineries prove to be significant methane sources, accurately estimating and characterizing the emissions from those operations is often challenging. Traditional method of emissions estimate involves putting together an emissions inventory by estimating emissions of individual sources at a facility and multiplying an activity by an emission factor to estimate total emissions. However, recent top-down studies have reported that the emissions from oil and natural gas activities are much higher than the reported inventories (Brandt et al., 2014; Baray et al., 2018). Karion et al. (2013) estimated higher levels of emitted methane from oil and gas wells by mass balance approach using aircraft in Utah's natural gas field. Canadian based studies on Alberta's oil and gas operations have shown similar discrepancy between the bottom-up to top-down measurements. Alberta Oil Sands Region (AOSR) measurement by Baray et al. (2018) showed that the hourly estimated emission rate from all facilities were 48 ± 8% higher than the 2013 Canadian

Greenhouse Gas Reporting Program (GHGRP) while airborne measurement by Johnson et al. (2017) over Alberta's oil and gas infrastructures demonstrated that measurements were 4-5 times greater than the inventory-based estimates. These studies highlighted that top-down measurements of emissions are necessary to validate and reconcile with a bottom-up inventory for an accurate quantification of methane sources.

Furthermore, many of the previous papers have emphasized the effect of the "super-emitters" that the emission from natural gas sites is dominated by small hotspots within facilities (Zavala-Araiza et al., 2015). The disproportionate methane emissions from super-emitters make the quantification difficult to be estimated by simple multiplication of a bottom-up inventory. Monitoring the spatial variability in methane emissions for large area sources are often challenging, especially with regard to fugitive emissions from a lengthy pipeline infrastructure and natural gas transportation and distribution system which may benefit from a mobile methane measurement.

This study aimed at demonstrating the mobile mass balance technique as a convenient top-down measurement method for estimating the emissions from large area sources such as a city and industrial facilities. The measurements of methane from the city of Sarnia were performed at downwind transects of the city shown in Figure 4.2 during two-day field studies on July 21st and 22nd 2022. The enhancement patterns of methane measured by Cavity Ring down Spectrometers (CRDS) were characterized by NOAA HYSPLIT back trajectory modelling to identify the sources of the enhancements and Gaussian plume dispersion model was used to estimate individual facility scale emission rates. Total methane emissions across the city and industrial complexes were quantified using the mass balance calculation.

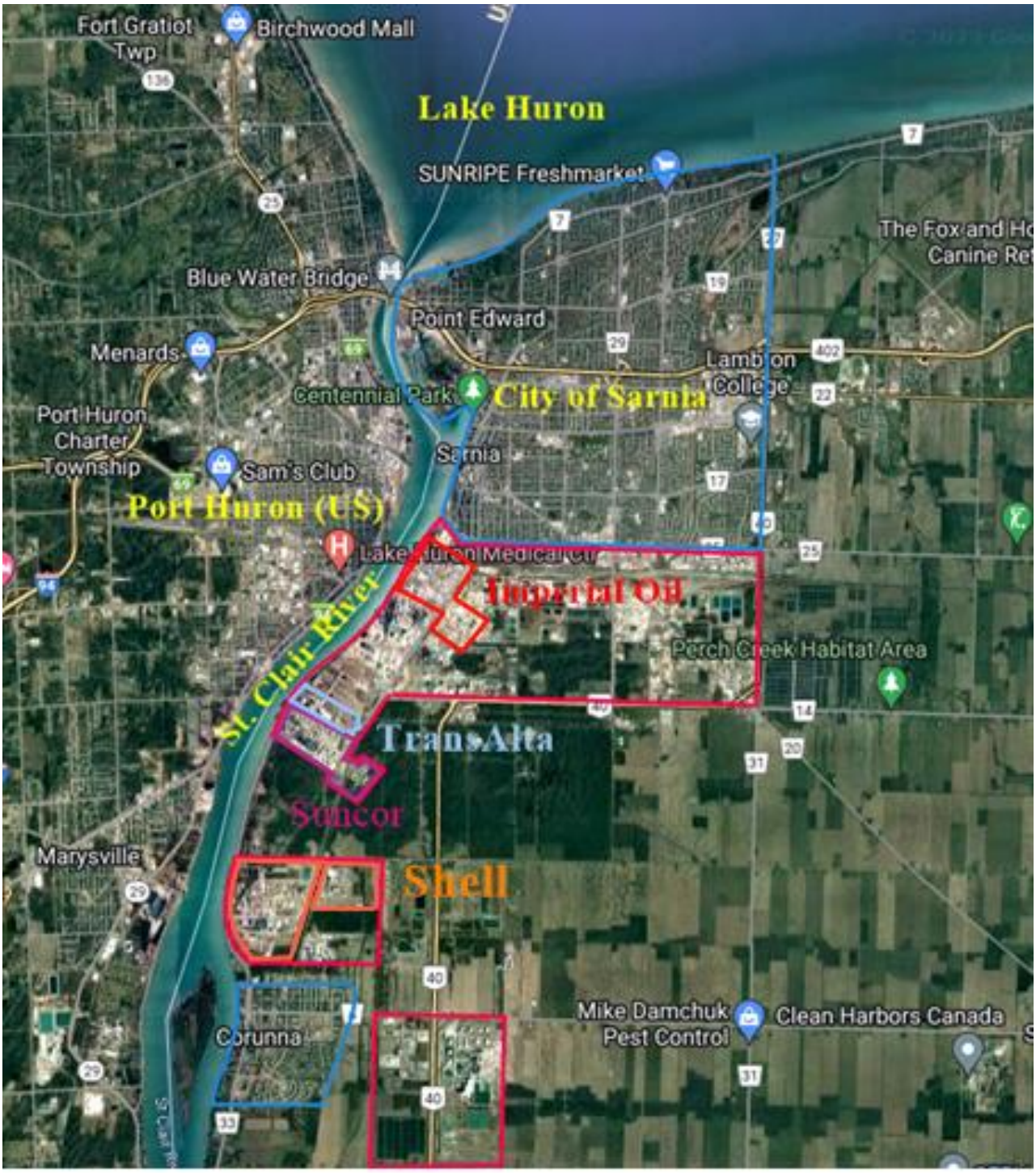

Figure 4.2: Map of Sarnia, residential areas are enclosed in blue line while red lines cover industrial complexes, including oil refineries and chemical plants. Major oil refineries and power plants that are suspected to produce methane are colored (Red: Imperial Oil, light blue: TransAlta Cogen Plant, Magenta: Suncor, Orange: Shell)

4.2. Methods

Measurements were conducted in and around the city of Sarnia (42.97 °N, 82.41 °W), located in southwestern Ontario, Canada, at the border with Port Huron, MI, USA. The full driving route can be seen in Appendix Figure C.1 and the routes are summarized in Table 4.1. They were aimed to capture CH_4 as well as SO_2 enhancements by travelling downwind of Sarnia, especially the 4 major refineries and power plants that were shown in Figure 4.2 (Imperial Oil, TransAlta, Suncor and Shell).

Table 4.1: Locations and measured time for each transects for each day.

July 21st		
Transect	**Measurement Time (EST)**	**Transect Road Name**
0	14:13 – 14:20	Highway 40
1	14:24 – 14:31	Indian Rd
2	13:52 – 14:08	Modeland Rd – Kimball Rd
3	14:40 – 15:07	Mandaumin Rd
4	15:15 – 15:44	Camlachie Rd - Marthaville Rd
5	15:59 – 16:27	Wanstead Rd
July 22nd		
Transect	**Measurement Time (EST)**	**Transect Road Name**
0	9:42 – 10:25	Vidal St – St Clair Pkwy
1	10:30 – 11:04	Highway 40 – Modeland Rd
2	11:07 – 11:48	Blackwell Sideroad – Waubuno Rd
3	11:56 – 12:22	Waterworks Rd
4	12:27 – 12:49	Camlachie Rd - Marthaville Rd

The measurements of methane were performed with the G2401 Picarro Cavity Ringdown Spectrometer (CRDS) mounted in a car. The instrument reported mole fractions of CH_4, CO, CO_2 and H_2O every 2 seconds with a precision of 2 ppb (methane); water-corrected dry mole

fractions of the species were used in the analysis. The inlet was mounted approximately 1 m above the ground on the passenger the side mirror, facing forward. The temporal offsets from the sampling tube and the time difference between instruments were measured at the start of the study and synchronized during the analysis. These time offsets of ~11 seconds were applied to the data set to synchronize the time and location of the vehicle.

The meteorological tower (Met tower) was set up at far downwind locations from the source by the Covenant Christian Church (42.979 °N, 82.163 °W) to measure wind speed and direction with 1 minute interval on both days. Additional hourly wind data and meteorological parameters were obtained from the government of Canada historical weather data from Sarnia station including the temperate and pressure used for the mass balance calculation. Ceilometer (Vaisala CL 51) based PBL height was obtained from two instruments set up in Windsor and Port Huron operated by Environment and Climate Change Canada (ECCC) and Northern Research Station (NRS) USDA Forest service respectively as part of the Michigan-Ontario Ozone Source Experiment (MOOSE) campaign. A model estimate of a boundary layer height was also obtained by the North American Regional Reanalysis Product (NCEP NARR). The surface Downwelling Shortwave Radiation (DSR) to calculate kinematic heat flux was obtained by the Advanced Baseline Imaginer (ABI) level 2 from GOES-16 satellite. The product provides pixel values of total shortwave irradiance received at the Earth's surface including effects from attenuation and scattering within the atmosphere.

The Hybrid Single-Particle Lagrangian Integrated Trajectory Model (HYSPLIT) by National Oceanic and Atmospheric Administration (NOAA) provides a computer model that estimates the air parcel trajectory by a Lagrangian approach of dispersion model an employing moving frame of reference for advection and diffusion calculation. Back trajectory analysis of observed plumes at downwind transects was employed to track the plume path and locate the potential sources of the enhancements.

Gaussian dispersion model was also used in this study to estimate source strengths. Gaussian dispersion model assumes that the dispersion of atmospheric species follows the normal statistical distribution. The simplified gaussian equation introduced in chapter 1 is employed:

$$C(x, y = 0, z = 0) = \frac{Q}{2\pi v \sigma_z \sigma_y} \quad (4.1)$$

where Q is the source rate, x is the downwind distance, v is the surface wind speed, and $\sigma_z \sigma_y$ corresponds to the vertical and lateral spread of the plume.

Gaussian fitting algorithm was developed in order to locate the plume and fit the data to the gaussian curve to identify the lateral plume spread, σ_y. Full plume width was defined as 6σ and 3σ value corresponding to half of plume width was employed to define lateral spread, $\sigma_y = 3\sigma$. The theoretical downwind distance from a source location to a peak enhancement was calculated from the size of the lateral spread (σ_y) given by 3σ of the plume from fitted curve:

$$downwind\ distance\ x, in\ km = \left(\frac{\sigma_y}{a}\right)^{\frac{1}{0.894}} \quad (4.2)$$

where a corresponds to the parameter from the Martin scheme (Appendix Table A.3.). Gaussian dispersion model assumes dispersion from a point source and the model may not provide an accurate estimate for area sources in Sarnia including industrial facilities and residential areas. An emission rate for an area source was estimated by assuming virtual point source extending beyond the location of an area source as depicted in Figure 4.3. A virtual point source assumption can produce a broad area of enhancement at downwind distance that can behave as an area source for further downwind transects. However, it should be noted that this approximation for an area source entails greater uncertainty for an emission estimate.

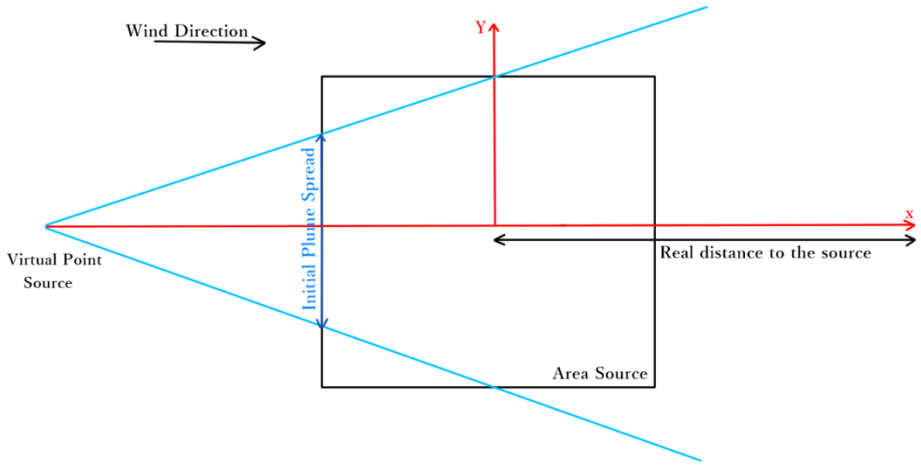

Figure 4.3: Diagram of a gaussian dispersion model for an area source

The mass balance approach was used to estimate the total emission of methane released across the whole city of Sarnia, including all industrialized sites and residential areas. As the measurements were performed on the surface by vehicle, the method requires the assumption of a well developed convective mixed layer (ML) in order for methane to achieve homogenous vertical profile at sufficiently far downwind transects. The downwind distance necessary to achieve this vertical homogeneity of methane in the boundary layer was calculated based on the atmospheric stability and convective velocity scale, w^* as daytime convection of atmosphere from surface heat flux dominates the plume mixing within the boundary layer. Based on the above assumptions, the total methane source rates across the downwind transect (s_1 to s_2) within the PBL (z = 0 to z = Z_{PBL}) can be found by:

$$Methane\ source\ rate = \int_{S1}^{S2}\int_{0}^{Z_{pbl}} X_{CH4}\frac{PMW_{CH4}}{RT} v_r \left(\frac{z}{Z_r}\right)^{\alpha} \cos(\theta)\, dSdZ \qquad (4.3)$$

where the integral calculates the flux of methane passing through the plane of width, S, and height of Z_{PBL} carried by the wind of speed v_r (assumed to be measured at height Z_r = 10 m above the ground) at an angle, θ. *T*he surface roughness coefficient, *a* used to estimate the vertical scaling wind profile. Pressure, P and temperature, T are assumed to be constant with height along with methane molecular weight, MW_{CH4} (16.0 $gmol^{-1}$) and gas constant, R (8.314 $Jmol^{-1}K^{-1}$).

4.3. Results and discussion

4.3.1. CH_4 measurement from July 21st

Mobile measurements were performed on 2 days field studies, July 21st and 22nd in order to increase statistical confidence in the results. Figure 4.4 shows CH_4 mixing ratios downwind of Sarnia on July 21st with each transects labelled in red. Transect 0 and 1 are considered together and called transect 01 throughout the discussion since Highway 40 had a curve in the middle of the transect that separated transect 0 and 1. Only the component of wind perpendicular to the transect is relevant in mass balance calculation and transect horizontal to the wind speed was excluded.

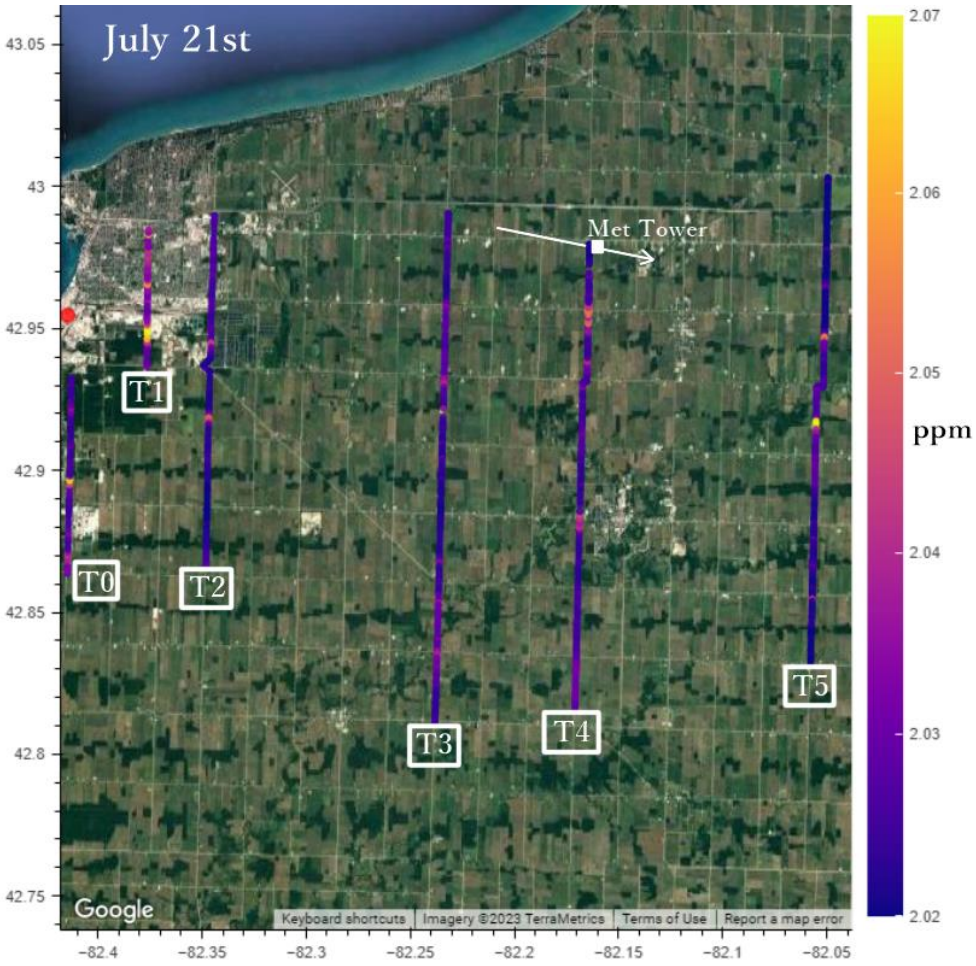

Figure 4.4: Map of each transect on July 21st. White square depicts the location of the Met Tower and white vector indicates the average direction of wind during the measurements.

Figure 4.5 shows the wind speed and direction data obtained from the Met tower, indicating a WNW wind direction predominantly, 283 ± 15 °, with wind speeds of 10.3 ± 3 ms^{-1}. The meteorological station data from Sarnia is shown in Table 4.2, with an average wind speed of 6.5 ± 1 ms^{-1} and average wind direction of 285 ± 20 °. The wind direction shows good agreement between the Met Tower and the Sarnia station, but the Met tower wind speed was slightly higher than the station data. Met tower wind speed was used in the mass balance calculation because further transects (T3 – T5) were used to estimate the average emission rate and the Met tower set up on T4 could provide a relevant local wind speed for these further transects. Downwelling shortwave radiation was obtained by the GOES-16 satellite at coordinate (42.875 °N, 82.375 °W) and summarized in Table 4.2 with an average of strong solar insolation of 870 ± 80

Wm^{-2}. According to Pasquill Stability classification, wind speed and solar insolation from the day is classified as neutral stability, C.

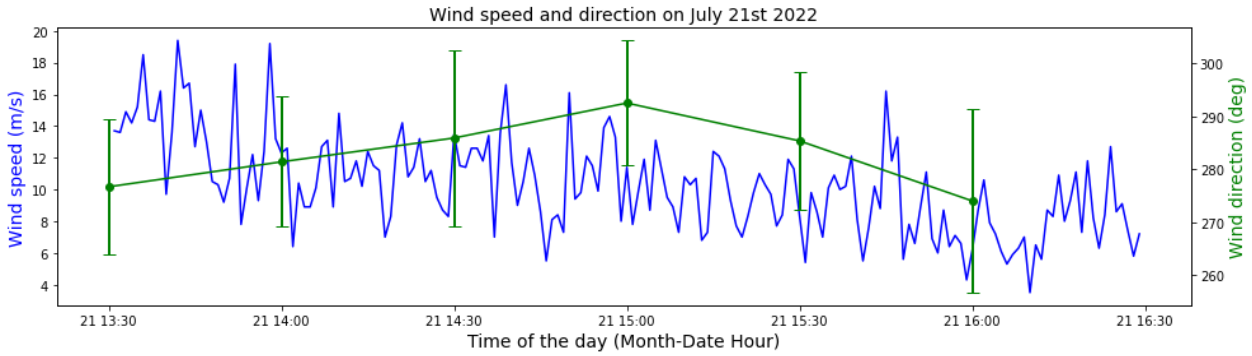

Figure 4.5: Wind speed and direction measured by the Met tower with time in EST. Wind speed is plotted with 1 minute data points while wind direction is plotted with 30-averages.

Table 4.2: Hourly Sarnia station meteorological data and downwelling solar radiation values obtained by GOES 16 satellite on July 21st.

Time (EST)	*Wind Speed (m/s)*	*Wind Direction (Degrees)*	*Temperature (°C)*	*Pressure (kPa)*	*Solar insolation (W/m^2)*
13:00	*6.7*	*270*	*29.6*	*98.37*	*902*
14:00	*7.8*	*290*	*29.6*	*98.36*	*951*
15:00	*6.7*	*310*	*30.8*	*98.39*	*900*
16:00	*4.7*	*270*	*30.5*	*98.41*	*743*
Average	*6.5 ± 1*	*285 ± 20*	*30.1 ± 0.5*	*98.38 ± 0.02*	*870 ± 80*

Figure 4.6 shows the back trajectories from methane peaks observed on transect 01 and 2 with potential methane sources highlighted in colors: Imperial oil (Red), Trans Alta Cogeneration Power Plant (Blue), Suncor Energy Refinery (Magenta), Shell Refinery and Chemical Plants

(Yellow), Nova Chemicals (Orange), and US sources, SEMCO energy and sewage treatment plant in (Light Blue).

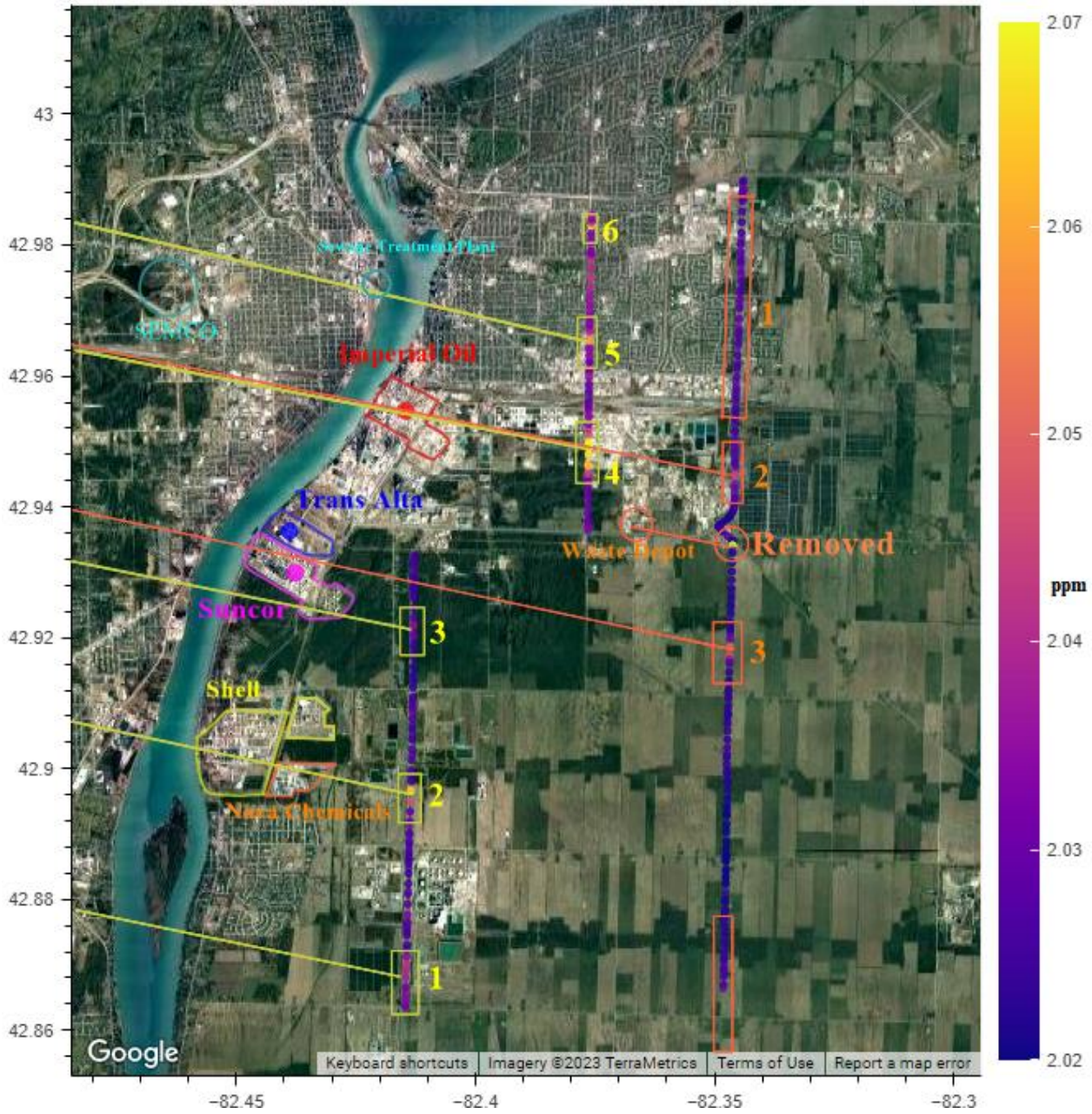

Figure 4.6: Map of transect 01 and 2 with potential sources in different colors. NOAA HYSPLIT back trajectories are drawn from the major peak locations at transect 01 (yellow) and transect 2 (orange).

Figures 4.7 and 4.8 show methane enhancements along transect, 01 and transect 2. Peaks identified by the curve fitting algorithm was labelled and corresponded to peaks highlighted in

Figure 4.6. Several sharp peaks are observed indicating close methane sources with multiple weak broad enhancements which may indicate sources further way in neighboring Michigan. Location of sources were identified using the HYSPLIT back trajectory and theoretical downwind distances were estimated based on lateral plume spreads (σ_y) which are summarized in Table 4.3 for transect 01 and Table 4.4 for transect 2. It should be noted that the peak fitting algorithm was not successful in fitting all enhancements to the gaussian function. For instance, peak 6 and other relatively small and broad enhancements were omitted as it is shown in Figure 4.7.

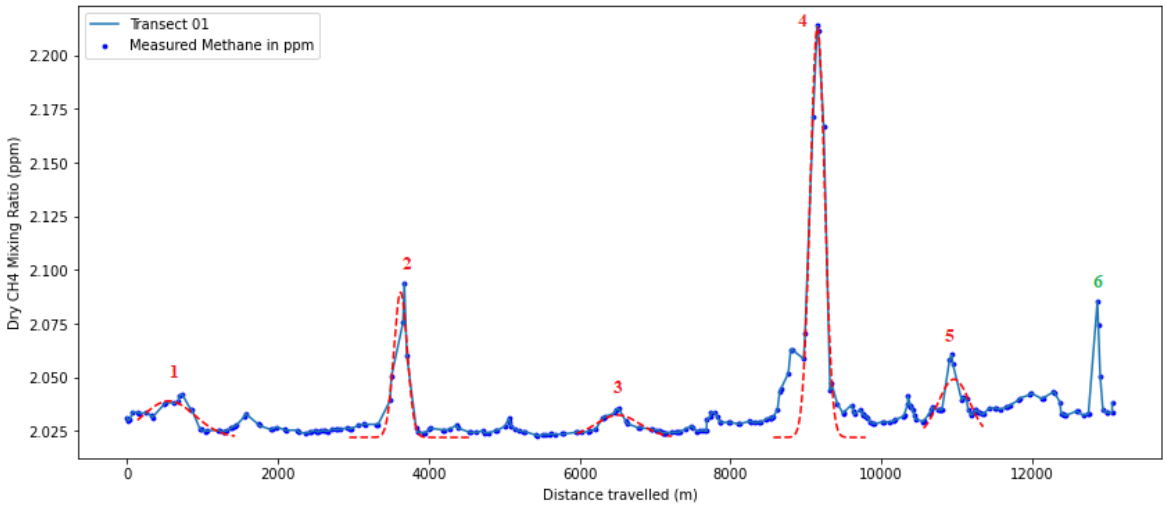

Figure 4.7: Dry mole fraction of methane measured along combined transect of 0 and 1 (transect 01). Enhancement patterns are characterized and fitted to gaussian curve by peak picking and fitting algorithm (peak 1 -5). Peak 6 was labelled in green as it was omitted by the algorithm but shows a clear enhancement.

Table 4.3: Summary of the standard deviations for curve fitted peaks by the algorithm on Transect 01 and estimated downwind distance to locate the sources based on 3σ for the plume lateral spread.

Transect 01 Peaks	*Centerline Location (m)*	*1 standard deviation of the peak, σ (m)*	*Estimated downwind distance from source (km)*
1	*553*	*341*	*12.9*
2	*3624*	*88*	*2.8*
3	*6506*	*291*	*10.8*
4	*9151*	*95*	*3.0*

5	*10962*	*208*	*7.4*

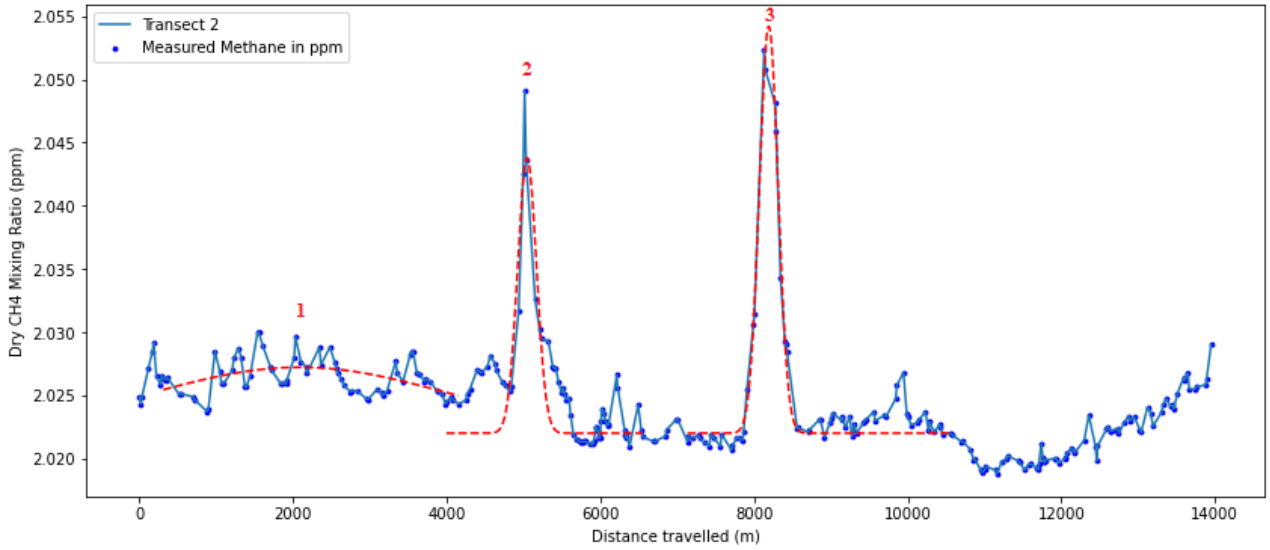

Figure 4.8: Dry mole fraction of methane measured along Transect 2. 1 broad curve and 2 sharp peaks are located.

Table 4.4: Summary of peaks on transect 2, standard deviation of the fitted curve (σ) and estimated distances from the source based on 3σ for the plume lateral spread.

Transect 2 Peaks	*Centerline Location (m)*	*1 Standard deviation of the peak, σ (m)*	*Estimated downwind distance from source (km)*
1	*2084*	*1947*	*90.5*
2	*5044*	*122*	*4.1*
3	*8190*	*122*	*4.1*

On transect 01, the maximum of peak 2 shows enhancement of 65 ppb above 2.025 ± 0.001 ppm background and the HYSPLIT back trajectory passes the Shell Canada refinery. The refinery is located approximately 2.9 km away from the location of the peak based on the map. The actual downwind distance approximately agreed to the estimated downwind distance of 2.8 km, based on the lateral plume spread of 3σ. Simplified gaussian equation was used to calculate the source rate, using the following parameters: $x = 2800\ m, v = 10.3\ m/s$, stability class C for $\sigma_x \sigma_y$ coefficients for the Martin Scheme. It was estimated that Shell Canada refinery emits 198 kg h^{-1} methane which is equivalent to 1730 annual tonnes of methane if the emission is consistent throughout the year.

The back trajectory from peak 3 aligns to the Suncor refinery facilities but shows weak and broad enhancement compared to other two sharp peaks, 2 and 4 which may indicate that the Suncor refinery is a relatively larger area source compared to Shell and Imperial oil refineries without apparent hotspots. Estimated distance to the source was 10.8 km which is much further away than the actual distance of 2.5 km from the map. The estimated distance corresponds to the location of the virtual point source if the Suncor facilities are assumed as an area source. Based om these assumptions, the estimation of the source rate yields 349 kg h^{-1} or 3059 annual tonnes of methane from Suncor refinery.

The back trajectory from peak 4 aligns with Imperial Oil refinery which is approximately 3.1 km from the peak and is akin to estimated downwind distance of 3.0 km. Peak 4 shows a sharp peak feature with an enhancement of 185 ppb. Using the same parameters as peak 2, with a different downwind distance of x = 3000 m for the distance between Imperial Oil and peak maximum, the source rate, Q is estimated to be 637 kg h^{-1} or 5580 tonnes methane per year. It is noted that peak 4 depicts an overlap of a weak and broad enhancement with the identified sharp peak. The weak and broad methane feature may represent to the area emission from the facilities while the sharp peak may imply that the refinery has a fugitive methane hotspot. As only an estimate was calculated for the sharp peak from this transect, the estimate value may not fully describe the whole facility scale emission. It is emphasized that the simple gaussian approach in this study should be considered as an approximate emission estimate for each identified source.

Between peak 4 to 6, widespread weak methane enhancements were observed which created an elevated methane level when the vehicle was travelling along northern part of the Sarnia. The back trajectories 5 and 6 do not align to any prominent methane source but the trajectories passes through the city's residential area. Elevated methane mixing ratio in urban environments are attributed to variety of anthropogenic sources including leaks from the natural gas infrastructure, and heating systems of buildings. Moreover, sharp characteristic of peak 6 may indicate a close local source such as the ships passing the St. Clair River since the unburned fuel from the consumption of liquified natural gas (LNG) in a ship's engine can be a considerable methane source. Another possible cause of elevated methane is from further away sources in U.S. from the state of Michigan. Based on U.S. EPA GHGRP, one major methane source in northern Port Huron is SEMCO Energy Gas Company (GHGRP ID: 1003026). The company majorly

distributes natural gas and was reported to emit 1367 tonnes of methane in 2021. The wastewater and sewage treatment facility just located along the St. Clair river could be another possible source which was shown to align with the back trajectory from peak 5.

On Transect 2, a sharp peak was removed prior to curve fitting which was identified to be the instantaneous emission observed from a local waste management service (Waste Depot at 456 McGregor side Rd) in alignment with the back trajectory. Peak 1 shows broad methane enhancement that aligns with the elevated level of methane observed along northern part of transect 01 which may be attributed to the city of Sarnia's residential methane emissions or possible further away U.S. sources. Peak 2 and 3 on Transect 2 show a sharp characteristic with estimated downwind distance of 4.1 km for both peaks. The back trajectory from peak 2 is in alignment with the Imperial oil refinery which is approximately 5.9 km away with observed maximum mixing ratio of 2.050 ppm. The discrepancy between the estimated distance to the actual distance from the map may arise from the inaccuracy of the simplified gaussian model for further downwind distances. The peak corresponds to enhancement of 35 ppb and using the real downwind distance of 5900 m, the source rate for the peak was estimated to be 409 kg h^{-1}. Assuming the enhancement is from the Imperial Oil predicted by the back trajectory, the estimated source rate is lower than the estimation from Transect 01, which was 637 kg h^{-1}. This may be due the temporal variability in methane emissions from the facilities depending on the operations performed throughout the day. It can also be due to the inaccuracy of the model as the simplified model fails to predict source rates from further downwind observations. Yet, the estimate from transect 2 can provide a meaningful comparison to the emission rate of Imperial Oil refinery estimated on transect 01.

Peak 3 back trajectory is depicted to pass through Suncor and TransAlta cogeneration plant facilities. Considering the sharp characteristic of peak 3, the source is presumed to be close with an estimated downwind distance of 4.1 km. Yet, the distance from the peak maximum to Suncor and TransAlta facilities are approximately 7.5 km. Employing 7.5 km as downwind distance with the enhancement of 36 ppb provides an emission rate of 648 kg h^{-1} which is much greater than the estimated rate from the Suncor refinery on transect 01. This may be due to the combined emissions from the Suncor refinery and the TransAlta facilities.

Figures 4.9, 4.10 and 4.11 depict the enhancement observed along transect 3, 4 and 5 respectively. It is noted that for further transects, it is difficult to identify clear peaks or enhancement features due to nearby interferences from local methane sources and irregular spread of plumes by topography.

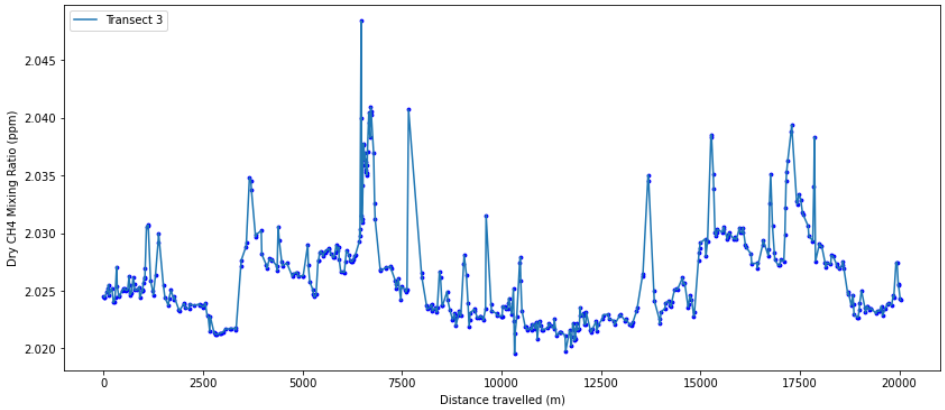

Figure 4.9: Dry mole fraction of methane measured along Transect 3

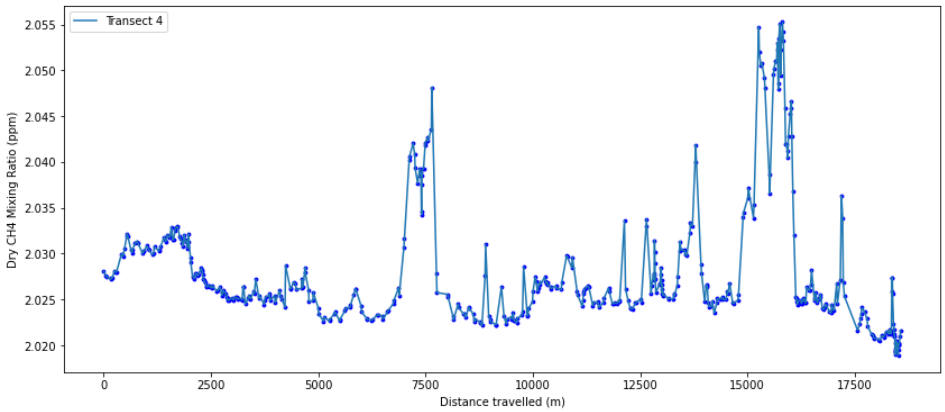

Figure 4.10: Dry mole fraction of methane measured along Transect 4

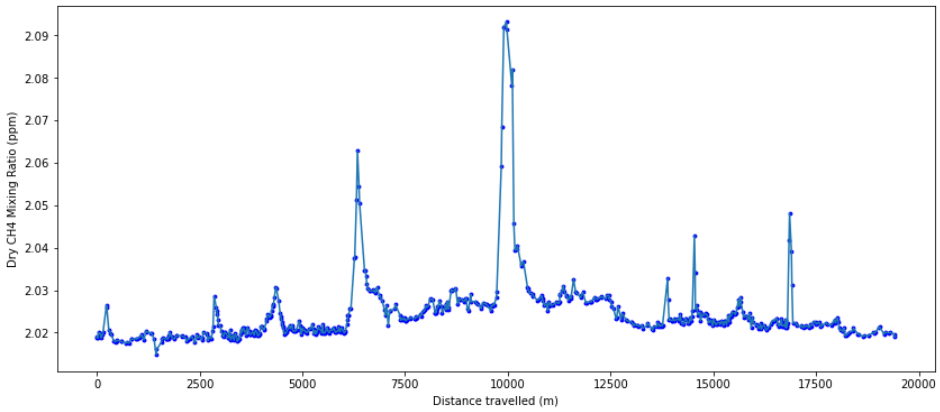

Figure 4.11: Dry mole fraction of methane measured along Transect 5.

The farther transect 3 to 5 showed several sharp enhancement patterns that imply nearby methane sources, most likely farms, as several cow and horse farms were observed during the measurement. The location of currently active farms and stables as well as waste management service (Clean Harbor Canada) is shown on Figure 4.12.

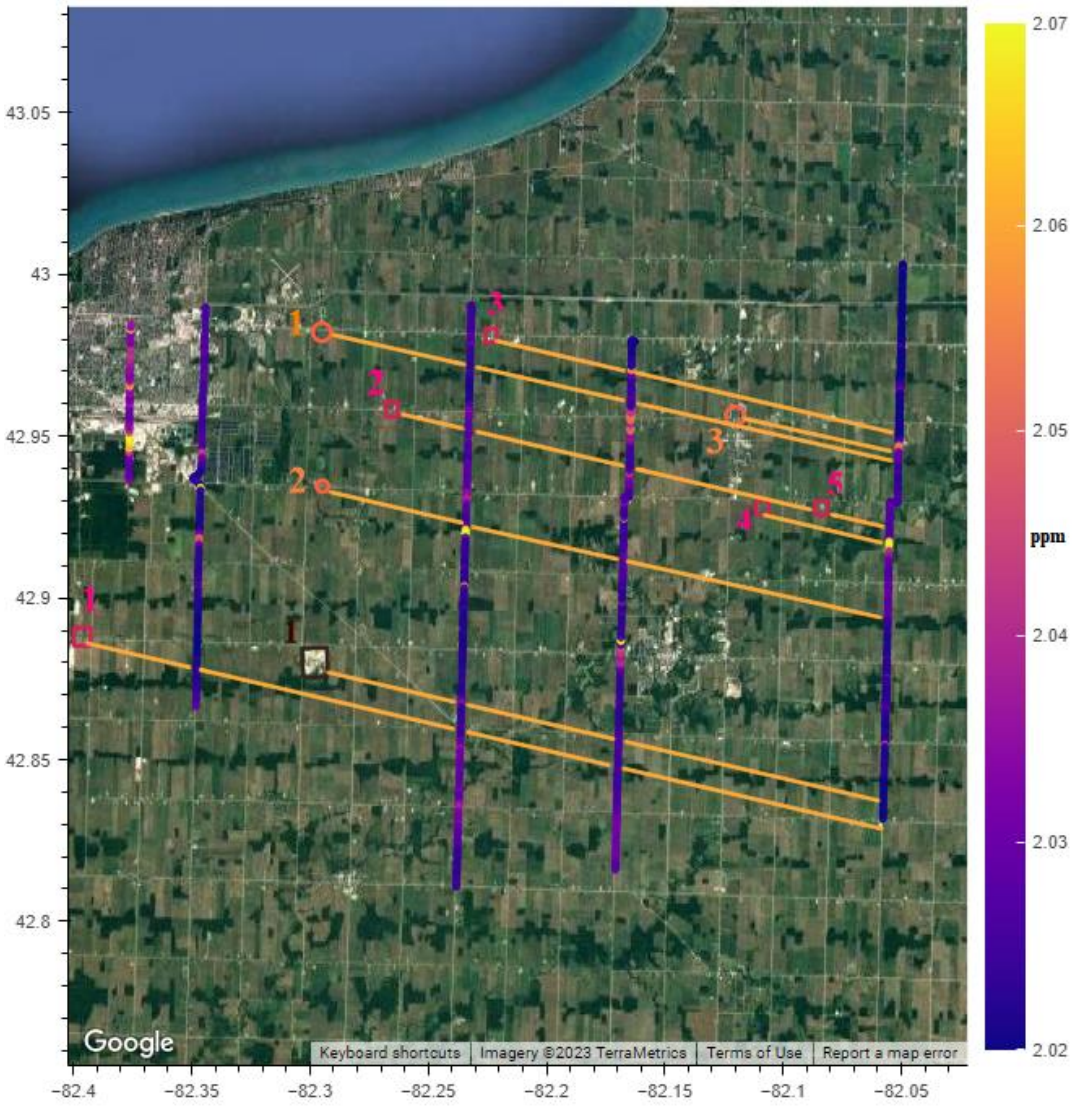

Figure 4.12: Transect map with farms, stables and waste management services located to identify their effect on enhancements. Orange lines indicate the forward trajectory from the potential sources. Farms are depicted by magenta squares. Stables are represented by orange circle and waste management by brown square. The list of farms and stables are named on Table 4.5.

Table 4.5: List of farms, stables and waste management corresponding to figure 4.12.

FARMS		**STABLES**	
1	Wilson Farm	1	Peter Core Stables
2	Fairwind Farm	2	Elite Stables
3	Char Creek Farm (Kettle Farm)	3	Dukeries Arabian Horse Farm
4	Blazing Acres Farm	**Waste Management**	
5	Konzelmann Farm	1	Clean Harbors Canada

Transect 5 especially shows several sharp peaks with very narrow plume spread of less than 150 m which indicates close local sources. The maximum observed on transect 5 was 2.09 ppm which is much greater than transect 3 (2.05 ppm) and transect 4 (2.06 ppm). Relatively high methane enhancements from local sources can skew the result for mass balance calculation as farther transects (T3 – T5) are used for the estimation. The maximum enhancement on transect 5 is assumed to be from Blazing Acres Farm (Farm 4) aligning to the highest enhancement observed on the transect as well as Duckeries Arabian Horse Farm (Stable 3). These local peaks with sharp features identified based on Figure 4.12 were removed for T3 – T5 for mass balance quantification. Figure 4.13 shows transect 5 enhancements after major local peaks were removed.

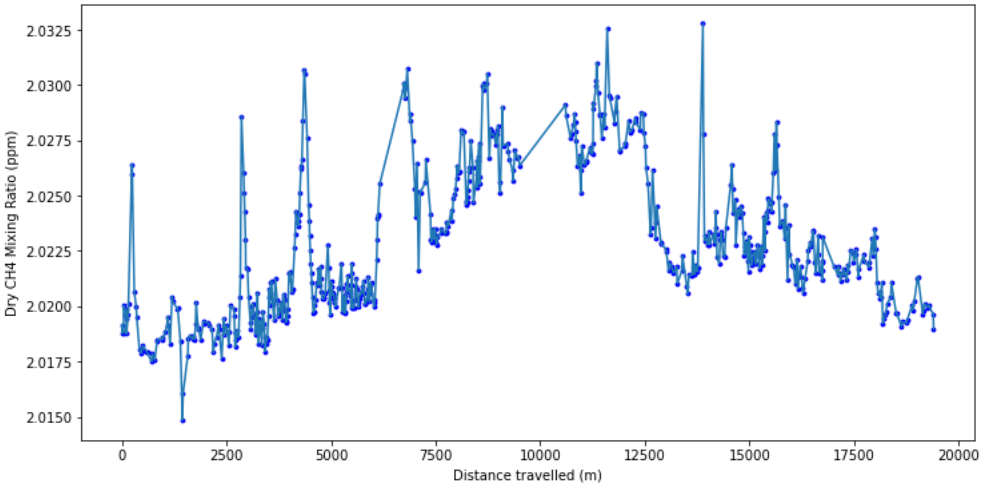

Figure 4.13*:* Transect 5 methane enhancements along the transect after removing peaks from local sources.

As carbon monoxide can be used for a tracer of vehicle exhaust, the correlation plot of CH_4 against CO at each transect was used to discern interferences from passing vehicles. Moreoever, the correlation was used to identify potential CO emissions from industrial facilities. Plots of CO against the transect distance travelled are plotted in Figure 4.14 for close transects (T1-T2) and Figure 4.15 for further transects (T3-T5).

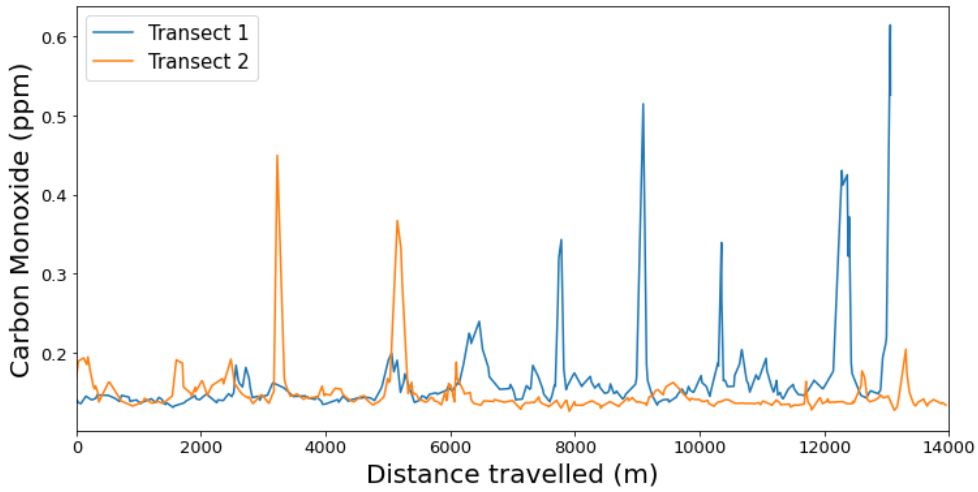

Figure 4.14: CO plot against the transect distance travelled for the first two transects.

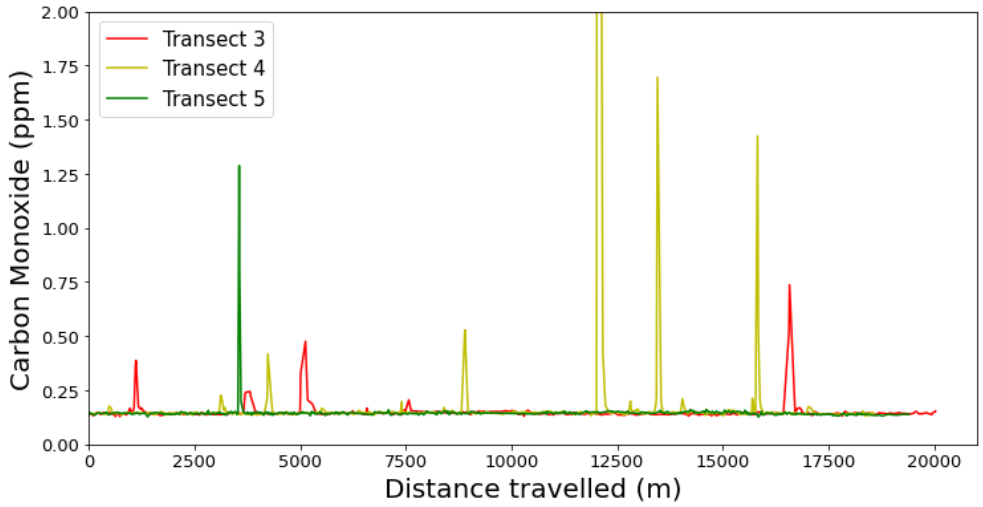

Figure 4.15: CO plot against the transect distance travelled for the transect 3 – 5 used for mass balance. The y axis is limited at 2 ppm to visualize smaller enhancement better. Transect 4 has a sharp peak at 4.24 ppm that is cut off.

The CO enhancement along the first transect shows multiple sharp peaks and weak enhancements that are as broad as several thousand meters. These weak and broad enhancements

are likely from refineries and chemical plants that utilize hydrocarbon fuels including liquified natural gas and crude oil. Along with methane, carbon monoxide is emitted as a by-product of the combustion of natrual gas and crude oil, especially from an incomplete combustion. Correlation plots in Figures 4.16 and 4.17 show statistically significant correlation of CH_4 with CO from P value < 0.01 which is most likely due to the weak CO emission from industrial facilites. Yet, low R^2 value indicate the variability in CO cannot be explained linearly to the enhancement in CH_4.

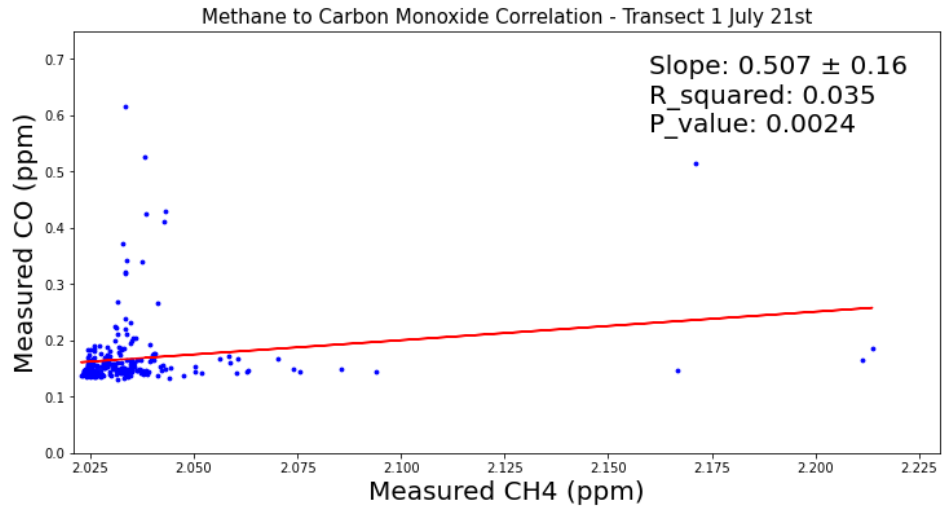

Figure 4.16: Methane to carbon monoxide correlation plot for transect 01.

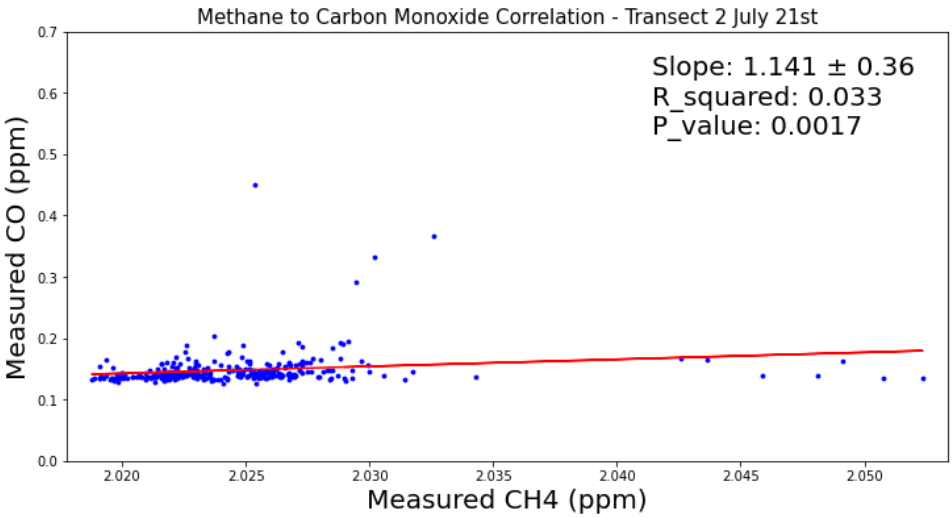

Figure 4.17: Methane to carbon monoxide correlation plot for transect 2.

Further downwind transects (T3 – T5) in Figure 4.15 only depict sharp peaks without broad enhancements which indicate a vehicle emission is the main source for CO peaks. Although it is known that natural gas vehicles (NGVs) using diesel and gasoline produce CH_4, a study by Nam et al. (2004) showed that the CH_4 emission from vehicle is very low. These are shown in the correlation plots for T3-T5 in Figures 4.18, 4.19 and 4.20 by relatively high P value > 0.01 and low R^2, indicating no correlation between the CH_4 and CO enhancements. The CO from industrial facilities for further transects are spread out enough that the CO level reached to a background. Therefore, it is concluded that the effect from the passing vehicles for T3-T5 are negligible.

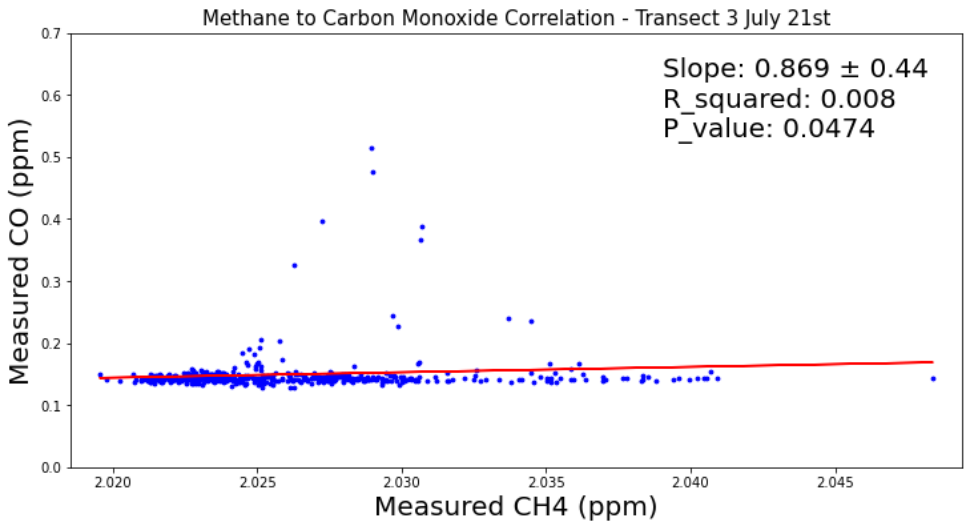

Figure 4.18: Methane to carbon monoxide correlation plot for transect 3.

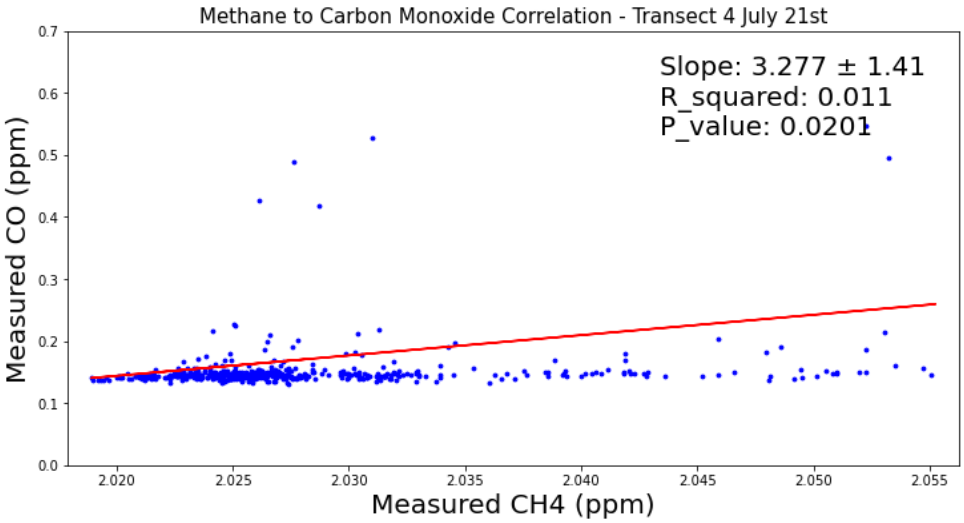

Figure 4.19: Methane to carbon monoxide correlation plot for transect 4.

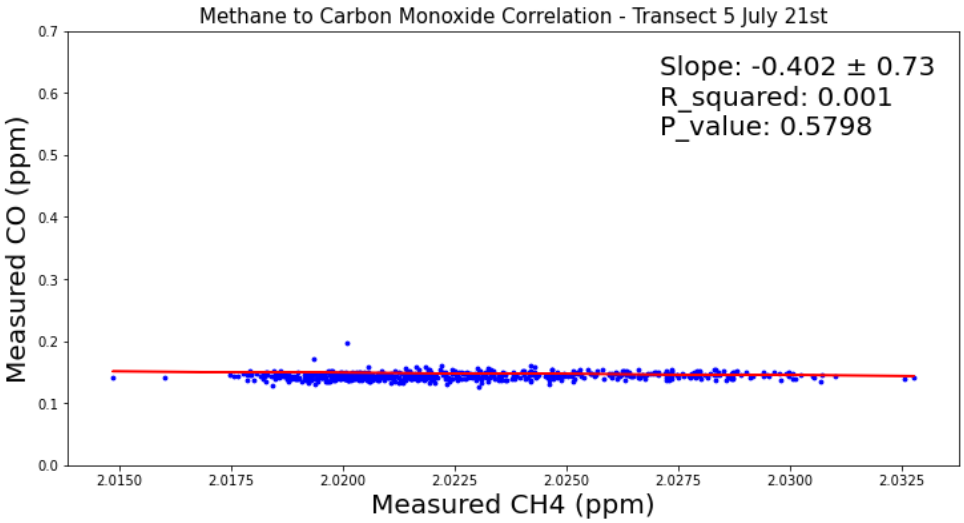

Figure 4.20: Methane to carbon monoxide correlation plot for transect 5.

The ceilometer data from Windsor was a 15-minute average experimental PBL height developed by an ECCC algorithm using a 1D gaussian filter and minimum gradient method, while the hourly averaged Port Huron PBL height is estimated by a Vaisala proprietary algorithm. The two ceilometers were spatially separated by a distance of ~ 90 km, with the Port Huron ceilometer being closer to the measurement domain. Figure 4.21 shows the time series plot for the development of boundary layer during measurement period. Additional model boundary layer height was obtained by the NCEP NARR. NARR employs NCEP Eta Model (Numerical weather forecast model) along with surface and rawinsonde observations to generate

32km resolution field of boundary layer heights. Summary of the boundary layer data including NCEP boundary layer height is presented on Table 4.6.

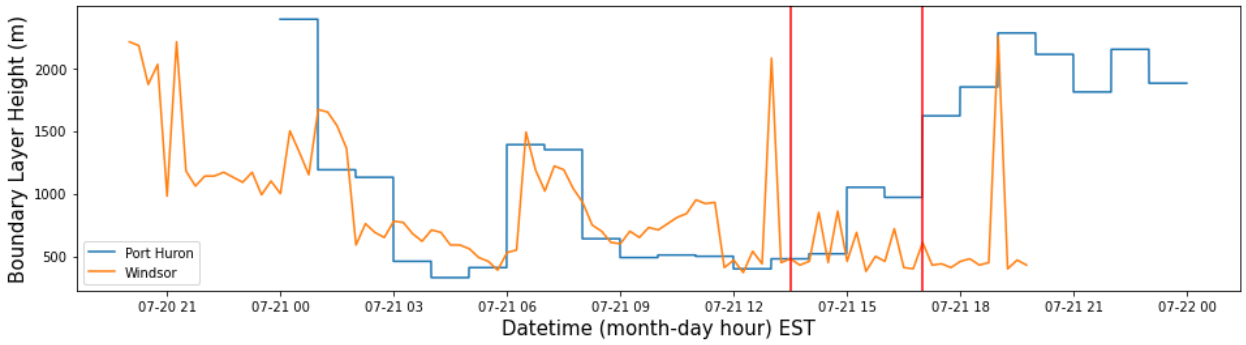

Figure 4.21: Time series of PBL height for each ceilometer, Blue: Port Huron and orange: Windsor. Two red line indicates the start and end time of the measurement on July 21.

Table 4.6: Summary of the boundary layer heights for July 21st during measurement period

Time (EST)	*Boundary Layer Height (Port Huron) (m)*	*Boundary Layer Height (Windsor) (meters)*	*Boundary Layer Height (NCEP) (meters)*
13:30	480	455 ± 50	1100 ± 440
14:00	520	655 ± 200	
15:00	1050	508 ± 110	
16:00	970	498 ± 130	
Average	750 ± 257	529 ± 67	1100 ± 440
Overall		790 ± 170	

The average of the three-boundary layer height was 790 ± 170 m on July 21st during the measurement period. The calculation of kinematic parameters and mixing time are presented in Appendix C1 which outputs well mixed distance of 9.3 km based on this result, only the last 3 transects were averaged for the rates estimated by the mass balance approach. Figure 4.22 illustrates the methane rates estimated on each transect.

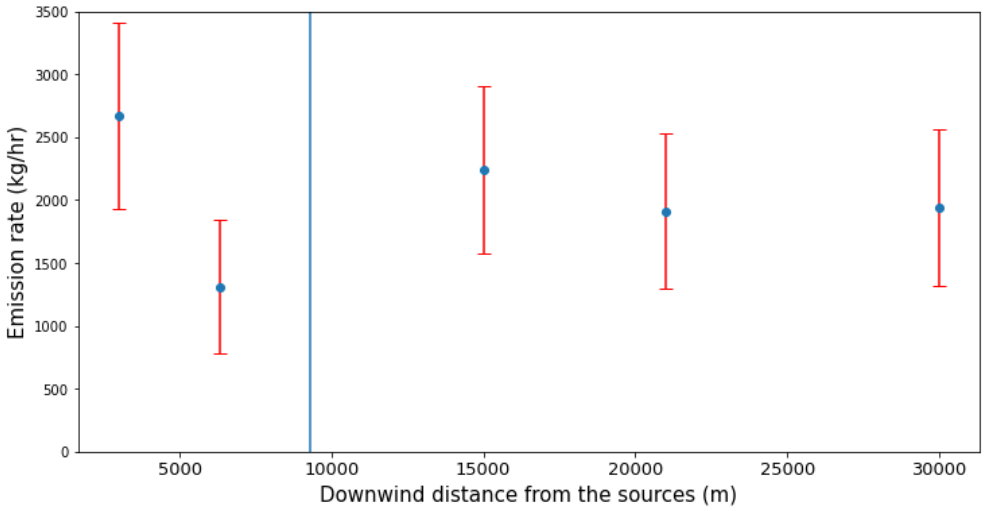

Figure 4.22: Estimates of methane emissions calculated by mass balance method per transect. The average emission estimate is based on the last 3 transects and blue line indicates the well mixed distance to assume homogenous vertical profile of methane.

Since the measurement involved estimation of emission rates for the city including industrial facilities and residential areas instead of a single point source, it was difficult to identify a point to calculate downwind distances for multiple sources. Since refineries, especially the Imperial Oil, present as a predominant methane source, the mid point of Imperial Oil and Sarnia refinery was employed as a coordinate to calculate the downwind distance for each enhancement. It should also be noted that Transect 01 and 2 values are not true emission rates as they are not sufficiently far from the source. The estimated emission rate based on the transects that are sufficiently far enough downwind is 2090 ± 640 kg h^{-1}. Since the total lateral distance travelled for T3-T5 were much greater than T1 and T2, they represent a true estimate of methane from the city of Sarnia including all industrial sources.

4.3.2. CH_4 measurements from July 22nd

The transect map with observed mixing ratios is presented in Figure 4.23 with the meteorological data from the MET tower in figure 4.24. During the measurement period between 9:30 AM EST to 13:00 PM EST, the average wind speed was measured to be 7.1 ± 3.5 ms^{-1} with the wind direction of 283 ± 24 °. The station weather data from Sarnia in Table 4.7 shows a wind direction of 285 ± 5 ° while local wind speed was higher compared to the station wind speed of 4.03 ± 1.5 ms^{-1}. Similar to day 1, the MET tower data for wind speed and direction was used in the mass balance calculation.

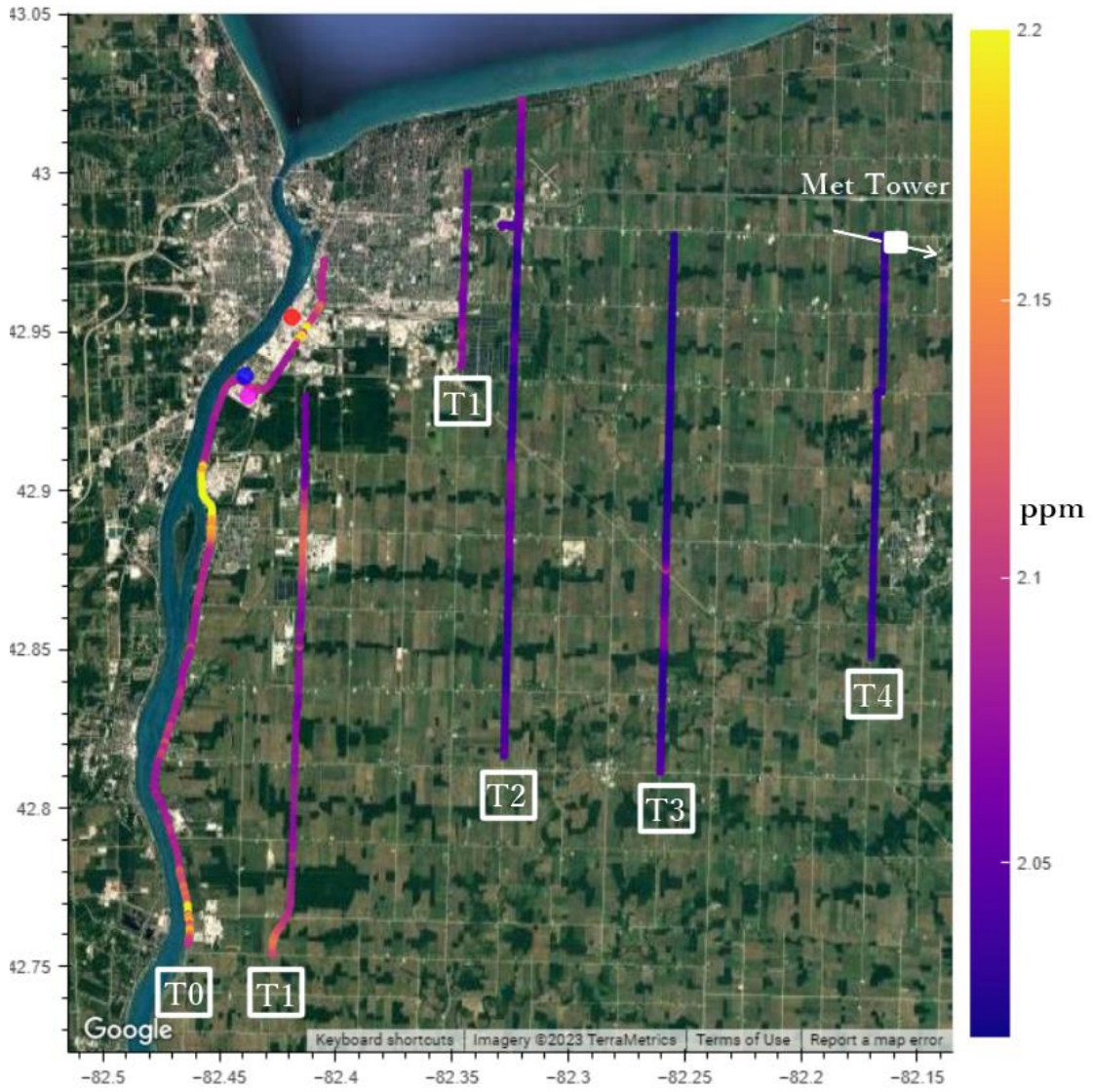

Figure 4.23: Map of each transect on July 22nd. White square indicates the location of Met Tower set up at Covenant Christian Church with wind direction indicated by the white arrow.

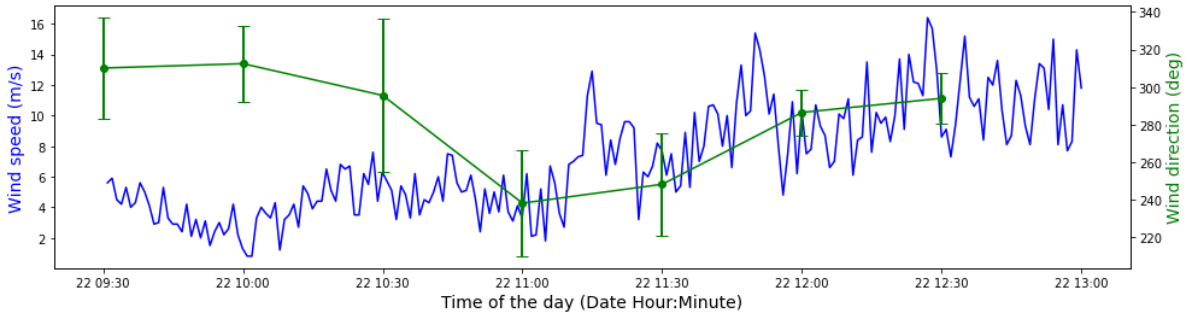

Figure 4.24: Time series plot of windspeed and direction measured by Met tower, on July 22nd, 2022. Wind speed is plotted by 1-minute average while wind direction is plotted by 30-min average.

Table 4.7: Station (Sarnia) meteorological data on July 22nd

Time (July 22nd)	*Wind speed (m/s)*	*Wind Direction (degrees)*	*Temperature (°C)*	*Pressure (kPa)*
9:00 – 10:00	*3.06*	*290*	*25*	*98.95*
10:00 – 11:00	*2.22*	*280*	*28*	*98.99*
11:00 – 12:00	*4.72*	*280*	*28.9*	*99.02*
12:00 – 13:00	*6.11*	*290*	*29.6*	*99.04*
Average	*4.03 ± 1.5*	*285 ± 5*	*27.9 ± 1.8*	*99.00 ± 0.03*

Measurements along the road on Ontario-Michigan border by the St. Clair River was performed as an upwind transect in order to identify background methane and any enhancements from sources in U.S. The methane mixing ratio along transect 0 is shown in Figure 4.25. Estimated downwind distance from the sources was calculated for each enhancement based on the lateral plume spread, σ_y from the gaussian curve fitting and presented in Table 4.8.

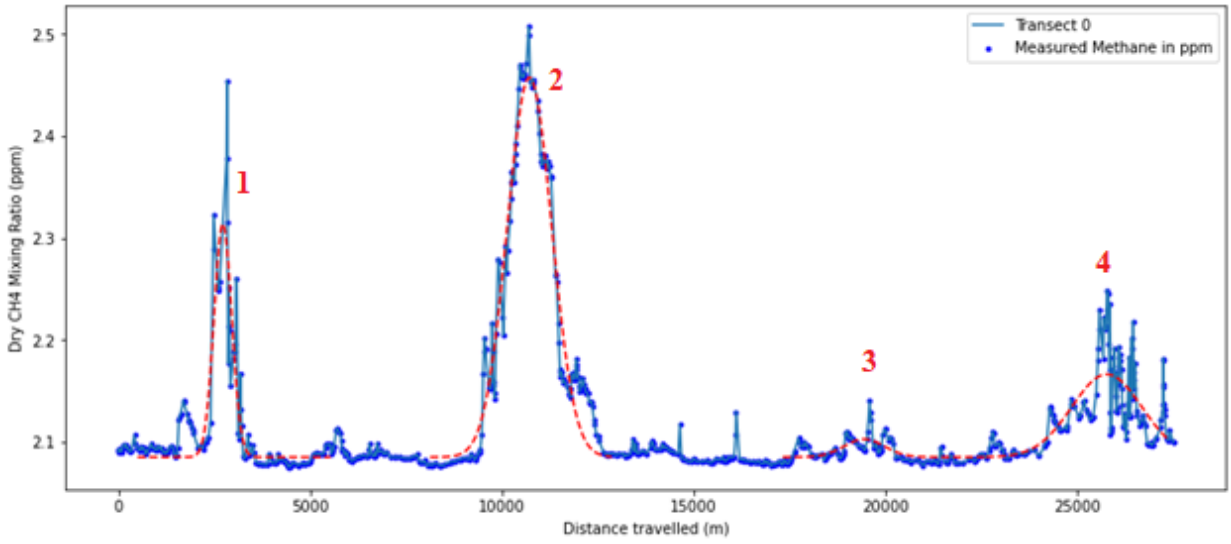

Figure 4.25: July 22nd dry mole fraction of methane measured along Transect 0 with 4 identified peaks.

Table 4.8: Summary of identified enhancements on Transect 0 on July 22nd. Downwind distance from sources and methane source rate are estimated by simplified gaussian model.

Transect 0 Peaks	*Centerline Location (m)*	*Peak Standard Deviation, σ (m)*	*Enhancement (ppb)*	*Estimated downwind distance (km)*	*Estimated source rate (kg/h)*
1	*2744*	*229*	*350*	*8.26*	*972*
2	*10727*	*582*	*370*	*23.5*	*4703*
3	*19334*	*526*	*55*	*21.0*	*594*
4	*25761*	*913*	*164*	*38.8*	*4284*

It is noted that the curve fitting algorithm was not efficient for transects 1 to 4 due to overlaps of peaks and local interferences. Only T0 data was used to calculate source rates of upwind sources based on the dispersion model. T1 to T4 enhancement plots along the lateral distance travelled are shown Figure 4.26 to Figure 4.29.

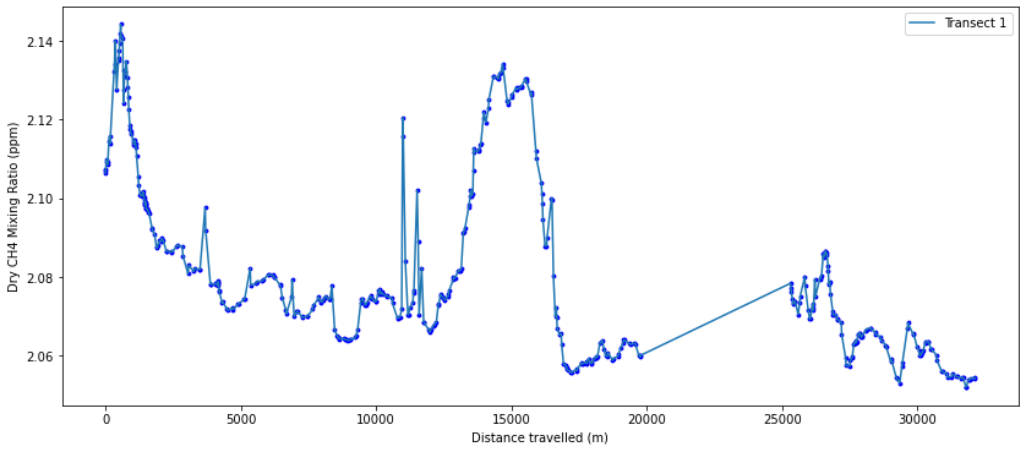

Figure 4.26: July 22nd Transect 1 dry mole fraction of methane.

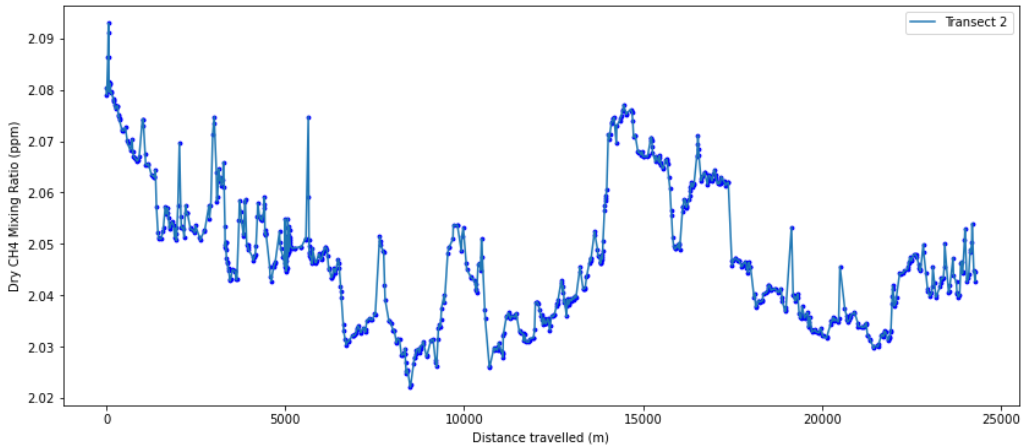

Figure 4.27: July 22nd Transect 2 dry mole fraction of methane.

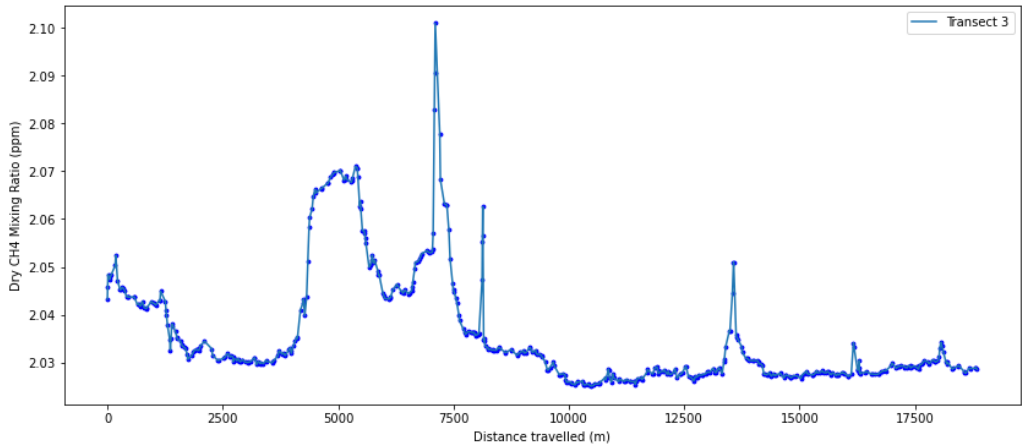

Figure 4.28: July 22nd Transect 3 dry mole fraction of methane.

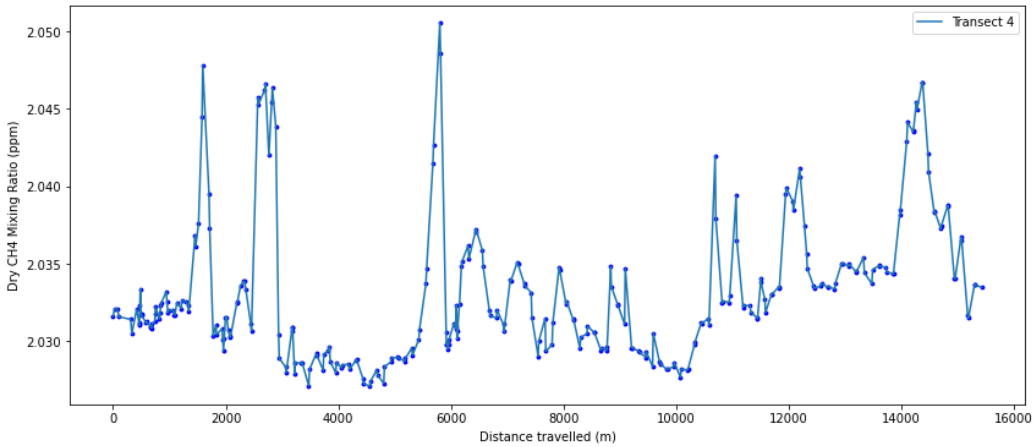

Figure 4.29: July 22nd Transect 4 dry mole fraction of methane.

Figure 4.30 visualizes relatively high ambient CH_4 mixing ratios observed along transect 0 and 1 that were elevated above typical background level of ~ 2.0 ppm. Background on the upwind transect (T0) was 2.087 ± 0.006 ppm. This evidently shows methane emissions originated from Michigan state, most likely from far away distance. In order to identify the sources for the enhancements, forward trajectories were depicted from the prominent methane sources in the area as shown in Figure 4.30.

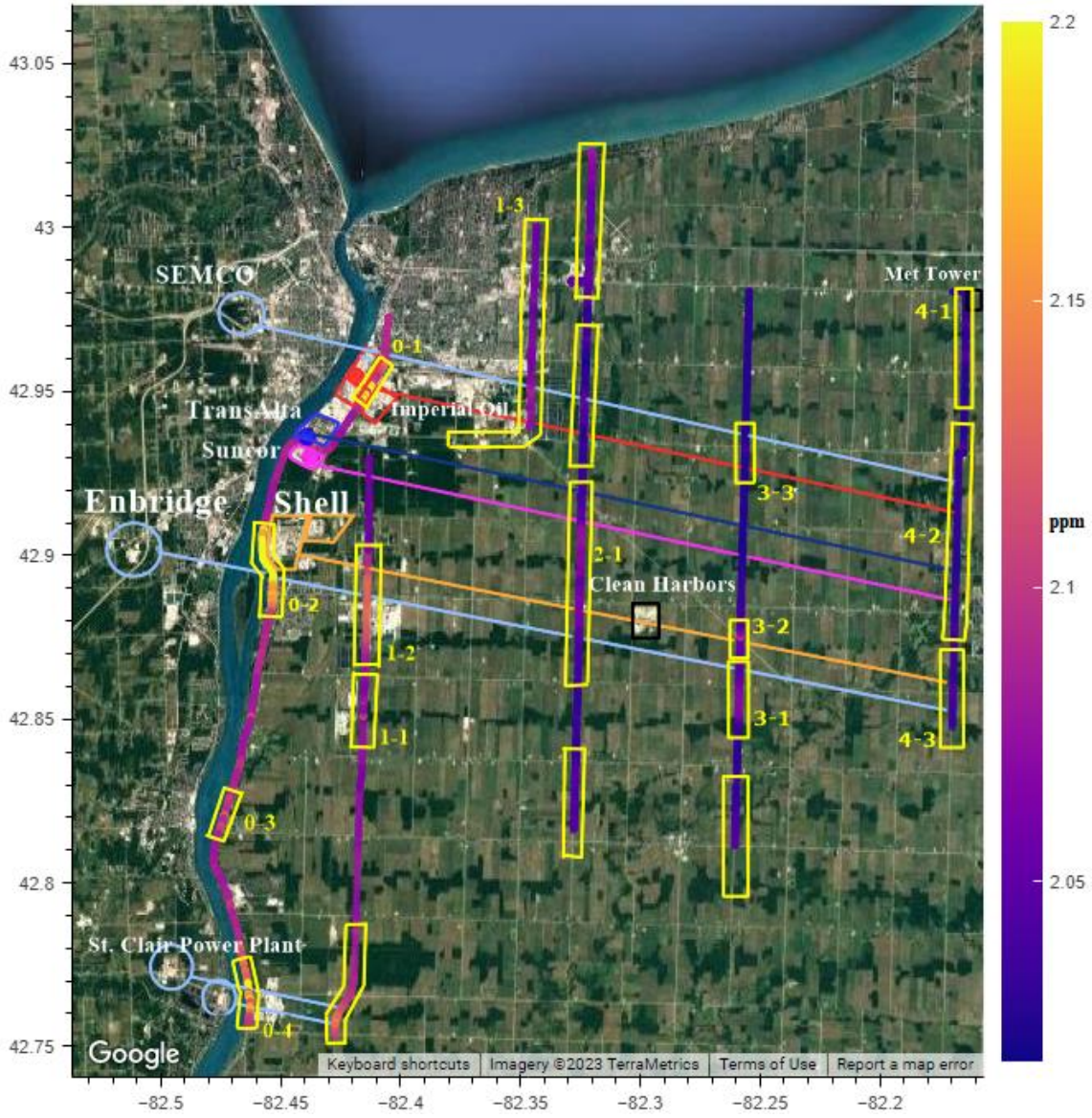

Figure 4.30: Forward trajectory map from potential sources (Red: Imperial Oil, Blue: TransAlta, Magenta: Suncor, Orange: Shell, Light blue: US sources such as SEMCO Energy, Enbridge, and St. Clair Power plants) Broad enhancement trends observed at each transect was highlighted in yellow box.

Due to the limitation of the road, northern part of transect 0 travels downwind of the major industrial facilities of Sarnia, including Imperial Oil refinery along Vidal street. Enhancement 0-1 aligns to Imperial Oil indicated by a sharp peak within a broader methane enhancement, similar to the characteristics of peaks observed from day 1 measurement. Assuming the Imperial Oil facilities form an area source, the estimated emission rate corresponds to 972 kg h^{-1} based on the virtual point source distance of 8.72 km. This estimated rate is slightly higher than the day 1 emission rate of 637 kg h^{-1} (from T01). As the peak was observed during daytime around 9:47 AM, it can be due to a difference in operations performed throughout the day. Moreover, considering the broader plume width observed on day 2 transect, the estimate from day 2 peaks likely involve other nearby sources such as Imperial Oil's chemical plants which are located in close proximity to the refinery.

The major methane enhancement on Transect 0, peak 0-2, is unequivocally a source in the USA, likely from the Enbridge Marysville Pump Station 187 (256 Murphy Dr St. Clair, MI). When the forward trajectory is drawn from the station, the plume from the station passes through the observed major enhancements at all downwind transects on T0 – T4. The peak 0-4 also aligns to the St. Clair power plants on T0 and T1. It is noted that the estimated source distances calculated by gaussian dispersion implies much farther way sources for each peak, 23.5 km for peak 0-2 and 38.8 km for peak 0-4. This is likely due to the source not truly being a point source but a source with a larger initial lateral spread as they present as broad area sources.

Higher elevated levels of methane observed along upwind transect, T0 may also be due to the fugitive leaks from transportation pipelines and natural gas infrastructure in Michigan state. Michigan state is known to carry natural gas and oils through complex system of pipelines, with over 59,000 miles of distribution pipelines which enters Michigan from Ohio, Indiana, and Wisconsin. The National Pipeline Mapping System (NPMS) shows transmission pipeline to visualize gas and liquified natural gas (LNG) transmissions as in Figure 4.31. Michigan, especially have several fugitive methane leaks from liquified natural gas (LNG) transmission pipelines. Similarly in Ontario, the methane leaks from transportation pipelines and distribution facilities (Enbridge) presents to be the top 3 major methane emitters for the oil and natural gas sector.

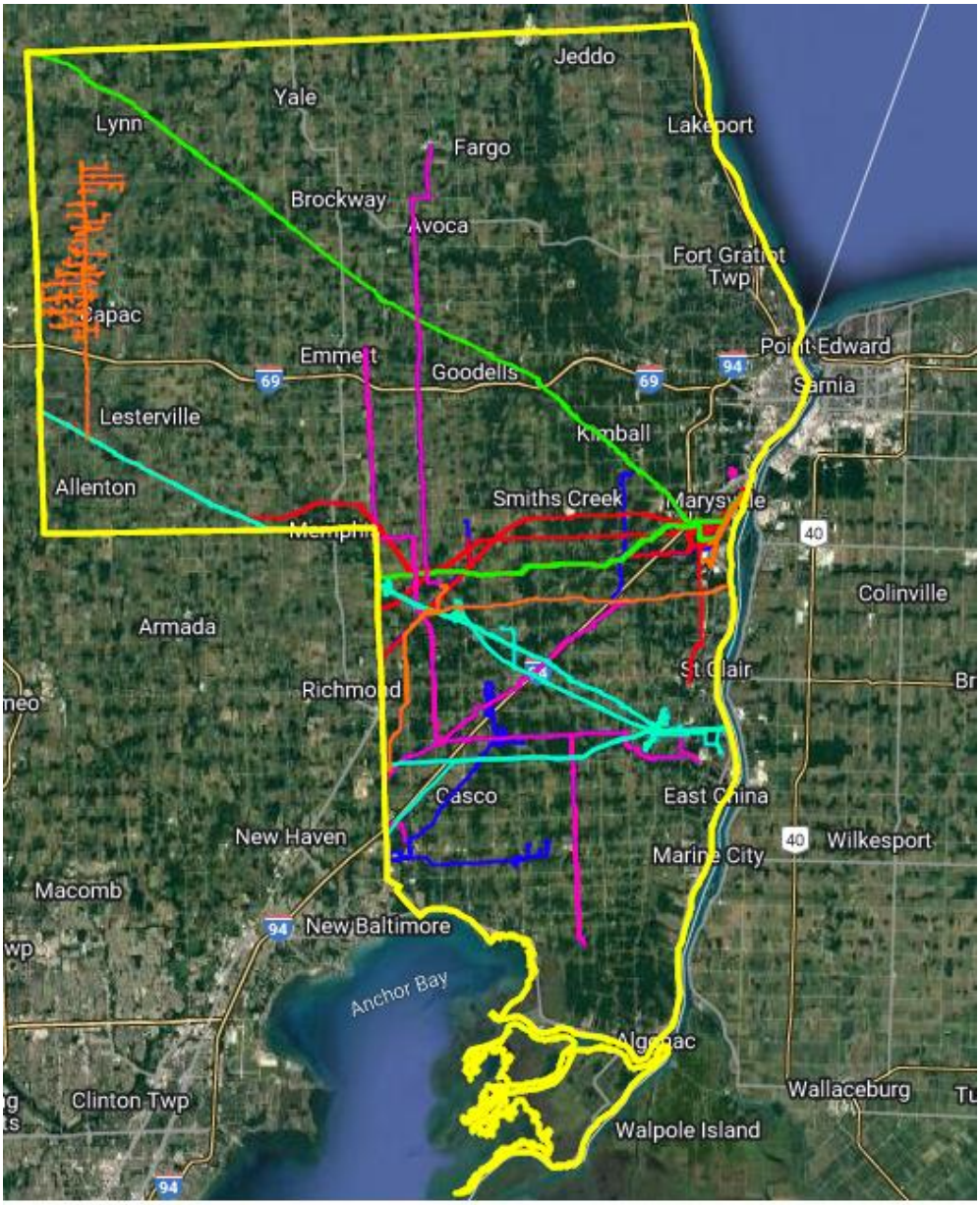

Figure 4.31: Pipeline map showing only currently active pipelines: Blue (all gas pipelines), Red (all liquid pipelines including liquified natural gas). Company related pipelines are specified by: Green (Enbridge Energy – line 5), Magenta (Semco Energy), Cyan (Great lake gas transmission – GLGT, Vector pipeline, and DTE gas company), and Orange (Nova Chemicals and ANR pipelines) Yellow line indicates the boarder of St.Clair county. (US department of transportation)

Two major pipelines that carry natural gas from northwest of Port Huron are Enbridge line 5 and SEMCO Energy's pipelines that extends from North to South. The SEMCO pipelines located northern area of Port Huron also match to the broader enhancement that caused elevated methane along north of measurement transects on both day 1 and day 2. Enbridge line 5 carries

natural gas to Marysville where the gas is delivered to Enbridge station near St. Clair river, storage facilities and Marysville Hydrocarbons LLC which were two major potential sources identified in figure 4.30. Based on the day 2 observation, this Enbridge pipeline and distribution facility near St. Clair river is suspected to be a considerable methane emitter. Line 5 pipeline is the most important pipeline for western Canada as well since it majorly carries the natural gas from US to Canada, connecting to the Enbridge facility in Sarnia. Then, the natural gas is further carried along line 7 and line 9 from Sarnia to Westover and Montreal.

Since the enhancements from the US were very broad and caused elevated background values on all transects downwind of Sarnia, effects of US sources could not be eliminated, and they were integrated together with methane emissions from Sarnia. Therefore, it was expected for day 2 emission rate to be greater than day 1. As the measurement started during morning, the boundary layer was still developing throughout the measurements. Therefore, each transect was assigned with corresponding meteorological condition instead of using averaged values for overall measurement period. Figure 4.32 demonstrates this development of boundary layer through the day. It is noted that the PBL data from Port Huron increased drastically between 10 to 11 AM (EST) as well as the NCEP NARR data between 11 to 12 pm. Table 4.9 summarizes the boundary layer heights along with the downwelling solar radiation value obtained by GOES-16 satellite.

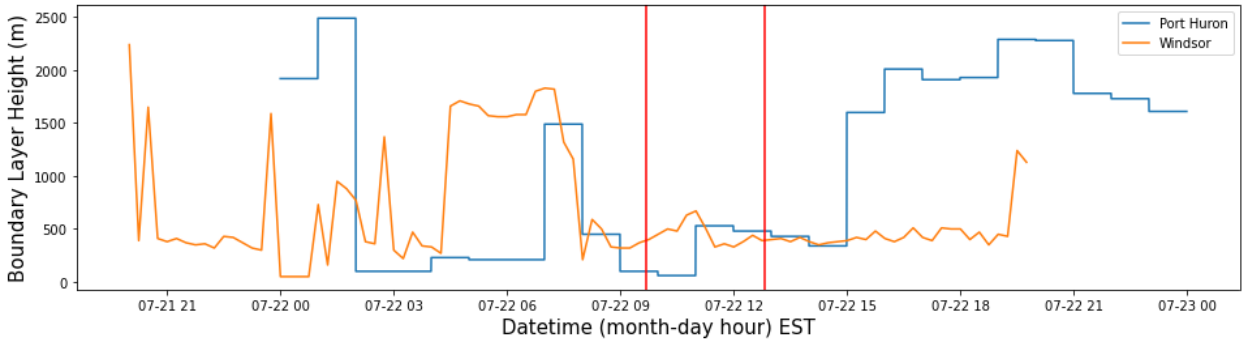

Figure 4.32: Time series of PBL height for each ceilometer, Blue: Port Huron and orange: Windsor. Two red lines indicate the start and end time of the measurements on July 22nd.

Table 4.9: Summary of boundary layer height data on July 22nd

Time (EST)	*Boundary Layer Height (Port Huron) (m)*	*Boundary Layer Height (Windsor) (m)*	*Boundary Layer Height (NCEP) ± 40% (m)*	*Downwelling solar radiation (W/m^2)*
9:00 – 10:00	*100*	*353 ± 68*	*350 ± 140*	*421*
10:00 – 11:00	*60*	*515 ± 138*	*350 ± 140*	*583*
11:00 – 12:00	*530*	*468 ± 270*	*1000 ± 400*	*695*
12:00 – 13:00	*480*	*385 ± 78*	*1000 ± 400*	*737*

Appendix C.1 provides a summary of kinematics parameters used to calculate the mixing time at each transect which shows that the mixing time increases as the boundary layer develops from morning till noon. The summary of combined meteorological parameters are presented on Table 4.10 for each transect used in the mass balance calculation. The furthest distance calculated is 8800 m and the data points beyond this distance were averaged as shown in figure 4.33 which includes transect 2 – 4.

Table 4.10: Summary of combined meteorological data assigned to each transect in order to consider the changing boundary layer condition.

Transect	*Measurement Time (EST)*	*Wind speed (m/s)*	*Wind Direction (degrees)*	*Boundary Layer Height (m)*	*Downwelling solar radiation (W/m^2)*
0	*9:42 – 10:25*	*3.5 ± 1.5*	*315 ± 24*	*380 ± 40*	*502 ± 160*
1	*10:30 – 11:04*	*4.7 ± 1.4*	*291 ± 43*	*310 ± 70*	*583*
2	*11:07 – 11:48*	*8.0 ± 2.4*	*239 ± 24*	*670 ± 160*	*695*
3	*11:56 – 12:22*	*9.2 ± 1.9*	*285 ± 15*	*620 ± 140*	*737*
4	*12:27 – 12:49*	*10.8 ± 2.3*	*290 ± 14*	*620 ± 140*	*737*

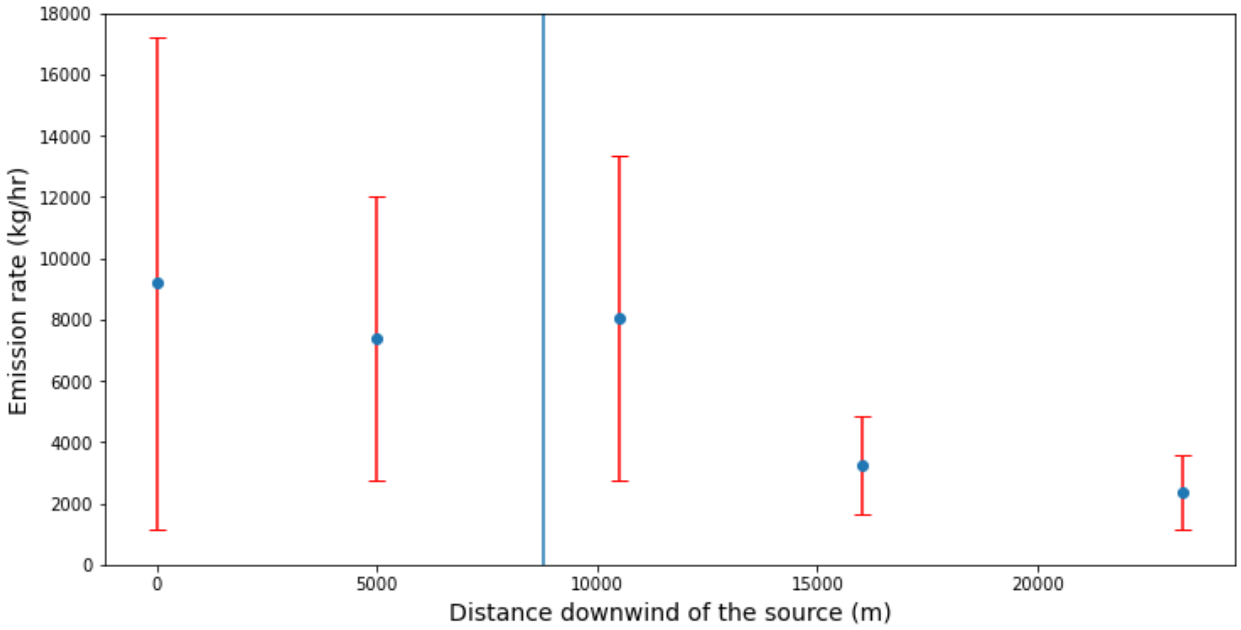

Figure 4.33: Estimates of methane emissions calculated by mass balance method at each transect. Blue line indicates well mixing distance at 8800 m. Transects 2,3 and 4 beyond the blue line are valid to for emission estimates.

Transect 0 was assumed to be "on" the source with downwind distance of 0 m. For other downwind transects, distance was calculated from the St. Clair parkway (the street for transect 0). Based on the calculated well mixed distance, average of last 3 data points provide emission rate of 4560 ± 2700 kg h^{-1}. However, strong influences of US sources on the data should be considered, which is visible for the first 3 transect from the estimated emission rate. There is a drastic drop is emission rate between T3 to T4, from 8053 ± 5300 kg h^{-1} to 3257 ± 1600 kg h^{-1}. To provide an estimate with the least effect from US enhancements, the average of the last 2 data points give estimate of 2810 ± 930 kg h^{-1}.

4.3.3. Discussion

These close transect measurements confirmed that major sources of methane from the industrial complexes were Imperial Oil refinery, Shell Canada refinery and Suncor refinery/TransAlta power plants as expected, with Gaussian modelling used to compute methane source rates summarized in Table 4.11. Annual emissions are calculated based on the assumption that the emissions do not have temporal variability, which is not accurate as refineries and power plants show strong temporal variation depending on facility operations (Lavoie et al., 2017). Yet, the estimated annual emission can be an approximate emission rates to be compared to the GHGRP values. Table 4.12 summarizes the day 1 and day 2 methane emission rate quantified by the mass balance method across the city of Sarnia, including all industrial facilities and residential areas.

Table 4.11: Summary of facility methane emissions estimated by the gaussian model.

Estimated Source	*Methane emission rate (kg h^{-1})*	*Annual Emission (tonnes)*
Imperial Oil Refinery (day 1 – T 01)	*637*	*5580*
Imperial Oil Refinery (day 1 – T2)	*409*	*3583*
Imperial Oil Refinery (day 2)	*972*	*8515*
Average Imperial Oil	*672 ± 230*	*5890 ± 2010*
Shell Canada Refinery (day 1 – T01)	*198*	*1730*
Suncor Refinery (day 1 – T01)	*349*	*3059*
Suncor and TransAlta Combined emission (day 1 – T2)	*648*	*5676*

Table 4.12: Summary of methane emission rate by mass balance method

	Methane emission rate (kg h^{-1})	*Annual emission rate (kilotons)*
Day 1 (21st July)	2090 ± 640	18.3 ± 5.6
Day 2 (22nd July)	2810 ± 930	25 ± 8
Average	2450 ± 560	21.5 ± 4.9

The day 2 emission estimate of 2810 ± 930 kg h^{-1} is higher than the day 1 estimate value of 2090 ± 640 kg h^{-1} due to a strong influence from the US methane sources. The comparison plot in Figure 4.34 shows good agreement emission rates calculated from each day within the uncertainty except the third point on day 2 which was excluded in the estimation of mass balance. The average value is shown to converge to 2450 ± 560 kg h^{-1}.

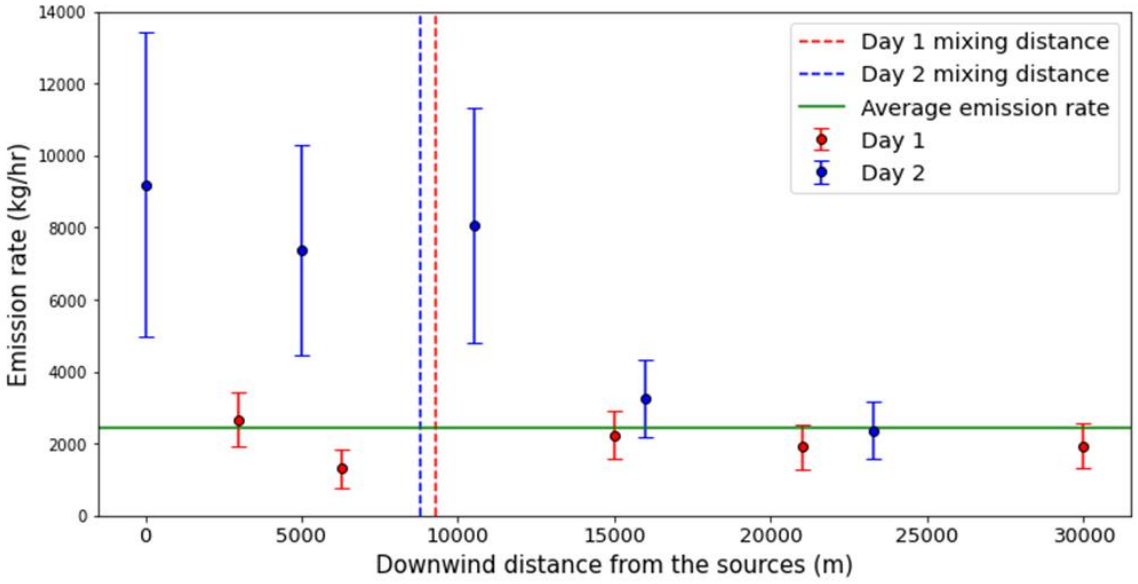

Figure 4.34: Comparison of the emission rates calculated for day 1 and day 2 by mass balance method depicting converging emission rate to the average emission rate of 2450 kg h^{-1} shown by a green horizontal line.

As there were emissions from US sources included in the total mass balance quantification on day 2, day 1 estimate value should be considered as a more accurate representation of Sarnia's total methane emission. The hourly methane emission rate from each day can be extrapolated to average annual methane emission rate of 21.5 ± 4.9 kt assuming no seasonal variability in the emissions. Based on 48 kt emission from the oil and natural gas sector reported by the National Inventory for Ontario, the methane emissions from city of Sarnia is expected to account for 45% of the methane emissions from the province's oil and natural gas sector. The rest of 55% of oil and natural gas emissions in Ontario are attributed to three other sources. According to GHGRP, the largest methane emitting facility was the Enbridge Gas distribution in North York, ON with reported value of 16.6 kt of methane from the facility with its transportation pipelines near the facility reported to emit fugitive methane leaks of 5.7 kt. Second largest methane emitter in the

sector was TransCanada Pipeline in Kenora, ON with reported value of 6.2 kt methane. The sum of these three sources account for 28.5 kt or ~60% of the Inventory estimate.

From the transect 01, gaussian modelling estimates provided imperial oil refinery emission, 672 kg h^{-1}, Suncor Refinery, 349 kg h^{-1} and shell refinery emission, 198 kg h^{-1}. The sum of these three facilities emissions corresponds to 1219 kg h^{-1} which is 50% of the emission estimated by the mass balance method. The GHGRP values are significantly lower than the estimates calculated by the gaussian models for each facility. Estimated annual emission rate of 5890 tonnes per year from Imperial Oil is 10 times greater than the GHGRP value of Imperial Oil refinery of 534 tonnes in 2020. Sarnia Refinery was reported to emit 82 tonnes of methane in 2020. Compared to 3059 tonnes estimated by gaussian model, the estimate is 37 times greater. However, it should be noted that as Suncor facilities are in close contact with TransAlta power plants, and the source was assumed to be an area source. It was possible that the observed broad emission was combined emissions of Sarnia refineries and TransAlta power plants. GHGRP combined methane emissions for both facilities were 342 tonnes (Suncor with TransAlta), implying the estimated value of 3059 tonnes is 9 times greater. This factor of 9 – 10 times difference with the GHGRP values coincides with the discrepancy observed in Greenlane field studies in Chapter 3.

4.4. Conclusion

Chapter 4 presents a successful result of the use of the mobile mass balance method to identify and quantify methane emissions from oil and gas facilities in the industrial sites of Sarnia based on two different field studies on July 21st and 22nd, 2022. Ground mobile measurements conducted by a cavity ringdown spectrometer mounted in a vehicle provided sufficient resolution of data to identify and characterize the methane plumes at downwind transects.

Even though the mass balance method can provide a convenient alternative to identify total methane emissions, it is also important to characterize emissions of each facility, especially for oil and gas infrastructures where the super emitters can account for a disproportionate amount of methane emissions. This is done by employing Gaussian dispersion modelling and HYSPLIT back trajectories to attribute methane plumes to their sources from the close transect measurement (T01 on July 21st and T0 on 22nd). From day 1, close transect measurement identified 3 main sources from Sarnia, Imperial Oil, Suncor, and Shell refineries, with respective

source rates of 637 kg h^{-1}, 349 kg h^{-1}, and 198 kg h^{-1}. Estimation from transect 2 provided slightly lower estimate for Imperial Oil of 409 kg h^{-1} with an average emission estimate of 523 ± 110 kg h^{-1} for Imperial from Day 1. Day 2 measurement along Vidal St. showed a higher estimate of 972 kg h^{-1}. This resulted in the average Imperial Oil refinery emission rate of 672 ± 230 kg h^{-1} from both days. The observed discrepancies between emission rates could be due to the temporal fluctuation in methane emissions from refineries, depending on different operations performed. For instance, cold venting could have caused higher methane emission. Further measurements at different time of the day, or long-term observations by a satellite observation are required to provide further insight to identify these potential intermittent emissions. It is also worth noting that the simplified gaussian model used in the study may not accurately depict the emissions from based on the enhancements on further transects and estimating emissions from area sources. Correlation analysis between CH_4 to CO from day 1 showed that industrial facilities emit low amount of CO with CH_4 which caused broad enhancements on close transects. However, the levels quickly fell to the background for further transects and identified vehicle exhausts showed to have nominal effect on the observed methane enhancements. Further analysis of CH_4 with CO_2 enhancements could access if the methane emission was originating from combustion or non-combustion related operations.

Upwind, Transect 0 measurement on day 2 highlighted several US sources. US sources were likely to be fugitive gas leaks from vast natural gas pipelines in the Michigan state. Suspected methane sources include SEMCO pipelines that carries liquified natural gas from northern Port Huron to south along Marysville which is suspected to cause elevated methane levels along northern part of transects close to the city of Sarnia on both days. Enbridge line 5 and their storage facilities near St. Clair river are also suspected sources of methane. Due to the widespread enhancement of methane that could not be separated from the emissions from Sarnia, the quantified emissions rates included enhancements from U.S sources. The total emission rate from Sarnia estimated by mass balance was 2090 ± 640 kg h^{-1} from day 1 and 2810 ± 930 kg h^{-1} from day 2 with the average emission of the two days study to be 2450 ± 560 kg h^{-1}. This emission rates are equivalent to 21.5 ± 4.9 kt annual methane emission close to 45% of the methane emissions in the Ontario's natural gas and oil sector. Since Sarnia account for close to half of the sector emission, regulating methane emissions from the refineries especially Imperial Oil, can greatly help curb methane emissions in order to meet Canada's 2030 goals of reducing

the GHGs emission by 40% from 2005 levels. The study showed that mass balance technique can provide convenient method to quantify overall methane from a large area and the method can benefit further from incorporating with local dispersion modelling to characterize plumes and satellite imageries to identify long term temporal variation.

Chapter 5: Conclusions and Future Work

In this thesis, the results of mobile measurements of atmospheric methane employing cavity ringdown spectrometer are presented from multiple field studies with mass balance quantification of emission rates. Methane emission from oil and gas production and waste management present a challenge to curbing anthropogenic methane emissions. The quantification of methane from these sources by top-down techniques has been the subject of much recent research. The mobile mass balance method presented in this study demonstrated that it is applicable for both the surveillance of methane from a small point source such as a landfill site and for the measurement of broader area sources such as multiple facilities and city scale methane emissions.

Mobile measurement of methane had high spatial resolution that could fully capture the characteristics of methane plumes at downwind transects. The 4 different field studies performed at Greenlane landfill during 2021 – 2022 showed that the major methane emission from the landfill was a hotspot in nature. The observed peaks fitted well to the expected gaussian curve, especially for closer transects where the interference from other local sources and topographic effects were minimal. The use of a simplified gaussian model was successful in demonstrating that the method was viable to characterize and quantify individual plumes which would have been difficult based on mass balance quantification alone. In order to further confirm that the plumes originated from a landfill, other tracers from landfills can be measured simultaneously such as hydrogen sulfide (H_2S) or non-methane organic compounds (NMOCs) other gases that are produced from the breakdown of organic materials in the landfills. The estimated average emission rate from the Greenlane landfill by the gaussian dispersion model was 3320 ± 250 kg h^{-1} which agreed well with the mass balance estimate of 3300 ± 730 kg h^{-1}. The quantified methane rates showed that the methane emissions had low seasonal variability as the results were consistent between studies performed at different times of the year. Comparison of meteorological parameters highlighted that the surface temperature and boundary layer height had the most effect on the observed methane enhancement at downwind locations. High boundary layer height along with strong surface heat flux was shown to dilute methane within the boundary layer quickly. Although homogenous mixing is required for the mobile mass balance method, extreme vertical mixing can also result in very small enhancement values of

several tens of ppb which can be difficult to identify and is more susceptible to noise and interference from local sources. The correlation between methane and carbon dioxide was shown to be following the expected 1:1 ratio with measured correlation slope of 0.99 ± 0.04 mole mole $^{-1}$ for a landfill source. The estimated CO_2 emission rate from the landfill was 7600 ± 1700 kg h^{-1}. The overall methane emissions estimate for Greenlane landfill was significantly higher than the inventory value of 240 kg h^{-1} based on the GHGRP. From the two different landfill studies performed, the landfill gas collection system is considered the major methane loss in landfills compared to 0 – 10% loss by oxidation when inventory values are calculated. Therefore, it can be suspected that the inventory may be estimating excessive methane loss by inaccurate gas collection efficiency of the system, or the gas collection system might have good efficiency as expected in the inventory evaluation but there can be fugitive methane leaks from collection pipes which agrees with a single sharp hotspot peak observed at the southern part of the Greenlane landfill.

The two-day field studies performed on July 21/22, 2022, also successfully demonstrated the use of the mobile based mass balance method to quantify the broad area emissions from the city of Sarnia including its industrial facilities and residential areas. The use of gaussian dispersion and HYSPLIT back trajectories provided means of identifying and attributing individual sources. Similar to landfill studies, other tracers from the source can also be employed in future studies to further confirm the location of the methane sources. In the case of city of Sarnia, SO_2 can be used as a tracer from refineries burning fossil fuels containing sulfur compounds as well as from chemical plants. The average emission rates estimated by mass balance for the city of Sarnia was 2450 ± 560 kg h^{-1}. Day 2 methane enhancements were much higher, 2810 ± 930 kg h^{-1} compared to day 1 estimate of 2090 ± 640 kg/h^{-1} due to the widespread methane plumes that were transported from the Michigan State, U.S. It is estimated that city of Sarnia emit 21.5 ± 4.9 kt CH_4 annually which account for ~45% of Ontario's oil and natural gas methane emissions from 2020 Inventory value. Out of estimated 2450 ± 560 kg h^{-1} CH_4, Imperial Oil, Suncor, and Shell refineries were identified to be the major methane sources in industrial complex in which estimated source rates based on the gaussian model were 672 ± 230 kg h^{-1}, 349 kg h^{-1}, and 198 kg h^{-1} respectively. Three different estimates obtained form the Imperial Oil at different times of the day imply the facility has a possible temporal fluctuation in emission rate. Compared to the GHGRP estimates, the estimated emissions for the listed facilities were 9-10 times greater than

the report showing that the top-down estimates made across the source consistently show higher emissions estimate than the GHGRP regardless of the source type (Waste management sector compared to oil and natural gas sector). Results from this study highlights that the natural gas power plants and crude oil refineries are significant contributors to annual CH_4 in Ontario with a lack of accurate emissions quantification in the Canadian Inventories.

Both chapter 3 and 4 demonstrated that the mobile mass balance technique is a cost effective and convenient alternative top-down technique, not limited to the source type or the area. Additional modelling studies and satellite monitoring can help to fully characterize the plume and locate sources more accurately. More rigorous local dispersion models can be used to predict plume paths while satellite imageries can help to identify long term temporal variation. This is especially useful for the oil and gas facilities where the specific facility operations can produce strong temporal variation in methane emissions. Moreover, the satellite monitoring can be employed to detect future potential methane leaks from pipelines and storage facilities. Although the mass balance technique was proved to be convenient and accessible, the method strongly depended on the meteorological parameters, especially on the determination of boundary layer height and wind conditions. The use of LIDAR or Sodar on site could have provided more accurate data for the local boundary layer height which would have reduced the major uncertainty in the emissions estimates.

As the mobile mass balance is relatively low-cost and requires much less time to perform measurements, ideally the result of this study could be employed to reconcile top-down measurements to the bottom-up inventory. This will help to provide more accurate picture of methane sources and sinks in Canada which will ultimately aid in building effective reduction strategies to meet the climate goals.

References

2017 ANNUAL PROGRESS REPORT GREEN LANE LANDFILL, March 2018, WSP

Aghdam, E. F.; Scheutz, C.; Kjeldsen, P. Impact of Meteorological Parameters on Extracted Landfill Gas Composition and Flow. Waste Management 2019, 87, 905–914.

Baray, S., K. L. Hayden, A. Sheapard, Z. Davis, K. Strawbridge, R. Staebler and R. McLaren, ColdSeason Methane Emissions in the Athabasca Oil Sands Region of Alberta Estimated Using Mobile Surface Measurements, draft 1, in prep for Atmospheric Chemistry and Physics, 2021

Baray, S.; Darlington, A.; Gordon, M.; Hayden, K. L.; Leithead, A.; Li, S.-M.; Liu, P. S.; Mittermeier, R. L.; Moussa, S. G.; O'Brien, J.; Staebler, R.; Wolde, M.; Worthy, D.; McLaren, R. Quantification of Methane Sources in the Athabasca Oil Sands Region of Alberta by Aircraft Mass Balance. Atmospheric Chemistry and Physics 2018, 18 (10), 7361–7378.

Basic Information about Landfill Gas. https://www.epa.gov/lmop/basic-information-about-landfill-gas#:~:text=Landfill%20gas%20(LFG)%20is%20a,of%20non%2Dmethane%20organic%20compounds. (accessed Jan 29, 2023).

Brandt, A. R.; Heath, G. A.; Kort, E. A.; O'Sullivan, F.; Petron, G.; Jordaan, S. M.; Tans, P.; Wilcox, J.; Gopstein, A. M.; Arent, D.; Wofsy, S.; Brown, N. J.; Bradley, R.; Stucky, G. D.; Eardley, D.; Harriss, R. Methane Leaks from North American Natural Gas Systems. Science 2014, 343 (6172), 733–735.

Bronstein, K., Coburn, J., and Schmeltz, R.: Understanding the Inventory of U.S. Greenhouse Gas Emissions and Sinks and the Greenhouse Gas Reporting Program for Landfills: Methodologies, Uncertainties, Improvements and Deferrals, n.d.

Burba, G.; Madsen, R.; Feese, K. Eddy Covariance Method for CO2 Emission Measurements in CCUS Applications: Principles, Instrumentation and Software. Energy Procedia 2013, 40, 329–336.

Carson, J. E.; Moses, H. The Validity of Several Plume Rise Formulas. Journal of the Air Pollution Control Association 1969, 19 (11), 862–866.

Cusworth, D. H.; Thorpe, A. K.; Ayasse, A. K.; Stepp, D.; Heckler, J.; Asner, G. P.; Miller, C. E.; Yadav, V.; Chapman, J. W.; Eastwood, M. L.; Green, R. O.; Hmiel, B.; Lyon, D. R.; Duren, R. M. Strong Methane Point Sources Contribute a Disproportionate Fraction of Total Emissions across Multiple Basins in the United States. Proceedings of the National Academy of Sciences 2022, 119 (38).

Davis, Z. Y.; Baray, S.; McLinden, C. A.; Khanbabakhani, A.; Fujs, W.; Csukat, C.; Debosz, J.; McLaren, R. Estimation of Nox and so2 Emissions from Sarnia, Ontario, Using a Mobile Max-DOAS (Multi-Axis Differential Optical Absorption Spectroscopy) and a Nox Analyzer. Atmospheric Chemistry and Physics 2019, 19 (22), 13871–13889.

Deardorff, J. W.; Willis, G. E. A Parameterization of Diffusion into the Mixed Layer. Journal of Applied Meteorology 1975, 14 (8), 1451–1458.

Delgado, M.; López, A.; Esteban, A. L.; Lobo, A. Some Findings on the Spatial and Temporal Distribution of Methane Emissions in Landfills. Journal of Cleaner Production 2022, 362, 1 Bronstein, K., Coburn, J., & Schmeltz, R. (2012). Understanding the EPA's inventory of U.S. greenhouse gas emissions and sinks and mandatory GHG reporting program for landfills: Methodologies, uncertainties, improvements, and deferrals. In 20th International Emission Inventory Conference: Emission

Inventories–Meeting the Challenges Posed by Emerging Global, National, and Regional and Local Air Quality Issues (pp. 1 - 14)32334.

Dlugokencky, E. J.; Masarie, K. A.; Tans, P. P.; Conway, T. J.; Xiong, X. Is the Amplitude of the Methane Seasonal Cycle Changing? Atmospheric Environment 1997, 31 (1), 21–26.

Environment Canada: Ottawa, 2020.

Gordon, M.; Li, S.-M.; Staebler, R.; Darlington, A.; Hayden, K.; O'Brien, J.; Wolde, M. Determining Air Pollutant Emission Rates Based on Mass Balance Using Airborne Measurement Data over the Alberta Oil Sands Operations. Atmospheric Measurement Techniques 2015, 8 (9), 3745–3765.

Government of Canada, C. E. R. Provincial and Territorial Energy Profiles – Ontario. https://www.cer-rec.gc.ca/en/data-analysis/energy-markets/provincial-territorial-energy-profiles/provincial-territorial-energy-profiles-ontario.html (accessed Jan 27, 2023).

Guerrero-Cruz, S.; Vaksmaa, A.; Horn, M. A.; Niemann, H.; Pijuan, M.; Ho, A. Methanotrophs: Discoveries, Environmental Relevance, and a Perspective on Current and Future Applications. Frontiers in Microbiology 2021, 12.

Health Effects of Ozone Pollution. https://www.epa.gov/ground-level-ozone-pollution/health-effects-ozone-pollution (accessed Jan 20, 2023).

Jacob, D. J.; Turner, A. J.; Maasakkers, J. D.; Sheng, J.; Sun, K.; Liu, X.; Chance, K.; Aben, I.; McKeever, J.; Frankenberg, C. Satellite Observations of Atmospheric Methane and Their Value for Quantifying Methane Emissions. Atmospheric Chemistry and Physics 2016, 16 (22), 14371–14396.

Jacob, D. J.; Varon, D. J.; Cusworth, D. H.; Dennison, P. E.; Frankenberg, C.; Gautam, R.; Guanter, L.; Kelley, J.; McKeever, J.; Ott, L. E.; Poulter, B.; Qu, Z.; Thorpe, A. K.; Worden, J. R.; Duren, R. M. Quantifying Methane Emissions from the Global Scale down to Point Sources Using Satellite Observations of Atmospheric Methane. Atmospheric Chemistry and Physics 2022, 22 (14), 9617–9646.

Jardine, C. N.; Boardman, B.; Osman, A.; Vowles, J.; Palmer, J. Methane UK; Environmental Change Institute, University of Oxford: Oxford, 2004.

Johnson, M. R.; Tyner, D. R.; Conley, S.; Schwietzke, S.; Zavala-Araiza, D. Comparisons of Airborne Measurements and Inventory Estimates of Methane Emissions in the Alberta Upstream Oil and Gas Sector. Environmental Science & Technology 2017, 51 (21), 13008–13017.

Karion, A.; Sweeney, C.; Pétron, G.; Frost, G.; Michael Hardesty, R.; Kofler, J.; Miller, B. R.; Newberger, T.; Wolter, S.; Banta, R.; Brewer, A.; Dlugokencky, E.; Lang, P.; Montzka, S. A.; Schnell, R.; Tans, P.; Trainer, M.; Zamora, R.; Conley, S. Methane Emissions Estimate from Airborne Measurements over a Western United States Natural Gas Field. Geophysical Research Letters 2013, 40 (16), 4393–4397.

Khair, Z. M.; Joly, L.; Cousin, J.; Decarpenterie, T.; Dumelié, N.; Maamary, R.; Chauvin, N.; Durry, G. In Situ Measurements of Methane in the Troposphere and the Stratosphere by the Ultra Light Spectrometer Amulse. Applied Physics B 2017, 123 (12).

Kirschke, S.; Bousquet, P.; Ciais, P.; Saunois, M.; Canadell, J. G.; Dlugokencky, E. J.; Bergamaschi, P.; Bergmann, D.; Blake, D. R.; Bruhwiler, L.; Cameron-Smith, P.; Castaldi, S.; Chevallier, F.; Feng, L.; Fraser, A.; Heimann, M.; Hodson, E. L.; Houweling, S.; Josse, B.; Fraser, P. J.; Krummel, P. B.;

Lamarque, J.-F.; Langenfelds, R. L.; Le Quéré, C.; Naik, V.; O'Doherty, S.; Palmer, P. I.; Pison, I.; Plummer, D.; Poulter, B.; Prinn, R. G.; Rigby, M.; Ringeval, B.; Santini, M.; Schmidt, M.; Shindell, D. T.; Simpson, I. J.; Spahni, R.; Steele, L. P.; Strode, S. A.; Sudo, K.; Szopa, S.; van der Werf, G. R.; Voulgarakis, A.; van Weele, M.; Weiss, R. F.; Williams, J. E.; Zeng, G. Three Decades of Global Methane Sources and Sinks. Nature Geoscience 2013, 6 (10), 813–823.

Landfill Gas Primer: An Overview for Environmental Health Professionals; The Agency for Toxic Substances and Disease Registry (ATSDR): Atlanta, GA, 2001.

Lavoie, T. N.; Shepson, P. B.; Gore, C. A.; Stirm, B. H.; Kaeser, R.; Wulle, B.; Lyon, D.; Rudek, J. Assessing the Methane Emissions from Natural Gas-Fired Power Plants and Oil Refineries. Environmental Science & Technology 2017, 51 (6), 3373–3381.

Manisalidis, I.; Stavropoulou, E.; Stavropoulos, A.; Bezirtzoglou, E. Environmental and Health Impacts of Air Pollution: A Review. Frontiers in Public Health 2020, 8.

Martin, D. O. Comment on"the Change of Concentration Standard Deviations with Distance". Journal of the Air Pollution Control Association 1976, 26 (2), 145–147.

Meyer-Dombard, D. A. R.; Bogner, J. E.; Malas, J. A Review of Landfill Microbiology and Ecology: A Call for Modernization with ‘next Generation’ Technology. Frontiers in Microbiology 2020, 11.

Michigan Natural Gas Active Storage Field Summary. https://www.michigan.gov/mpsc/regulatory/natural-gas/transportation-storage/michigan-natural-gas-active-storage-field-summary#Reference (accessed Feb 1, 2023).

Miller, S. M.; Wofsy, S. C.; Michalak, A. M.; Kort, E. A.; Andrews, A. E.; Biraud, S. C.; Dlugokencky, E. J.; Eluszkiewicz, J.; Fischer, M. L.; Janssens-Maenhout, G.; Miller, B. R.; Miller, J. B.; Montzka, S. A.; Nehrkorn, T.; Sweeney, C. Anthropogenic Emissions of Methane in the United States. Proceedings of the National Academy of Sciences 2013, 110 (50), 20018–20022.

Myhre, G., D. Shindell, F.-M. Bréon, W. Collins, J. Fuglestvedt, J. Huang, D. Koch, J.-F. Lamarque, D. Lee, B. Mendoza, T. Nakajima, A. Robock, G. Stephens, T. Takemura and H. Zhang, 2013: Anthropogenic and Natural Radiative Forcing. In: Climate Change 2013: The Physical Science Basis. Contribution of Working Group I to the Fifth Assessment Report of the Intergovernmental Panel on Climate Change [Stocker, T.F., D. Qin, G.-K. Plattner, M. Tignor, S.K. Allen, J. Boschung, A. Nauels, Y. Xia, V. Bex and P.M. Midgley (eds.)]. Cambridge University Press, Cambridge, United Kingdom and New York, NY, USA.

National Pipeline Mapping system Public Map Viewer. https://www.npms.phmsa.dot.gov/ (accessed Jan 19, 2023).

Nam, E. K.; Jensen, T. E.; Wallington, T. J. Methane Emissions from Vehicles. Environmental Science & Technology 2004, 38 (7), 2005–2010.

Olaguer, E. P. The Potential Ozone Impacts of Landfills. Atmosphere 2021, 12 (7), 877.

Paige, M. E.; Silver, J. A.; Petroski, D.; Bomse, D. S. Portable Natural Gas Leak Detector for Survey Inspections. SPIE Proceedings 2006.

Pasquill Stability Classes. https://www.ready.noaa.gov/READYpgclass.php#:~:text=Strong%20insolation%20corresponds%20to%20sunny,to%20similar%20conditions%20in%20midwinter. (accessed May 12, 2022).

Peña Alfredo. Sensing the wind profile. dissertation, Department of Geography and Geology, Faculty of Science, University of Copenhagen: Cph., 2009.

Pihlatie, M. K.; Christiansen, J. R.; Aaltonen, H.; Korhonen, J. F. J.; Nordbo, A.; Rasilo, T.; Benanti, G.; Giebels, M.; Helmy, M.; Sheehy, J.; Jones, S.; Juszczak, R.; Klefoth, R.; Lobo-do-Vale, R.; Rosa, A. P.; Schreiber, P.; Serça, D.; Vicca, S.; Wolf, B.; Pumpanen, J. Comparison of Static Chambers to Measure CH4 Emissions from Soils. Agricultural and Forest Meteorology 2013, 171-172, 124–136.

Ramaswamy V., Boucher O., Haigh J., Hauglustaine D., Haywood J., Myhre G., Nakajima T., Shi G. Y., Solomon S., Radiative Forcing of Climate Change. In Climate change 2001 the scientific basis; Cambridge Univ. Pr: Cambridge, 2001.

Riddick, S. N.; Hancock, B. R.; Robinson, A. D.; Connors, S.; Davies, S.; Allen, G.; Pitt, J.; Harris, N. R. P. Development of a Low-Maintenance Measurement Approach to Continuously Estimate Methane Emissions: A Case Study. Waste Management 2018, 73, 210–219.

Röwer, I. U.; Geck, C.; Gebert, J.; Pfeiffer, E.-M. Spatial Variability of Soil Gas Concentration and Methane Oxidation Capacity in Landfill Covers. Waste Management 2011, 31 (5), 926–934.

Saunois, M.; Bousquet, P.; Poulter, B.; Peregon, A.; Ciais, P.; Canadell, J.G.; Dlugokencky, E.J.; Etiope, G.; Bastviken, D.; Houweling, S.; et al. The global methane budget 2000–2012. Earth Syst. Sci. Data 2016, 8, 697–751.

Scheutz, C.; Kjeldsen, P. Environmental Factors Influencing Attenuation of Methane and Hydrochlorofluorocarbons in Landfill Cover Soils. Journal of Environmental Quality 2004, 33 (1), 72–79.

Simon, A. L.: CHAPTER 6 - Natural Gas, In Energy Resources; Pergamon Press Ltd., Oxford, United Kingdom, 67-73, https://doi.org/10.1016/B978-0-08-018750-1.50011-6., 1975.

Spokas, K.; Bogner, J.; Corcoran, M.; Walker, S. From California Dreaming to California Data: Challenging Historic Models for Landfill CH4 Emissions. Elementa: Science of the Anthropocene 2015, 3.

State of Waste in Ontario: Landfill Report, January 2021, Ontario Waste Management Association

Stolper, D.A., Martini, A.M., Clog, M., Douglas, P.M., Shusta, S.S., Valentine, D.L., Sessions, A.L., Eiler, J.M., Distinguishing and understanding thermogenic and biogenic sources of methane using multiply substituted isotopologues, Geochimica et Cosmochimica Acta (2015), doi: http://dx.doi.org/10.1016/j.gca. 2015.

Stull, R. B. Practical meteorology: An algebra-based survey of Atmospheric Science; Dept. of Earth, Ocean & Atmospheric Sciences, University of British Columbia: Vancouver (BC, Canada), 2017.

Su, Y.; Zhang, X.; Xia, F.-F.; Zhang, Q.-Q.; Kong, J.-Y.; Wang, J.; He, R. Diversity and Activity of Methanotrophs in Landfill Cover Soils with and without Landfill Gas Recovery Systems. Systematic and Applied Microbiology 2014, 37 (3), 200–207.

Vaughn, T. L.; Bell, C. S.; Pickering, C. K.; Schwietzke, S.; Heath, G. A.; Pétron, G.; Zimmerle, D. J.; Schnell, R. C.; Nummedal, D. Temporal Variability Largely Explains Top-down/Bottom-up Difference in

Methane Emission Estimates from a Natural Gas Production Region. Proceedings of the National Academy of Sciences 2018, 115 (46), 11712–11717.

Weiner, R. F.; Matthews, R. A.; Vesilind, P. A. In Environmental engineering; Butterworth-Heinemann: Amsterdam, 2003; pp 351–374.

West, J. J.; Fiore, A. M. Management of Tropospheric Ozone by Reducing Methane Emissions. Environmental Science & Technology 2005, 39 (13), 4685–4691.

Xu, L.; Lin, X.; Amen, J.; Welding, K.; McDermitt, D. Impact of Changes in Barometric Pressure on Landfill Methane Emission. Global Biogeochemical Cycles 2014, 28 (7), 679–695.

Zaman, M.; Heng, L. K.; Müller Christoph. Measuring emission of agricultural greenhouse gases and developing mitigation options using nuclear and related techniques: Applications of nuclear techniques for ghgs; Springer: Applications of nuclear techniques for GHGs, 2021.

Zavala-Araiza, D.; Alvarez, R. A.; Lyon, D. R.; Allen, D. T.; Marchese, A. J.; Zimmerle, D. J.; Hamburg, S. P. Super-Emitters in Natural Gas Infrastructure Are Caused by Abnormal Process Conditions. Nature Communications 2017, 8 (1).

Zavala-Araiza, D.; Lyon, D. R.; Alvarez, R. A.; Davis, K. J.; Harriss, R.; Herndon, S. C.; Karion, A.; Kort, E. A.; Lamb, B. K.; Lan, X.; Marchese, A. J.; Pacala, S. W.; Robinson, A. L.; Shepson, P. B.; Sweeney, C.; Talbot, R.; Townsend-Small, A.; Yacovitch, T. I.; Zimmerle, D. J.; Hamburg, S. P. Reconciling Divergent Estimates of Oil and Gas Methane Emissions. Proceedings of the National Academy of Sciences 2015, 112 (51), 15597–15602.

Zavala-Araiza, D.; Lyon, D.; Alvarez, R. A.; Palacios, V.; Harriss, R.; Lan, X.; Talbot, R.; Hamburg, S. P. Toward a Functional Definition of Methane Super-Emitters: Application to Natural Gas Production Sites. Environmental Science & Technology 2015, 49 (13), 8167–8174.

Zhang, Y.; Gautam, R.; Pandey, S.; Omara, M.; Maasakkers, J. D.; Sadavarte, P.; Lyon, D.; Nesser, H.; Sulprizio, M. P.; Varon, D. J.; Zhang, R.; Houweling, S.; Zavala-Araiza, D.; Alvarez, R. A.; Lorente, A.; Hamburg, S. P.; Aben, I.; Jacob, D. J. Quantifying Methane Emissions from the Largest Oil-Producing Basin in the United States from Space. Science Advances 2020, 6 (17).

Zhao, J.; Zhang, M.; Xiao, W.; Wang, W.; Zhang, Z.; Yu, Z.; Xiao, Q.; Cao, Z.; Xu, J.; Zhang, X.; Liu, S.; Lee, X. An Evaluation of the Flux-Gradient and the Eddy Covariance Method to Measure CH4, CO2, and H2O Fluxes from Small Ponds. Agricultural and Forest Meteorology 2019, 275, 255–264.

Appendices

Appendix A: Supplemental for Chapter 1

Table A.1: Wind profile exponents for different atmospheric stability classes, from U.S. Environmental Protection Agency, 1995

Stability Class	**Exponent, α**	
	Urban Region (Rough Surface)	Rural Region (Smooth Surface)
A	0.15	0.07
B	0.15	0.07
C	0.20	0.07
D	0.25	0.10
E	0.30	0.35
F	0.30	0.35

Table A.2: Meteorological conditions to define Pasquill stability classes.

	Daytime Solar Radiation		
Surface wind speed (m/s)	**Strong**	**Moderate**	**Slight**
< 2	A	A – B	B
2 – 3	A – B	B	C
3 – 5	B	B – C	C
5 – 6	C	C – D	D
> 6	C	D	D

Table A.3: Martin Scheme for σ_y variables (a, and b) for downwind distance, x.

Pasquill Stability Class	$\boldsymbol{\sigma_y}$ ***lateral dispersion for downwind distance, x km***	
	a	*b*
A	213	0.894
B	156	
C	104	
D	68	
E	50.5	
F	34	

Table A.4: Martin Scheme for σ_z variables (c, d, and f) for downwind distance, x.

Pasquill Stability Class	$\boldsymbol{\sigma_z}$ ***vertical dispersion for downwind distance, x km***					
	x < 1.0 km			*x* ≥ 1.0 km		
	c	*d*	*f*	*c*	*d*	*f*
A	440.8	1.041	9.27	459.7	2.094	-9.6
B	106.6	1.149	3.3	108.2	1.098	2
C	61	0.911	0	61	0.911	0
D	33.2	0.725	-1.7	44.5	0.516	-13
E	22.8	0.675	-1.3	55.4	0.305	-34
F	14.35	0.74	-0.35	62.6	0.18	-48.6

Appendix B: Supplemental for Chapter 3

B.1: Calculation of Deardorff velocity and mixing distance for Study B

Deardorff velocity is calculated by:

$$w^* = \left[\frac{g}{T} Z_i F\right]^{\frac{1}{3}} = \left[\frac{\left(9.81 \frac{m}{s}\right)}{278.62\ K} (420m) \left(0.360 \frac{Km}{s}\right)\right]^{\frac{1}{3}} = 1.746 \frac{m}{s}$$

Calculation of well mixing time and distance:

$$t_m = \frac{Z_i}{w^*} = \frac{420\ m}{1.746 \frac{m}{s}} = \ 241\ s\ , 3t_m\ =\ 723\ \text{s}$$

Well mixing distance = $3t_m v = \ 723s\frac{4.8m}{s} = 3470m \ \approx 3.5\ km$

Propagation of uncertainty on the mixing distance:

1. Uncertainty on the Deardorff velocity: assuming the only uncertainty exists on the boundary layer height and that the uncertainty on F, and T are relatively small,

$$\frac{\delta w^*}{w^*} = \frac{1}{3}\left(\frac{\delta Z_i}{Z_i}\right) = \frac{1}{3}\left(\frac{100m}{420m}\right) = 0.07936$$

2. Overall uncertainty on the mixing distance, d_{mixed}:

$$\frac{\delta d_{mixed}}{d_{mixed}} = \left[\left(\frac{\delta w^*}{w^*}\right)^2 + \left(\frac{\delta Z_i}{Z_i}\right)^2 + \left(\frac{\delta v}{v}\right)^2\right]^{\frac{1}{2}}$$

$$= [(0.07936)^2 + (0.23810)^2 + (0.08333)^2]^{\frac{1}{2}} = 0.26445 \approx 26\%$$

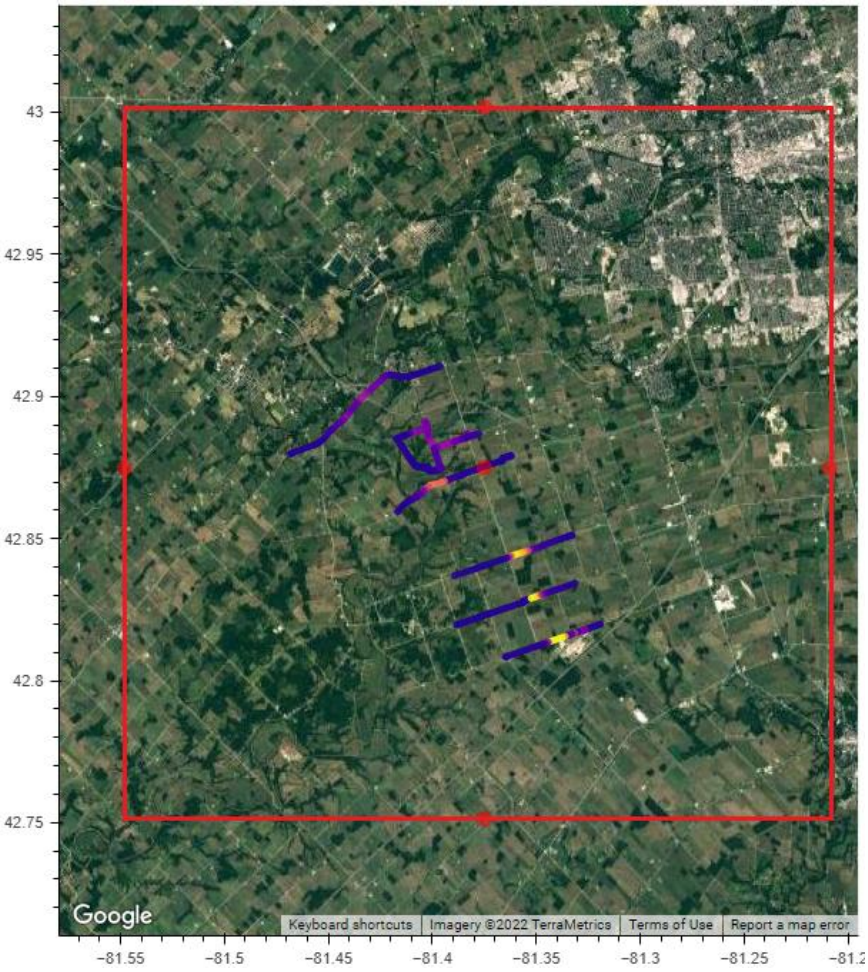

Figure B.1: GOES 16 DSR cell with the resolution of 27 km enclosing transects and the landfill.

Table B.1: Table of PBL height data and the kinematics parameters for Study D

Estimated Planetary Boundary Layer (PBL) Height	
PBL Height (Ceilometer) (m)	870 ± 150
PBL Height (NCEP) (m)	1200 ± 500
PBL Height (Aircraft Flights) (m)	950 ± 150
Average PBL Height (m)	1006 ± 180
Kinematics Parameters	
Average Downwelling Shortwave Radiation (Surface) (W/m^2)	433 ± 13
Surface Kinematic Heat Flux (Km/s)	0.352
Deardorff Velocity (m/s)	2.28
Convective Mixing Time (s)	438

Table B.2: Maximum values observed for study B and D at each transect.

Study B	Distance from the landfill (m)	Max CH4 (ppm)
T0	770	23.38
T1	2700	5.06
T2	4500	4.14
T3	8600	3.20
T5	13000	2.58
Study D	Distance from the landfill (m)	Max CH4 (ppm)
T1	2200	3.31
T2	7500	2.21
T3	9600	2.19
T4	11600	2.14

Table B.3: Summary of the meteorological parameters from 4 different studies for comparison

	Study A (Oct 15)	**Study B (Feb 21)**	**Study C (July 7)**	**Study D (Oct 1)**
Wind Velocity (m/s)	1.5 ± 0.7	4.8 ± 0.4	1.2 ± 0.5	4.8 ± 0.6
Temperature (K) [°C]	289.1 ± 0.6 [16 °C]	278.6 ± 0.1 [5 °]	296.5 ± 0.3 [23 °C]	291.1 ± 0.01 [18 °]
Pressure (kPa)	97.97 ± 0.06	98.58 ± 0.01	98.47 ± 0.02	98.75 ± 0.03
Solar Insolation (W/m^2)	266	443	693	433
Boundary Layer Height (m)	360	420 ± 100	1100	1000 ± 200
Surface Kinematic Heat Flux (Km/s)	0.216	0.360	0.563	0.352
Deardorff Velocity (m/s)	1.38	1.746	2.736	2.28
Convective Mixing Time (s)	261	241	402	438
Homogenous mixing Distance (m)	1200	3500	1500	6300

Appendix C: Supplemental for Chapter 4

C1. Calculation of kinematics parameter and mixing distance for July 21st measurement

Calculation of the kinematic heat flux:

$$F = \frac{870\ Wm^{-2}}{1231\left(\frac{Wm^{-2}}{Kms^{-1}}\right)} = 0.7067\ K\frac{m}{s},$$

Calculation of convective velocity scale:

$$w^* = \left[\frac{g}{T} Z_i F\right]^{\frac{1}{3}} = \left[\frac{\left(9.81 \frac{m}{s}\right)}{303.25\ K} (790m) \left(0.7067 \frac{Km}{s}\right)\right]^{\frac{1}{3}} = 2.624 \frac{m}{s}$$

Calculation of well mixing time and distance:

$$t_m = \frac{Z_i}{w^*} = \frac{790m}{2.624 \frac{m}{s}} = 301\ s\ , 3t_m = 903\ s$$

Well mixing distance = $3t_m v = 903s \frac{10.3m}{s} = 9303m \approx 9.3\ km$

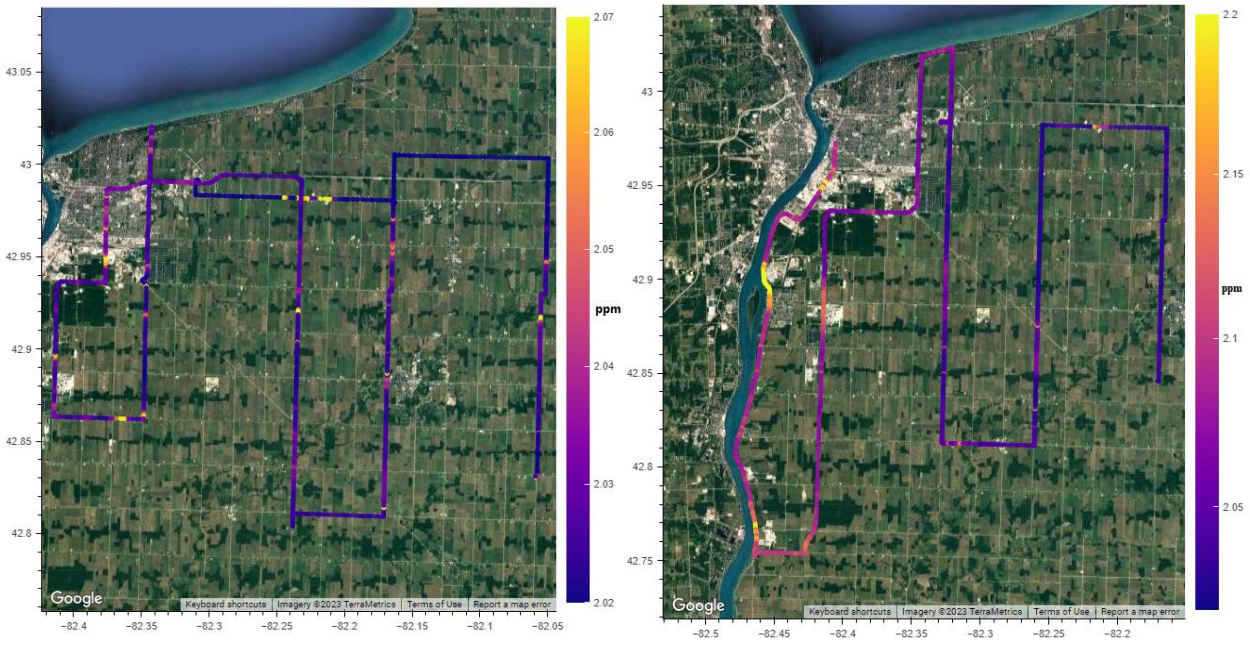

Figure C.1: Full survey maps of Sarnia at downwind locations on first day of study, July 21st (Left) and second day on July 22nd (Right)

Table C.1: Summary of kinematics parameters per transect for July 22nd .

Transect	*Kinematic Heat Flux (Km/s)*	*Convective Velocity Scale (m/s)*	*Mixing time (3 t_m) (s)*	*3 t_m mixing distance (m)*
0	0.4078	1.716	664	2300
1	0.4736	1.685	552	2600
2	0.5646	2.310	870	7000
3	0.5987	2.295	810	7500
4	0.5987	2.295	810	8800